

This book deals with the phenomena of magnetism exhibited by intermetallic compounds. We selected the rare earth based intermetallic compounds considering the interesting magnetic behavior of the 4f orbital. A variety of interesting properties are exhibited in these compounds simply by changing the rare earth element. The interesting behavior includes: Pauli-paramagnetism, heavy fermion behavior, crystal field effects, hard and soft ferromagnets, various anisotropic effects, etc. Apart from this, exploring the 4f orbital has become a trend for the fundamental studies as well as practical applications. The presence of a 3d orbital also motivates the interest because of the interplay between them. We present our studies on 4f orbital, 3d orbital and their interplay in this book.

Magnetic Behaviour in Rare Earth



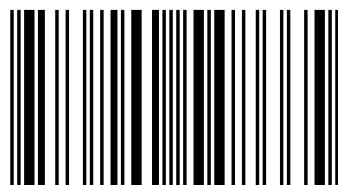
Devang Joshi

Magnetic Behaviour in Rare Earth Intermetallic Indides and Gallides

Magnetic Properties of Some of the Rare Earth Intermetallic Indides and Gallides



Dr. Devang Joshi has completed his masters from Gujarat University, followed by a PhD from IIT Bombay. His post PhD research experience is from four different institutes spanning up to eight years; TIFR, Mumbai, KIT, Germany, IPR Gandhinagar and TU Wien. Currently the author is working as an Assistant Professor at IITE Gandhinagar.



978-620-0-54866-5

Joshi

LAP LAMBERT
Academic Publishing

Devang Joshi

Magnetic Behaviour in Rare Earth Intermetallic Indides and Gallides

FOR AUTHOR USE ONLY

FOR AUTHOR USE ONLY

Devang Joshi

Magnetic Behaviour in Rare Earth Intermetallic Indides and Gallides

**Magnetic Properties of Some of the Rare Earth
Intermetallic Indides and Gallides**

FOR AUTHOR USE ONLY

LAP LAMBERT Academic Publishing

Imprint

Any brand names and product names mentioned in this book are subject to trademark, brand or patent protection and are trademarks or registered trademarks of their respective holders. The use of brand names, product names, common names, trade names, product descriptions etc. even without a particular marking in this work is in no way to be construed to mean that such names may be regarded as unrestricted in respect of trademark and brand protection legislation and could thus be used by anyone.

Cover image: www.ingimage.com

Publisher:

LAP LAMBERT Academic Publishing

is a trademark of

International Book Market Service Ltd., member of OmniScriptum Publishing Group

17 Meldrum Street, Beau Bassin 71504, Mauritius

Printed at: see last page

ISBN: 978-620-0-54866-5

Copyright © Devang Joshi

Copyright © 2020 International Book Market Service Ltd., member of OmniScriptum Publishing Group

FOR AUTHOR USE ONLY

Dedicated

to

My Parents

Arvind P. Joshi & Madhu A. Joshi

Abstract

This book deals with the phenomena of magnetism exhibited by intermetallic compounds. We selected the rare earth based intermetallic compounds considering the interesting magnetic behavior of the 4f orbital. A variety of interesting properties are exhibited in these compounds simply by changing the rare earth element. The interesting behavior includes: Pauli-paramagnetism, heavy fermion behavior, crystal field effects, hard and soft ferromagnets, various anisotropic effects, etc. Apart from this, exploring the 4f orbital has become a trend for the fundamental studies as well as practical applications. The presence of a 3d orbital also motivates the interest because of the interplay between them. We present our studies on 4f orbital, 3d orbital and their interplay in this book.

Here we describe a detailed study on some of the rare earth indides and gallides. It involves the study on a series of ternary indides R_2CoIn_8 (R = rare earths and Y) and substitutional studies on RNi_5 compounds namely: RNi_4Ga , RNi_3FeGa and RNi_3MnGa . Magnetism in these series of compounds is studied using their magnetic, specific heat and transport characteristic.

The book begins with chapter 1, intended to introduce the readers about the theoretical and experimental aspects of rare earth magnetism. The topics are selected on the basis of which the results of the subsequent chapters are explained. The second chapter covers the details of various experimental techniques used for preparing and characterizing the rare earth intermetallic alloys.

The subsequent chapters (Ch. 3, Ch. 4 and Ch. 5) describe the results and discussion on the original work done on the series of intermetallic compounds discussed above. Finally we conclude our discussion by the Conclusion chapter discussing the important results of our study with a future direction on the unexplored part of our studies.

All the investigated samples in this book were made by standard arc melting procedure followed by the annealing required for the respective samples.

Chapter 3

In this chapter we have investigated the magnetic, thermal and transport properties of the R_2CoIn_8 series of compounds. R_2CoIn_8 compounds form with $R = Ce, Pr, Nd, Sm, Gd, Tb, Dy, Ho$ and Y in Ho_2CoGa_8 type tetragonal structure with a space group $P4/mmm$. The lattice parameters are such that the lattice ratio $c/a \sim 3$. Rare earth and Cobalt atoms occupy crystallo-

graphic sites $2g$ and $1a$, respectively with occupancy 2 and 1. Indium atoms occupy sites $2e$, $2h$ and $4i$ with occupancy 2, 2 and 4, respectively.

The nonmagnetic Y compound (Y_2CoIn_8) shows a Pauli-paramagnetic behavior. The heat capacity and resistivity also show a behavior expected for a nonmagnetic compound. These results confirm the nonmagnetic behavior of the compound and hence the Co atoms can be considered to be nonmagnetic in this series of compounds. Ce_2CoIn_8 is a heavy fermion ($\gamma = 480$ mJ/mole-K) superconductor ($T_c = 0.4$ K). The resistivity behavior of the compound reflects a dominant Kondo behavior at high temperatures (above ≈ 40 K) and a non Fermi liquid behavior at low temperatures (down to 2 K). The magnetization results are in agreement with the Kondo behavior. Pr_2CoIn_8 does not show any magnetic ordering down to 2 K, but shows a dominating crystal field effect at low temperatures. The crystal field fit to the inverse susceptibility shows a nonmagnetic doublet ground state, which occurs rarely.

Compounds with the rest of the magnetic rare earths ($R = Sm, Gd, Tb, Dy$ and Ho) order antiferromagnetically at low temperatures. All the compounds except Gd_2CoIn_8 show metamagnetic transitions at 2 K. Dy_2CoIn_8 and Ho_2CoIn_8 at 2 K show a field induced ferromagnetic transition at 83 kOe and 55 kOe, respectively. Dy_2CoIn_8 undergoes a spin reorientation at 5 K below its transition temperature. Magnetization results of Sm_2CoIn_8 and Tb_2CoIn_8 show an effect of a ferromagnetic component below the ordering temperature. The behavior is attributed to the incomplete cancellation of antiferromagnetically ordered spins. In case of Sm_2CoIn_8 , the magnetic isotherm at 2 K shows that the compound remains in the field induced metamagnetic state even if the field is reduced to zero. This behavior is attributed to the highly anisotropic behavior of the Sm^{3+} ions. Magnetization measurements on Tb_2CoIn_8 show the possibility of a complex magnetic structure with dominating antiferromagnetic interactions. The heat capacity and resistivity measurements also support the result. The compound also shows an unexpectedly high magnetoresistance at 2 K ($\approx 2500\%$). Magnetization results of Gd_2CoIn_8 show strong antiferromagnetic interactions between the Gd moments.

Chapter 4

This chapter describes the magnetic and thermal properties of RNi_4Ga series of compounds. The series forms as a substitutional variant of the well known RNi_5 series of compounds. Compounds form in the $CaCu_5$ type hexagonal structure with a space group $P6/mmm$. Within a unit

cell, the rare earth atoms occupy crystallographic $1a$ site with occupancy 1, Ni atoms occupy $2c$ and $3g$ sites, both with occupancy 2. However, when Ga is substituted for Ni, it occupies only the $3g$ site. The result is attributed to the larger metallic radius of Ga atom (1.41 Å) compared to Ni (1.24 Å). The unit cell volume shows a lanthanide contraction behavior except CeNi₄Ga, because of its mixed valent behavior. The unit cell volume increases compared to that of the parent compound due to the larger size of Ga compared to Ni.

The nonmagnetic La and Lu compounds show a Pauli-paramagnetic behavior similar to that of their parent compounds. This shows a nonmagnetic behavior of Ni in this series of compounds. CeNi₄Ga and PrNi₄Ga show a paramagnetic behavior down to 2 K.

Compounds with rest of the rare earths order ferromagnetically at low temperatures (below 20 K). The transition temperature decreases compared to that of the parent compound. The reason can be attributed to the decrease in the absolute value of the conduction electron polarization responsible for the RKKY interaction. The transition temperature of SmNi₄Ga and TbNi₄Ga deviates appreciably from that expected from the de-Gennes scaling and the possible reason is attributed to the crystal field effects.

All the compounds show anisotropic magnetic behavior except GdNi₄Ga. At 2 K, GdNi₄Ga gives a saturation magnetization value more than the theoretically expected value. The extra contribution is attributed to the polarization of the conduction electrons and a possible filling up of the $3d$ band. GdNi₄Ga shows the possibility of helical magnetic structure in the ordered state at low fields (below 100e).

The coercive field obtained for all the compounds was negligible except for SmNi₄Ga ($H_c = 40$ kOe) and TbNi₄Ga ($H_c = 2$ kOe), due to their high anisotropy. High coercivity in SmNi₄Ga is attributed to the presence of narrow domain walls. A rough estimate of the thickness of the domain walls calculated from the temperature dependence of H_c comes out to be 8 Å.

Chapter 5

The nonmagnetic behavior of Ni in RNi₄Ga series of compounds motivated us to see the effect on other magnetic $3d$ elements within the lattice. We selected Mn and Fe for the present study. In this chapter we will be discussing the effect of Fe and Mn substitution at the Ni site in RNi₄Ga, forming RNi₃MnGa and RNi₃FeGa. Our discussion will be mainly focused on the magnetization behavior of these compounds.

RNi_3MnGa and RNi_3FeGa form in the $CaCu_5$ type hexagonal structure with a space group $P6/mmm$, maintaining the structure of the parent compound. Both Fe and Mn have equal preference to the $2c$ and $3g$ sites. This may be due to the comparable size of Ni (1.24 Å), Fe (1.26 Å) and Mn (1.28 Å). The unit cell volume has increased compared to that of the parent compounds. The unit cell volume of Mn compounds is larger than that of the Fe compounds. The reason may be due to the larger size of Mn compared to Fe. In both the series of compounds the unit cell volume follows the lanthanide contraction except for Ce compounds. This implies that Ce retains its mixed behavior in these compounds also.

Y and La compounds in both the series (with Fe and Mn) show magnetic ordering at low temperatures (below 40 K). This shows that both Mn and Fe retain the magnetic behavior in the compound (assuming Ni is nonmagnetic). Y compounds in both the series show spin glass behavior at low temperatures. La compounds show an anisotropic ferromagnetic behavior at low temperatures.

$CeNi_3FeGa$ shows an onset of ferromagnetic type magnetic ordering at 15 K, whereas $CeNi_3MnGa$ orders ferromagnetically at 23 K. Compounds of Fe and Mn with rest of the rare earths show a ferromagnetic ordering at very high temperatures (between 50 to 250 K) compared to their parent compounds RNi_4Ga . The ferromagnetic ordering temperature increases due to the ordering of the substituted ions at high temperature in the compound.

$GdNi_3FeGa$ and $GdNi_3MnGa$ show anisotropic behavior in contrast to the isotropic behavior exhibited by $GdNi_4Ga$. The anisotropy is induced by the substituted Fe and Mn ions. $SmNi_3FeGa$ shows a highly anisotropic behavior with a large ferromagnetic ordering temperature of 240 K (maximum of all the investigated compounds). The coercivity obtained at 15 K is 40 kOe. The Sm compound could not be formed in single phase with Mn. $NdNi_3FeGa$, $NdNi_3MnGa$, $PrNi_3MnGa$ and $ErNi_3FeGa$ shows step like metamagnetic transitions at 2 K. $ErNi_3FeGa$ shows spin compensating ferrimagnetic behavior with negative magnetization (~ 160 K) below its ordering temperature (190 K) at low fields (below 600 Oe). The reason is attributed to the higher anisotropic energy at the Er site which holds the Er moment against the field, in addition to the ferrimagnetic ordering of Er and Fe moments.

Contents

| | |
|---|-----------|
| 1. Introduction | 1 |
| 1.1 Paramagnetism | |
| 1.1.1 Spin Paramagnetism | 1 |
| 1.1.2 Van-Vleck Paramagnetism | 4 |
| 1.1.3 Pauli Paramagnetism | 5 |
| 1.2 Magnetic Ordering | |
| 1.6.1 Indirect Exchange (RKKY) | 6 |
| 1.6.2 Direct Exchange | 9 |
| 1.3 Transport Property | 9 |
| 1.4 Kondo Effect (Single ion and Kondo Lattice) | 12 |
| 1.5 Thermal Property (Heat Capacity) | 14 |
| 1.6 Crystal Electric Field Effects | 18 |
| 1.6.1 Effect on Magnetization | 20 |
| 1.6.2 Effect on Heat Capacity | 20 |
| 1.6.3 Effect on Resistivity | 21 |
| 1.7 Spin Glass Behavior | 22 |
| 1.8 References | 24 |
| 2. Experimental Methods | 26 |
| 2.1 Sample Preparation | 26 |
| 2.2 Phase Detection | 26 |
| 2.3 Resistivity Measurements | 28 |
| 2.4 Magnetization Measurements | 29 |
| 2.4.1 VSM (Vibrating Sample Magnetometer) | 29 |
| 2.4.2 Squid (Superconducting Quantum Interference Device) | 31 |
| 2.4.3 AC Susceptibility Measurement | 33 |
| 2.5 Heat Capacity | 34 |
| 2.6 References | 35 |
| 3. Magnetic Properties of Ternary Indides $R_2\text{CoIn}_8$ (R = rare earths & Y) | 36 |
| 3.1 Introduction | 36 |

| | | |
|---------|--|------------|
| 3.2 | Sample Preparation and Crystal Structure | 38 |
| 3.3 | Results and Discussions | 43 |
| 3.3.1 | $R_2\text{CoIn}_8$ ($R = \text{Y, Ce, Pr}$) | |
| 3.3.2.1 | Magnetization Measurements | 43 |
| 3.3.2.2 | Resistivity Measurements | 49 |
| 3.3.2.3 | Heat Capacity Measurements | 54 |
| 3.3.2 | $R_2\text{CoIn}_8$ ($R = \text{Sm, Gd, Tb, Dy and Ho}$) | 58 |
| 3.3.2.1 | Gd_2CoIn_8 | 59 |
| 3.3.2.2 | Dy_2CoIn_8 | 62 |
| 3.3.2.3 | Ho_2CoIn_8 | 68 |
| 3.3.2.4 | Sm_2CoIn_8 | 72 |
| 3.3.2.5 | Tb_2CoIn_8 | 77 |
| 3.4 | Summary | 80 |
| 3.5 | References | 81 |
| 4. | Magnetic Properties of Ternary Gallides $R\text{Ni}_4\text{Ga}$ ($R = \text{rare earths}$) | 83 |
| 4.1 | Introduction | 83 |
| 4.2 | Sample Preparation and Crystal Structure | 84 |
| 4.3 | Results and Discussion | 87 |
| 4.3.1 | Primary Discussion | |
| 4.3.1.1 | Magnetization Measurements | 87 |
| 4.3.1.2 | Heat Capacity Measurements | 99 |
| 4.3.2 | Detailed Discussion for GdNi_4Ga and LaNi_4Ga | 101 |
| 4.3.3 | Detailed Discussion for SmNi_4Ga and TbNi_4Ga | 107 |
| 4.4 | Summary | 114 |
| 4.5 | References | 114 |
| 5 | Magnetic Properties of $R\text{Ni}_3\text{TGa}$ ($R = \text{rare earths, } T = \text{Fe and Mn}$) compounds | 117 |
| 5.1 | Introduction | 117 |
| 5.2 | Sample Preparation and Crystal Structure | 117 |
| 5.3 | Results and Discussions | |
| 5.3.1 | $R\text{Ni}_3\text{FeGa}$ and $R\text{Ni}_3\text{MnGa}$ ($R = \text{Nonmagnetic rare earths, La and Y}$) | 123 |
| 5.3.2 | $R\text{Ni}_3\text{FeGa}$ ($R = \text{Ce, Pr, Nd, Sm, Gd, Tb, Dy, Ho and Er}$) | 135 |

| | | |
|----------|---|------------|
| 5.3.3 | Spin Compensation Behavior of ErNi_3FeGa | 147 |
| 5.3.4 | RNi_3MnGa ($R = \text{Ce, Pr, Nd, Gd, Tb, Dy and Ho}$) | 151 |
| 5.4 | Summary | 158 |
| 5.5 | References | 159 |
| 6 | Conclusions | 160 |
| 6.1 | Ternary Indides R_2CoIn_8 | 160 |
| 6.2 | Ternary Gallides RNi_4Ga | 162 |
| 6.3 | Pseudo Ternary Gallides (RNi_3FeGa and RNi_3MnGa) | 163 |
| 6.4 | Future Directions | 164 |

FOR AUTHOR USE ONLY

List of Figures

| | | |
|------|--|----|
| 1.1 | Temperature variation of inverse susceptibility for SmRh_4B_4 . | 3 |
| 1.2 | Density of states of free electrons with and without applied field. | 5 |
| 1.3 | Damped oscillatory nature of $RKKY$ interaction with distance. | 6 |
| 1.4 | Radial component of the wave functions plotted for Ce and Tm atoms. | 8 |
| 1.5 | Temperature variation of resistivity for a typical nonmagnetic compound (LaPt_4B). | 10 |
| 1.6 | Behavior of resistivity in the antiferromagnetically ordered state for UPd_2Al_3 . | 11 |
| 1.7 | Schematic curve to show a Kondo effect in resistivity, susceptibility, and inverse susceptibility. Heat capacity curve for a typical heavy fermion behavior. | 13 |
| 1.8 | Heat capacity fit in antiferromagnetically ordered state. | 17 |
| 1.9 | Schematic diagram of the crystal field splitting of $J = 4$ ground state of Pr^{3+} ion. | 18 |
| 1.10 | Curve showing the effect of crystal field on inverse susceptibility. | 19 |
| 1.11 | Typical Schottky contribution to the heat capacity with a fit. | 20 |
| 1.12 | Peak shift with frequency for a typical spin glass compound. | 22 |
| 1.13 | The shift in T_f with frequency for a spin glass system fitted to Vogel-Fulcher law. | 23 |
| 2.1 | Schematic diagram for diffraction of X-ray from the parallel atomic planes. | 26 |
| 2.2 | Top view of the resistivity puck used for resistivity measurement in PPMS. | 28 |
| 2.3 | Schematic diagram of a Vibrating Sample Magnetometer. | 30 |
| 2.4 | A simplified view of a SQUID magnetometer. | 31 |
| 2.5 | SQUID voltage produced when the sample scans across the pickup coils. | 32 |
| 2.6 | Schematic diagram of a heat capacity puck in PPMS. | 34 |
| 2.7 | Temperature variation of the platform in HC puck during a measurement cycle. | 34 |
| 3.1 | a): X-ray diffraction pattern of Gd_2CoIn_8 before annealing and b): Rietveld analysis of the diffraction pattern of Gd_2CoIn_8 after annealing. | 39 |
| 3.2 | Unit cell structure of R_2CoIn_8 . | 40 |
| 3.3 | a): Variation of lattice parameters with rare earths for R_2CoIn_8 compounds and b): Variation of unit cell volume with rare earths. | 41 |

| | | |
|------|---|----|
| 3.4 | Temperature variation of susceptibility for Y_2CoIn_8 . | 44 |
| 3.5 | a): Temperature variation of susceptibility for Ce_2CoIn_8 and b): Temperature variation of inverse susceptibility for the same. | 45 |
| 3.6 | Magnetic isotherm at 2 K for Ce_2CoIn_8 . | 46 |
| 3.7 | a): Temperature variation of susceptibility for Pr_2CoIn_8 and b): Temperature variation of inverse susceptibility for the same. | 47 |
| 3.8 | Magnetic isotherm at 2 K for Pr_2CoIn_8 . | 48 |
| 3.9 | Crystal field fit to inverse susceptibility for Pr_2CoIn_8 . | 48 |
| 3.10 | Temperature variation of resistivity for Y_2CoIn_8 . | 50 |
| 3.11 | a): Temperature variation of resistivity for Ce_2CoIn_8 and b): Magnetic contribution to the resistivity for the same. | 51 |
| 3.12 | Total resistivity of Pr_2CoIn_8 with a fit and a spin disorder resistivity for the same. | 53 |
| 3.13 | Heat capacity of Y_2CoIn_8 . | 54 |
| 3.14 | a): C/T vs T^2 curve with a straight line fit and b): Magnetic entropy for Ce_2CoIn_8 . | 55 |
| 3.15 | C/T vs T^2 curve for Pr_2CoIn_8 with a straight line fit and with an inset showing its entropy. | 57 |
| 3.16 | Schottky anomaly of Pr_2CoIn_8 with a fit. | 58 |
| 3.17 | Neel temperature of R_2CoIn_8 compounds compared with de-Gennes scaling. | 59 |
| 3.18 | a): Temperature variation of susceptibility with various applied fields. b): Inverse susceptibility for the same with a fit and an inset showing its magnetic isotherm. | 61 |
| 3.19 | Heat capacity curve for Gd_2CoIn_8 with an inset showing its magnetic entropy. | 62 |
| 3.20 | a): Temperature variation of resistivity for Gd_2CoIn_8 . b): magnetoresistance for the same at 2 K. | 63 |
| 3.21 | a): Susceptibility of Dy_2CoIn_8 at various fields. b): Inverse susceptibility for the same with a Curie-Weiss fit. | 64 |
| 3.22 | Magnetic Isotherm for Dy_2CoIn_8 at various temperatures. | 65 |
| 3.23 | Low temperature heat capacity for Dy_2CoIn_8 at various fields. | 66 |
| 3.24 | Resistivity vs temperature curve for Dy_2CoIn_8 . | 67 |
| 3.25 | Low temperature ordered state resistivity for Dy_2CoIn_8 . | 69 |
| 3.26 | Magnetoresistance of Dy_2CoIn_8 at 2 K. | 68 |
| 3.27 | a): Temperature variation of susceptibility for Ho_2CoIn_8 at various fields. b): | |

| | |
|--|----|
| Magnetic isotherms at various temperatures. | 69 |
| 3.28 Low temperature heat capacity of Ho_2CoIn_8 at various fields. | 70 |
| 3.29 a): Temperature variation of resistivity of Ho_2CoIn_8 with a fit. b): Resistivity for the same in the ordered state with a fit. | 71 |
| 3.30 Magnetoresistance for Ho_2CoIn_8 at 2 K. | 72 |
| 3.31 Temperature variation of Susceptibility for Sm_2CoIn_8 at various fields. | 73 |
| 3.32 Magnetic isotherm for Sm_2CoIn_8 at 2 K. | 74 |
| 3.33 Temperature variation of inverse susceptibility for Sm_2CoIn_8 with a fit. | 74 |
| 3.34 a): Temperature variation of resistivity for Sm_2CoIn_8 . b): Resistivity for the same in the ordered state with a fit. | 75 |
| 3.35 Magnetoresistance for Sm_2CoIn_8 at 2 K. | 76 |
| 3.36 Low temperature heat capacity for Sm_2CoIn_8 at various fields. | 76 |
| 3.37 Susceptibility of Tb_2CoIn_8 at various fields. | 77 |
| 3.38 Magnetic isotherm for Tb_2CoIn_8 at 2 K. | 78 |
| 3.39 Low temperature heat capacity for Tb_2CoIn_8 at various fields with an inset showing C/T vs T curve. | 79 |
| 3.40 Temperature variation of resistivity in the ordered state, with an inset showing its magnetoresistance at 2 K. | 80 |
| 4.1 Rietveld Refinement of X-ray pattern of SmNi_4Ga . | 84 |
| 4.2 Crystal structure of RNi_4Ga compounds. | 85 |
| 4.3 Unit cell volume and lattice parameters for RNi_4Ga compounds with rare earths. | 86 |
| 4.4 Temperature variation of susceptibility for LaNi_4Ga and LuNi_4Ga . | 88 |
| 4.5 Susceptibility vs Temperature curves under FC and ZFC conditions for RNi_4Ga ($R = \text{Pr, Nd and Sm}$) compounds. | 89 |
| 4.6 Susceptibility vs Temperature curves under FC and ZFC conditions for RNi_4Ga ($R = \text{Gd, Tb and Dy}$) compounds. | 90 |
| 4.7 Susceptibility vs Temperature curves under FC and ZFC conditions for RNi_4Ga ($R = \text{Ho, Er and Tm}$) compounds. | 91 |
| 4.8 Magnetic Isotherm for RNi_4Ga ($\text{Pr, Nd, Sm, Gd and Tb}$) compounds at 2 K. | 92 |
| 4.9 Magnetic Isotherm for RNi_4Ga ($\text{Dy, Ho, Sm, Er and Tm}$) compounds at 2 K. | 93 |

| | | |
|------|---|-----|
| 4.10 | Real part of the AC susceptibility of RNi_4Ga series of compounds. a): $R = Er, Gd, Pr, Tb$ and Nd . b): $R = Ho, Sm, Dy$ and Tm . | 94 |
| 4.11 | Inverse susceptibility vs Temperature curve for RNi_4Ga (Pr, Nd, Gd and Tb) compounds. The line through the data points represents the Curie-Weiss fit. | 96 |
| 4.12 | Inverse susceptibility vs Temperature curve for RNi_4Ga (Dy, Ho, Er and Tm) compounds. The line through the data points represent the Curie-Weiss fit. | 97 |
| 4.13 | Temperature variation of susceptibility for $SmNi_4Ga$. | 98 |
| 4.14 | T_C of RNi_4Ga compounds compared with the de-Gennes scaling. | 99 |
| 4.15 | Heat capacity curve for $LaNi_4Ga$ and $PrNi_4Ga$. | 101 |
| 4.16 | Heat capacity curves for RNi_4Ga ($R = Sm, Tb$ and Gd) compounds. | 102 |
| 4.17 | Heat capacity curves for RNi_4Ga ($R = Dy, Er$ and Tm) compounds. | 103 |
| 4.18 | Real part of the AC susceptibility of $GdNi_4Ga$ with various DC fields. Inset shows an imaginary part. | 104 |
| 4.19 | C/T vs T curve for $GdNi_4Ga$ with an inset showing its entropy. | 105 |
| 4.20 | C/T vs T^2 curve for $LaNi_4Ga$. | 106 |
| 4.21 | Density of states for $3d$ electrons with spin up and spin down states. | 107 |
| 4.22 | AC susceptibility for $TbNi_4Ga$. | 108 |
| 4.23 | C/T vs T curve for $TbNi_4Ga$ with an inset showing its entropy. | 109 |
| 4.24 | Magnetic isotherm for $TbNi_4Ga$ at 2 K. | 110 |
| 4.25 | AC susceptibility of $SmNi_4Ga$. | 110 |
| 4.26 | C/T vs T curve for $SmNi_4Ga$. | 111 |
| 4.27 | Magnetic Isotherm for $SmNi_4Ga$ at 2 K. | 111 |
| 4.28 | Magnetization vs Temperature plot for $SmNi_4Ga$ at various fields. | 112 |
| 4.29 | Variation of Coercive field with temperature for $SmNi_4Ga$. | 113 |
| 5.1 | Rietveld analysis of the X-ray pattern of YNi_3FeGa and $PrNi_3MnGa$. | 118 |
| 5.2 | Crystal structure of RNi_3TGa ($T = Mn$ and Fe) compounds. | 119 |
| 5.3 | Lattice parameters of RNi_3FeGa and RNi_3MnGa series of compounds plotted against corresponding rare earths. | 121 |
| 5.4 | Unit cell volumes for RNi_3FeGa and RNi_3MnGa series of compounds. | 122 |
| 5.5 | a): Temperature variation of susceptibility for YNi_3FeGa . b): Magnetic isotherm | |

| | | |
|-------------|---|-----|
| | for the same at 2 K. c): χ^{-1} vs T plot for the same. | 124 |
| 5.6 | a): Real part, b): Imaginary part of the AC susceptibility for YNi_3FeGa . c): Variation of T_f with frequency fitted to Vogel-Fulcher law. | 125 |
| 5.7 | Thermoremanent magnetization as a function of time at 2 K. | 127 |
| 5.8 | a): Temperature variation of susceptibility for LaNi_4Ga . b): Magnetic isotherm for the same at 2 K. c): χ^{-1} vs T plot for the same. | 128 |
| 5.9 | a): Real part and b): Imaginary part of susceptibility for LaNi_3FeGa . | 129 |
| 5.10 | a): Temperature variation of susceptibility, b): Inverse susceptibility and c): magnetic isotherm at 2 K for YNi_3MnGa . | 130 |
| 5.11 | a): Real part and b): Imaginary part of AC susceptibility for YNi_3MnGa . | 131 |
| 5.12 | a): Temperature variation of susceptibility, b): Inverse susceptibility and c): magnetic isotherm at 2 K for LaNi_3MnGa . | 132 |
| 5.13 | Heat capacity plot for a): YNi_3FeGa and b): LaNi_3FeGa . | 133 |
| 5.14 | Heat capacity plot for a): YNi_3MnGa and b): LaNi_3MnGa . | 134 |
| 5.15 | a): Temperature variation of ZFC susceptibility with inverse susceptibility as an inset, b): Magnetic isotherm with an inset showing the derivative of susceptibility and c): Heat capacity for CeNi_3FeGa . | 137 |
| 5.16 | a): Temperature variation of susceptibility under ZFC and FC conditions with an inset showing the derivative of susceptibility, b): Magnetic isotherm at 2 K and c): Heat capacity for PrNi_3FeGa . | 138 |
| 5.17 | a): Temperature variation of susceptibility under ZFC and FC conditions with an inset showing the derivative of susceptibility, b): Magnetic isotherm at 2 K and c): Heat capacity for GdNi_3FeGa . | 139 |
| 5.18 | a): Temperature variation of susceptibility under ZFC and FC conditions with an inset showing the derivative of susceptibility, b): Magnetic isotherm at 2 K and c): Heat capacity for NdNi_3FeGa . | 140 |
| 5.19 | a): Temperature variation of susceptibility under ZFC and FC conditions with an inset showing the derivative of susceptibility and b): Magnetic isotherm at various temperatures for SmNi_3FeGa . | 141 |
| 5.20 | a): Temperature variation of susceptibility under ZFC and FC conditions with an | |

| | | |
|------|--|-----|
| | inset showing the derivative of susceptibility and b) : Magnetic isotherm at 2 K for TbNi ₃ FeGa. | 142 |
| 5.21 | a) : Temperature variation of susceptibility under ZFC and FC conditions with an inset showing the derivative of susceptibility, b) : Magnetic isotherm at 2 K and c) : Heat capacity for DyNi ₃ FeGa. | 143 |
| 5.22 | a) : Temperature variation of susceptibility under ZFC and FC conditions with an inset showing the derivative of susceptibility and b) : Magnetic isotherm at 2 K for HoNi ₃ FeGa. | 144 |
| 5.23 | a) : Temperature variation of susceptibility under ZFC and FC conditions and b) : Magnetic isotherm at 2 K. | 145 |
| 5.24 | a) : Field cooled susceptibility near the T_C at various applied fields, b) : magnetization in zero field after cooling the sample in ± 50 kOe and c) : Magnetic isotherm at various temperatures near the compensation temperature for ErNi ₃ FeGa. | 148 |
| 5.25 | Temperature variation of susceptibility under ZFC and FC conditions with an inset showing the derivative of susceptibility for CeNi ₃ MnGa. | 152 |
| 5.26 | a) : Temperature variation of susceptibility under ZFC and FC conditions with an inset showing the derivative of susceptibility and b) : Magnetic isotherm at 2 K for PrNi ₃ MnGa. | 153 |
| 5.27 | a) : Temperature variation of susceptibility under ZFC and FC conditions with an inset showing the derivative of susceptibility and b) : Magnetic isotherm at 2 K for NdNi ₃ MnGa. | 154 |
| 5.28 | a) : Temperature variation of susceptibility under ZFC and FC conditions with an inset showing the derivative of susceptibility and b) : Magnetic isotherm at 2 K for GdNi ₃ MnGa. | 155 |
| 5.29 | a) : Temperature variation of susceptibility under ZFC and FC conditions with an inset showing the derivative of susceptibility and b) : Magnetic isotherm at 2 K for TbNi ₃ MnGa. | 156 |
| 5.30 | a) : Temperature variation of susceptibility under ZFC and FC conditions with an inset showing the derivative of susceptibility and b) : Magnetic isotherm at 2 K for DyNi ₃ MnGa. | 157 |

List of Tables

| | | |
|------------|---|-----|
| 3.1 | Lattice Parameters, unit cell volume and c/a ratio for $R_2\text{CoIn}_8$ compounds. | 42 |
| 3.2 | Crystallographic parameters for Gd_2CoIn_8 compound. | 43 |
| 3.3 | Energy levels, state representation, degeneracy and wave functions for crystal field split $J = 4$ state for Pr_2CoIn_8 . | 49 |
| 3.4 | Neel temperatures for $R\text{In}_3$ and $R_2\text{CoIn}_8$ series of compounds. Paramagnetic Curie temperature and effective magnetic moment for $R_2\text{CoIn}_8$ compounds are also given. | 61 |
| 4.1 | Crystallographic parameters for $R\text{Ni}_4\text{Ga}$ compounds. The occupancy is compared with the corresponding parent compound $R\text{Ni}_5$. | 87 |
| 4.2 | Comparison of the lattice parameters (a and c) and the unit cell volume of $R\text{Ni}_5$ and $R\text{Ni}_4\text{Ga}$ compounds. | 95 |
| 4.3 | Transition temperature of $R\text{Ni}_5$ and $R\text{Ni}_4\text{Ga}$ series of compounds. Paramagnetic Curie temperature, effective magnetic moment and saturation moment for $R\text{Ni}_4\text{Ga}$ compounds are also listed. | 100 |
| 5.1 | Crystallographic parameters for $R\text{Ni}_3\text{TGa}$ ($T = \text{Mn}$ and Fe) compounds. | 120 |
| 5.2 | Lattice parameters of $R\text{Ni}_3\text{FeGa}$ and $R\text{Ni}_3\text{MnGa}$ series of compounds. | 120 |
| 5.3 | Comparison between the T_c s of $R\text{Ni}_4\text{Ga}$ and $R\text{Ni}_3\text{FeGa}$ series of compounds. Experimental saturation magnetization at 90 kOe and 2 K is compared with the expected value. Coercive Field for $R\text{Ni}_3\text{FeGa}$ at 2 K is given. | 149 |
| 5.4 | Comparison of the T_c of $R\text{Ni}_4\text{Ga}$, $R\text{Ni}_3\text{FeGa}$ and $R\text{Ni}_3\text{MnGa}$ series of compounds. Experimental saturation magnetization at 90 kOe and 2 K compared with the expected value. Coercive Field for $R\text{Ni}_3\text{MnGa}$ and $R\text{Ni}_3\text{FeGa}$ at 2 K is given. | 150 |

Chapter 1

Introduction

Magnetism is one of the oldest branches of science. A thorough research in this area is going on since last few hundreds of years. In the early days, the research was focused on explaining the behavior of iron and related compounds and their applications. Theoretically, the research in this field was enhanced after the discovery of Quantum mechanics. Later on, a penetrating work by J.H. Van Vleck [1] changed the scenario. Experimentally the research was boosted by the discovery of superconductors, rare earths and various technologies providing very low temperatures. This also has created a great revolution in the area of condensed matter physics, making it a branch of physics providing a great support to the recent technology advancements. Magnetism in rare earth transition metal intermetallic systems is still under investigation as they offer a great variety of magnetic materials for tailoring the magnetic properties such as coercivity, Curie temperature, anisotropy, magnetization, etc. for practical applications.

In this book we are investigating a number of rare earth based intermetallic compounds. In case of the rare earths, the f shell lies deeper inside the atom and hence remains unaffected from the orbital overlap except in the case of Ce and Yb compounds. Hence the rare earth ions retain their moment in the compounds and their ground state properties are governed by the Hund's rule. The $4f$ ions interact between themselves via polarization of the conduction electrons (RKKY interaction). In case of the Ce (in few cases Yb) atoms, the orbital overlap is such that the f electrons lie submerged in the sea of the conduction electrons. This gives rise to a variety of interesting properties like Heavy fermion, dense Kondo lattice, Fermi liquid behavior, valence fluctuation, etc. In the case of other rare earths, the f orbital shows various types of magnetic ordering. This chapter is aimed to present a discussion on those features of the rare earth magnetism that forms a basis for the interpretation of the data presented in the subsequent chapters.

1.1 Paramagnetism

1.1.1 Spin Paramagnetism

Magnetization in the rare earth based compounds (compounds where only rare earth is magnetic) arises due to the unpaired electrons in the $4f$ shell. Due to the localized behavior of

the $4f$ shell, the magnetic behavior of the rare earth can reasonably be described by the respective free trivalent ion properties. The rare earth ion is generally a trivalent ion because it loses the $5d^1$ and $6s^2$ electrons in the bond formation to make the conduction band. Now since the f -orbital is less affected by the surrounding, the $L-S$ coupling is maintained and J is a good quantum number. In such cases, all the three Hund's rules are applicable to the rare earth ion. The details of the Hund's rule are found elsewhere [2]. The rare earth ions with a finite value of J interact to give rise to various types of magnetic ordering. At high temperatures (well above the magnetic ordering), because of the high thermal energy ($k_B T$), a positive contribution from the non-interacting magnetic moments arises, called the spin paramagnetism or the *Langevin paramagnetism*. The measured magnetization is the time average of the alignment of the moments under an externally applied magnetic field. The magnetization in such cases is given by,

$$M = N_A g J \mu_B B_J(x) \quad (1.1)$$

where N_A is the Avogadro number (if calculated in moles), g is the Lande factor, J is the total angular momentum quantum number, μ_B is the Bohr magneton, $B_J(x)$ is the Brillouin function and $x = \mu H / k_B T$, where H is the externally applied field. The function $B_J(x)$ is defined by

$$B_J(x) = \frac{2J+1}{2J} \coth\left(\frac{(2J+1)x}{2J}\right) - \frac{1}{2J} \coth\left(\frac{x}{2J}\right) \quad (1.2)$$

At high temperatures where $x \ll 1$, equation (1.1) reduces to

$$M \cong \frac{BN_A J(J+1)g^2 \mu_B^2}{3k_B T} = \frac{BN_A p^2 \mu_B^2}{3k_B T} = \frac{BC}{T} \quad (1.3)$$

where p is the effective moment given by $p = g[J(J+1)]^{\frac{1}{2}}$, B is the applied magnetic field and C is the Curie constant. The above equation is called the *Curie law*. The exchange interaction between the magnetic ions cause magnetic ordering below a certain temperature. In such a case, the expression for the magnetic susceptibility is given by the Curie Weiss Law,

$$\chi = \frac{C}{T - \theta_p} \quad (1.4)$$

where θ_p is the paramagnetic Curie temperature. The temperature variation of inverse susceptibility of the localized spins above the magnetic ordering temperature according to the above expression should be linear in T . A negative value of θ_p in the above expression represents an an-

tiferromagnetic interaction between the localized spins and a positive value indicates a ferromagnetic interaction. The above relation takes a more general form when the temperature independent Van-Vleck susceptibility term (χ_0) is included,

$$\chi = \frac{C}{(T - \theta_p)} + \chi_0 \quad (1.5)$$

Generally the Van-Vleck susceptibility is negligible compared to the susceptibility of the magnetic rare earth ions. But in some of the cases it dominates, giving non linearity in the behavior of the inverse susceptibility curve.

In some of the cases like Sm^{3+} and Eu^{3+} ions, the excited states lie near to the ground state. In such cases the paramagnetic susceptibility will not follow the simple Curie-Weiss law and the

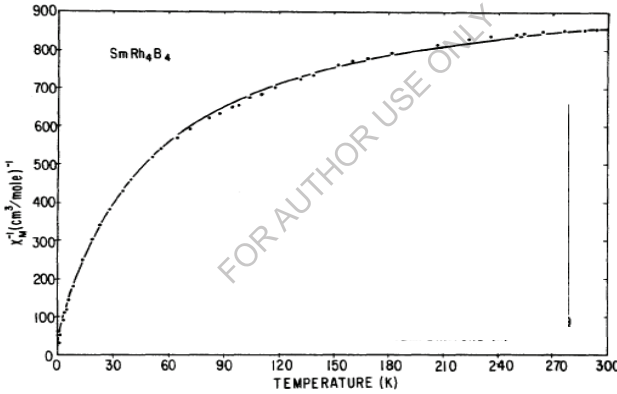


Fig. 1.1: χ^{-1} vs T plot for SmRh_4B_4 fitted to Eq. (1.7) [3].

modified equation is given by [1]

$$\chi = N_A \frac{\sum_{L-S}^{L+S} \left[g_J^2 \mu_B^2 J(J+1) / 3k_B T \right] + \alpha_J (2J+1) e^{-E_J^0 / k_B T}}{\sum_{L-S}^{L+S} (2J+1) e^{-E_J^0 / k_B T}} + \chi_0 \quad (1.6)$$

where L is the total orbital angular momentum and S is the total spin. The α_J term arises from the joint contribution of the high frequency elements of the paramagnetic moments (particularly when the multiplet intervals are small compared to $k_B T$) and the diamagnetic contribution. This

term originates from the *non permanent* behavior of the resulting magnetic moment which can have different relative alignment of \vec{L} and \vec{S} . E_J^0 is the zeroth order energy of the J^{th} level. For Sm^{3+} ions, the first excited state lies very close to the ground state ($\Delta E_{7/2-5/2} \approx 1400$ K) and hence the above equation can be approximated to (for first excited state only),

$$\chi = \frac{N_A}{k_B} \left(\frac{\mu_{\text{eff}}^2}{3(T - \theta_p)} + \frac{\mu_B^2}{\delta} \right) \quad (1.7)$$

where $\delta = 7\Delta E/20$ and ΔE is the difference between the ground state and the first excited state. For Sm^{3+} ion, the first term in the above equation represents a Curie-Weiss contribution from $J = 5/2$ ground state, while the second term is the temperature independent Van-Vleck correction arising from the accessible first excited state, $J = 7/2$. In the absence of crystal field effects, the probable value of μ_{eff} and δ is $0.845 \mu_B$ and 490 K, respectively. Figure 1.1 shows the inverse susceptibility of SmRh_4B_4 [3] with a fit to Eq. (1.7) for $\delta = 470$ K and $\mu_{\text{eff}} = 0.63 \mu_B$. The low value of μ_{eff} was attributed to the crystal field effects.

1.1.2 Van-Vleck Paramagnetism

If the total orbital angular momentum of the system in the ground state is zero ($J = 0$), then in such cases there will be no paramagnetism because

$$\langle 0 | \hat{\mu} | 0 \rangle = g_J \mu_B \langle 0 | J | 0 \rangle = 0 \quad (1.8)$$

where $\hat{\mu}$ is the magnetic moment operator. This implies that the ground state energy of the system does not change if the magnetic field is applied and hence there is no paramagnetic susceptibility. The above equation appears only if the first order perturbation theory is used. The second order perturbation theory includes the excited states with $J \neq 0$ also. In such cases, the expression for the susceptibility can be written as

$$\chi = \frac{N_A}{V} \left(2\mu_B^2 \sum_n \frac{|\langle 0 | (L_z + gS_z) | n \rangle|^2}{E_n - E_0} - \frac{e^2 \mu_0}{6m_e} \sum_{i=1}^Z \langle r_i^2 \rangle \right) \quad (1.9)$$

where m_e is the mass of the electron, μ_0 is the permeability in free space and $\langle r_i \rangle$ is the expectation value of the electron position. The positive first term ($E_n > E_0$) gives the Van-Vleck para-

magnetism and the second term represents the diamagnetic contribution. Both the contributions are independent of temperature.

1.1.3 Pauli Paramagnetism

A brief discussion on Pauli paramagnetism is described here and the details are found elsewhere [4]. The Pauli paramagnetism arises due to the free conduction electrons. Single free electron in a system possesses only a spin angular momentum. It contributes one Bohr magneton to the magnetic moment when the field is applied. In a system with free electrons, the density of

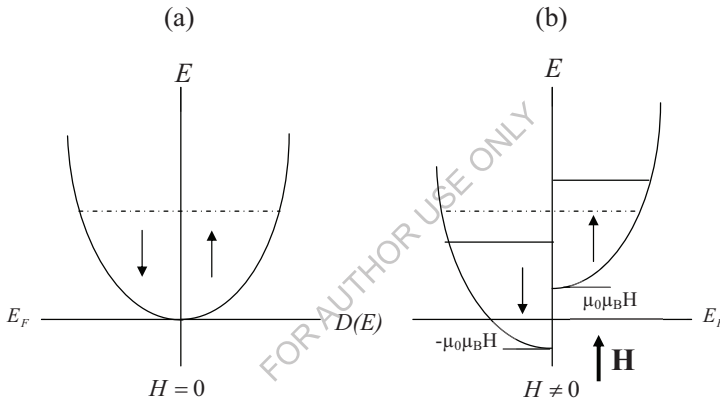


Fig. 1.2: (a): Density of the states for the free electrons with no applied field. The density of states for up and down spins are equal and proportional to \sqrt{E} . (b): Density of states when a magnetic field is applied in the up direction.

states with up spin and down spin of free electrons are equal in the absence of a magnetic field (Fig. 1.2a). When a field H is applied in the upward direction parallel to the up-spins as shown in Fig. 1.2b, the energy of the electrons with up spin will increase by $\mu_B H$ and those with down spin will decrease by $\mu_B H$. The displacement will also change the Fermi level but the new Fermi level will be very close to the original and hence can be considered the same as the original one. In such cases, the net magnetic moment will be the difference between the up and down spin

moments multiplied by the moment per spin. So the net magnetic moment in the direction of the field comes out to be

$$M = \mu_0 \mu_B^2 H D(E_F) \quad (1.10)$$

where $D(E_F)$ is the density of states at the Fermi level and is given by

$$D(E_F) = \frac{3N}{2E_F} \quad (1.11)$$

Substituting Eq. (1.11) in Eq. (1.10) and rearranging it in the form of susceptibility we get

$$\chi = \frac{3N\mu_0\mu_B^2}{2E_F} \quad (1.12)$$

The expression is independent of temperature and is called the Pauli paramagnetic susceptibility. Now there is also diamagnetism arising due to the free electrons, which turn out to be 1/3 of the Pauli paramagnetic contribution and opposite in direction. Considering this, the resultant expression for the Pauli paramagnetic susceptibility can be written as

$$\chi = \frac{N\mu_0\mu_B^2}{E_F} \quad (1.13)$$

1.2 Magnetic Ordering

1.2.1 Indirect Exchange (RKKY)

At high temperatures, $4f$ moments of the rare earth ions behave independent of each other giving rise to spin paramagnetism. At low temperatures the exchange energy dominates and the rare earth ions interact via indirect exchange interaction involving the polarization of the conduction electrons by the rare earth spins. The interaction between any localized spin \vec{S} and the conduction electron spin $\vec{\sigma}$ is given by

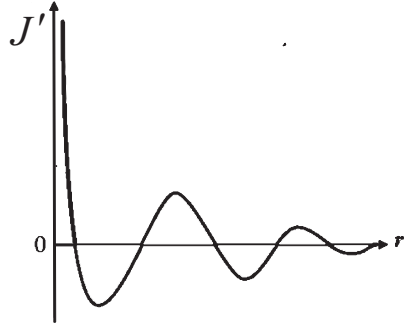


Fig. 1.3: A schematic representation showing variation of indirect exchange integral J' in the neighbourhood of the localized spin S kept at the origin.

$$H_{ex} = -J' \vec{S}_i \cdot \vec{S}_j \quad (1.14)$$

where J' is the exchange integral. Any interaction of this type is known to cause an oscillatory spin polarization of the conduction electrons, depending upon the distance between the two spins. The spin polarization of the conduction electrons acts as a medium for the indirect interaction between the two well separated localized moments. This type of indirect exchange interaction of two localized $4f$ moments via polarization of the conduction electrons is called the *RKKY* interaction. The *RKKY* interaction between the two localized spins \vec{S}_i and \vec{S}_j is given by [5]

$$H_{RKKY} = -\sum_{i,j} J''(R_{ij}) \vec{S}_i \cdot \vec{S}_j \quad (1.15)$$

where $J''(R_{ij})$ is the effective exchange integral between the localized spins located at \vec{R}_i and \vec{R}_j . In the *RKKY* theory, the expression for the exchange integral in the simplified form is given by [6]

$$J''(R_{ij}) = \frac{9\pi J'^2}{E_F} F(2k_F R_{ij}) \quad (1.16)$$

where k_F is the Fermi-wave vector, E_F is the Fermi energy, J is the exchange integral and $F(x)$ is the function having an oscillatory nature given by

$$F(x) = \frac{x \cos(x) - \sin(x)}{x^4}, \quad x = 2k_F R_{ij} \quad (1.17)$$

From the above equations, it is clear that the exchange integral is isotropic and has an oscillatory nature w.r.t. the distance between the interacting ions as shown in Fig. 1.3. So depending upon the distance between the ions, the exchange integral becomes positive or negative (Fig. 1.3) resulting in ferromagnetic or antiferromagnetic interaction.

RKKY Theory Applied to Rare Earths:

In the case of rare earth elements, the f orbital lies deep in the atom covered by $5s$, $5d$ and $6s$ as shown in Fig. 1.4 for the case of Tm. Thus, the f orbitals are well separated and shielded from each other. Due to the spatial extent of the f orbital, the magnetic coupling has to proceed indirectly since there is no overlap between the f wave functions. Also the $L-S$ coupling remains intact and J (total angular momentum) is considered as a good quantum number. In such cases the Hamiltonian in equation (1.14) can be written as

$$H_{exch} = -(g_J - 1)J'J \cdot \sigma \quad (1.18)$$

where J' is the exchange integral between the conduction electron and the localized moment, σ is the conduction electron spin and g_J is the Lande g factor. Using the above equation, the effective exchange coupling between the rare earth ions can be written as

$$J''(R_{ij}) = \frac{9\pi(g_J - 1)^2 J'^2}{E_F} F(2k_F R_{ij}) \quad (1.19)$$

Considering this expression within the framework of molecular field theory, de-Gennes showed that the paramagnetic Curie temperature θ_p is given by [7]

$$\theta_p = -\frac{3\pi^2 J'}{k_B E_F} (g_J - 1)^2 J(J+1) \sum_i F(2k_F R_{ij}) \quad (1.20)$$

where n is the average conduction electron per atom and the summation is taken over all the magnetic moment sites. The above equation is well defined in the cases where J is a good quantum number (especially, rare earth compounds where only the rare earth has moment). The deduction is that the paramagnetic Curie-temperature θ_p within a class of the analogous intermetal-

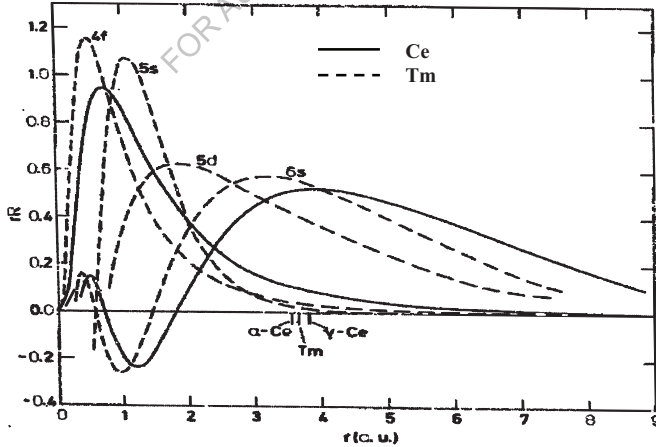


Fig.1.4 The radial component of the wave functions plotted for Ce and Tm. Fig. from [8].

lic rare-earth compounds should scale as $(g_J - 1)^2 J(J+1)$ and this factor is called the *de-Gennes factor*.

1.2.2 Direct Exchange:

The magnetic moment requires a media for interacting when they are far apart (*RKKY* interaction) but they interact directly when brought close to each other. Such a behavior happens in the case of transition elements where the $3d$ orbital lies in the peripheral. The large spatial extent of the $3d$ orbital causes it to overlap with the $3d$ orbital of the neighboring atom. This leads to a $3d$ band and in many cases it is possible that the electrons become free. The strong exchange interaction among the $3d$ electrons leads to the situation that the spin up and spin down electrons no longer remains equal and this give rise to magnetism. According to the Heisenberg theory, if two atoms i and j have spin angular momentum \vec{S}_i and \vec{S}_j , respectively then the exchange energy between them is given by

$$E_{ex} = -2J_{ex} \vec{S}_i \cdot \vec{S}_j = -2J_{ex} S_i S_j \cos \phi \quad (1.21)$$

where J_{ex} is the exchange integral and ϕ is the angle between the spins. If J_{ex} is positive, E_{ex} is minimum when the spins are parallel ($\cos \phi = 1$). If J_{ex} is negative, E_{ex} is minimum when the spins are antiparallel ($\cos \phi = -1$). The interactions depend upon the distance between the two atoms.

1.3 Transport Property

The transport property is one of the fundamental tools for investigating the conduction mechanism of the materials. The conduction mechanism is highly affected by the magnetic behavior of the material; hence it also becomes an important tool to study the magnetic property of the material. The transport property is mainly explored through the electrical and thermal conductivities of the material. Here we will discuss only the electrical conductivity of the material with various contributions to it (relevant to the work in this thesis). The major contribution to resistivity of any material arises from the phonons. The temperature variation of the phonon contribution is proportional to T^5 . A general expression describing the temperature variation of the pure pho-

non contribution was derived by Bloch which is known as the Bloch-Gruneisen relation. It has the form given by [8],

$$\rho(T) = \rho_0 + 4R\theta_D \left(\frac{T}{\theta_D} \right)^5 \int_0^{\frac{\theta_D}{T}} \frac{x^5 dx}{(e^x - 1)(1 - e^{-x})}, \quad x = \frac{\theta_D}{T} \quad (1.22)$$

where ρ_0 is the temperature independent residual resistivity and the second term which goes as T^5 accounts for electron-phonon scattering process. The notation θ_D represents the Debye temperature and the coefficient R stands for the electron phonon interaction. ρ_0 arises at very low temperatures due to the scattering of the conduction electrons by the impurities and imperfections in the sample. At low temperatures, the phonon contribution becomes vanishingly small and hence such contribution dominates. The smaller the value of ρ_0 , the better is the sample quality. In many of the metallic compounds it is considered as one of the parameters describing the quality of the sample. The ratio of room temperature resistivity to that of ρ_0 is reported to check for the sample quality. The above formula is used for fitting the temperature variation of resistivity of a purely nonmagnetic material. A typical resistivity behavior of the nonmagnetic LaPt₄B is shown in Fig. 1.5 with a fit to Eq. (1.22). If the material is magnetic then there are various other contributions to the resistivity. For pure (not diluted) magnetic materials in the paramagnetic state, the conduction electrons are scattered by the disordered spins. This gives rise to the spin disorder resistivity in the paramagnetic state. The spin disorder resistivity is independent of the temperature. In the ordered state the spin disorder resistivity vanishes, but the phonon contribution still remains. Also in the ordered state, the resistivity is affected by the magnons and the anisotropic behavior of the compound. To get an expression for the magnetic

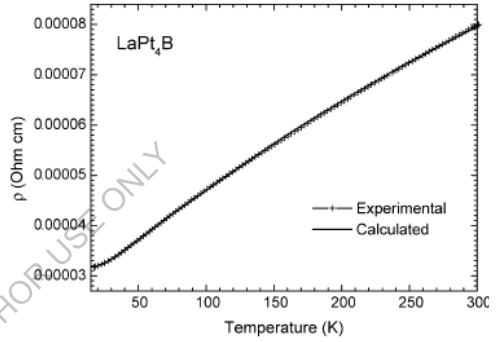


Fig. 1.5: Resistivity of a typical nonmagnetic compound fitted to Eq. 1.22. The figure is taken from [9].

contribution to the resistivity, we consider the magnon dispersion relation for the anisotropic materials given by [10]

$$E_k = \Delta + Dk^2 \quad (1.23)$$

where Δ accounts for the anisotropy gap and D is the spin wave stiffness. The contribution to the electrical resistivity arising from the spin wave is given by [11]

$$\rho_M = A\beta \int d\omega \frac{\omega}{\sinh^2(\beta\omega/2)} \int_0^{2k_F} k^3 \pi [\delta(\omega - E_k) + \delta(\omega + E_k)] dk \quad (1.24)$$

where $\beta = 1/k_B T$, $A = (1/3\hbar)(4\pi n G^2 / en)$.

n is the charge density, ω is the frequency of the spinwave and k is the wave vector of the conduction electrons. G is the coupling between the electrons and the rare earth moments, E_k is the energy of the magnetic excitations which scatter the conduction electrons and the term in the square bracket represents the imaginary part of the susceptibility. Solving the above equation for ferromagnetic materials with $k_B T \ll \Delta$ and E_k given by (1.23) we find

$$\rho_M = a\Delta T e^{-\Delta/k_B T} \left[1 + 2 \frac{k_B T}{\Delta} \right] \quad (1.25)$$

where a is a constant which depends on the material. This equation describes the temperature variation of the electrical resistivity in the absence of a magnetic field. For an isotropic ferromagnet, $\rho_m \propto T^{-2}$ since $\Delta = 0$. Equation (1.23) can be solved for antiferromagnets by substituting the imaginary part of the susceptibility by [12]

$$\text{Im } \chi(k, \omega) = \frac{\pi}{\varepsilon_k} [\delta(\omega - \omega_k^+) + \delta(\omega + \omega_k^-)] \quad (1.26)$$

where $\varepsilon_k = \frac{1}{2}(\omega_k^+ - \omega_k^-) = \sqrt{\Delta^2 + Dk^2}$ and $\omega_k^\pm = -\mu_{\text{eff}} H \pm \varepsilon_k$

The solution of equation (1.24) with $H = 0$ gives the final result for the resistivity as

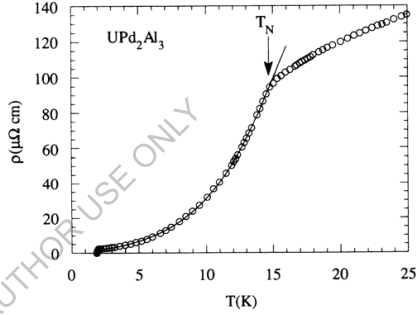


Fig.1.6: Resistivity fit in the antiferromagnetically ordered state to Eq. 1.27. Fig. from [13].

$$\rho_M \approx b\Delta^2 \sqrt{\frac{k_B T}{\Delta}} e^{-\Delta/k_B T} \left[1 + \frac{2}{3} \left(\frac{k_B T}{\Delta} \right) + \frac{2}{15} \left(\frac{k_B T}{\Delta} \right)^2 \right] \quad (1.27)$$

where b is a constant. The above equation can be used for fitting the resistivity of magnetically anisotropic materials in the antiferromagnetically ordered state under zero applied fields. A typical fit for UPd_2Al_3 [13] is shown in Fig. 1.6 with $\rho_0 = 1 \mu\Omega\text{-cm}$, $b = 24.1 \mu\Omega\text{-cm/K}^2$. For isotropic antiferromagnets ($\Delta = 0$), (1.24) has to be solved independently, which gives the resistivity $\rho_m \propto T^3$.

1.4 Kondo Effect (Single Ion and Kondo Lattices)

In the case of very dilute magnetic alloys (Fe in Au at concentration of ~ 15 ppm), we have a very few localized spins and are far apart to interact. In such cases, if the spins are bathed in the sea of conduction electrons (localized spins overlap with the conduction electrons), it gives rise to a strong interaction between the conduction electrons and the localized spins. At high temperatures, the magnetic moments behave like free paramagnetic moments but below a characteristic temperature, known as the Kondo Temperature (T_K), the interaction between the magnetic moments and the conduction electrons forces the impurity spins to become nonmagnetic. This is because the conduction electrons begin to form a cloud of opposite-spin polarization around the impurity spin resulting in a quasi bound state. This process of screening of a magnetic impurity by the conduction electrons is known as the *Kondo effect* (or *Single Ion Kondo effect*). This effect can be seen in the magnetization as well as the resistivity behavior of the compounds. The magnetization falls below its free moment value and the inverse susceptibility shows a large value of negative paramagnetic Curie temperature (Fig. 1.7d). The resistivity of metallic compounds does not decrease monotonically with temperature but rather passes through minima and saturates at low temperatures (Fig. 1.7a). This anomalous behavior in the resistivity was explained by J. Kondo using the perturbation calculations [14]. He showed that the above effect leads to an increasing $\ln(T)$ term in resistivity with decreasing temperature. The exact expression for the resistivity is given by

$$\rho_{mag} = \rho_0 + c \ln(T) \quad (1.28)$$

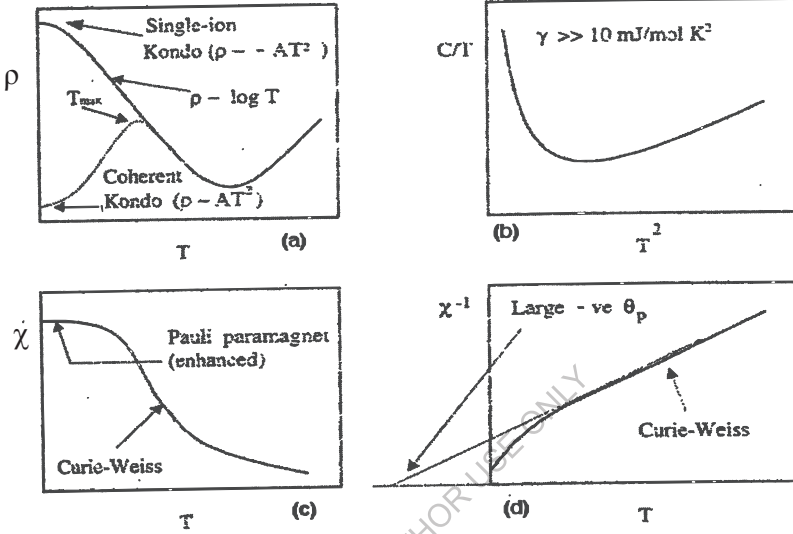


Fig. 1.7: (a) Resistivity behavior of Single ion Kondo effect and Kondo lattice behavior. **(b):** Heat capacity behavior of a typical heavy fermion compound. **(c):** Susceptibility of a Kondo compound and a nonmagnetic heavy fermion. **(d):** Inverse susceptibility of a Kondo compound.

where ρ_0 is the residual resistivity, c is a constant given by $c = \frac{3zJ'}{E_F}$ and z is the number of free electrons per unit cell. Here J' is always negative because of the antiferromagnetic coupling between the spins and the conduction electrons. Hence the formula used to fit the experimental data is

$$\rho_{mag} = \rho_0 - c \ln(T) \quad (1.29)$$

At very low temperatures the Kondo interaction binds the conduction electrons to the impurity spins to form a many body correlated singlet with the binding energy, $E_0 = k_B T_0$. At high temperatures ($T \gg E_0 / k_B$), the impurity spins remain uncompensated, contributing a maximum to the susceptibility. The build up of spin compensating cloud around the impurity occurs gradually with temperature. Hence we define the Kondo temperature as the centre of the broad cross over

regime where the behavior changes gradually from a high temperature uncompensated localized moment behavior to a low temperature Fermi liquid behavior.

Kondo effect takes place in the alloys if the magnetic impurities are well separated and isolated (*RKKY* interaction is negligible). If we have a $3d$ impurity, then at the most 10% of the impurity is favored for the signature of Kondo interaction. However, when the impurity concentration is increased beyond the percolation limit, the $3d$ orbitals of the neighboring impurity ions overlap to form a band and the interaction between the ions takes over resulting in the suppression of Kondo effect. Thus with $3d$ ions, the Kondo effect is limited to low concentration regime where as in the case of $4f$ ions it depends on the condition that f^n and $f^{n\pm 1}$ configurations are close enough in energy to give rise to an intermediate valence character due to the strong hybridization with the conduction electrons. This condition is only satisfied in the case of Ce and Yb ions. These atoms are present at every lattice; hence the behavior is called as *Kondo lattice*. The magnetic susceptibility has a behavior similar to that of the Single ion Kondo effect (Fig. 1.7c and d) where as the resistivity falls after a certain temperature due to coherent scattering of the from the periodically arranged Kondo lattices in contrast to single ion case. At low temperatures the interaction between the Kondo impurity and the conduction electrons is high. In such cases Rajan [15] has shown that the susceptibility ($T \rightarrow 0$) saturates to a value $\chi(0)$ given by

$$\chi(0) = \frac{\nu(\nu^2 - 1)g_J\mu_B^2}{24\pi k_B T_0} \quad (1.30)$$

where $\nu = 2J + 1$ is the degeneracy and T_0 is related to the Kondo temperature by the Wilson number: $W = T_K/T_0 = 1.289$ [16]. The strong interaction also causes increase in the low temperature heat capacity (electronic contribution) of the compounds termed as the Heavy Fermion behavior. The typical values of the electronic coefficient γ are of the order of 100 to 1000 mJ/mole-K compared to 1 to 10 (mJ/mole-K) [17] in case of normal metals. The heat capacity at low temperature has a behavior as shown in Fig.1.7b.

1.5 Thermal Property (Specific Heat)

Specific heat is an important physical property which gives information on phase transitions. All the magnetic orderings would show up as an anomaly at the transition temperature in the specific heat measurements. Specific heat at low temperatures also provides information on

the electronic density of states at the Fermi level and the degeneracy of the ground state of a magnetic ion (from entropy measurement).

The specific heat is defined as the amount of heat required to raise the temperature of unit mass of the material by unit temperature. Keeping all other parameters constant the specific heat is defined as

$$C = \lim_{dT \rightarrow 0} \left(\frac{dE}{dT} \right) \quad (1.31)$$

where dE is the heat required to increase the temperature by dT of unit mass of the material.

The total heat capacity of a substance is the sum of four individual contributions; (i) C_e , the electronic contribution originating from the conduction electrons and filled electron orbitals, (ii) C_l , the lattice contribution originating from the phonons, (iii) C_{mag} , the magnetic contribution originating from the unpaired electrons and (iv) C_n , the nuclear contribution originating from the interaction of the nuclear moments with the effective magnetic field at the site of the nucleus. The nuclear contribution is very less and dominant only at low temperatures (< 1 K). Hence its contribution is neglected in our analysis, where the data is available only down to 1.8 K. Hence the total heat capacity of the material can be written as

$$C = C_e + C_l + C_{mag} \quad (1.32)$$

The lattice contribution to the specific heat is common to all the materials. It arises due to the thermal vibration of the lattice atoms. If we consider the amplitude of vibration to be small, then the motion of atoms can be considered as a simple harmonic motion. Classically, the simple harmonic oscillator has six degrees of freedom and hence they have an internal energy $3k_B T$. One mole of system contains N particles, so the total energy will be $3Nk_B T$ and hence the heat capacity will be $3R$ (≈ 25 J/mole-K). This is the value described by Dulong and Petit, hence called as Dulong Petit law [17]. It was found that at low temperatures there is reduction in the specific heat value from the $3R$. Plank had shown that the energy of an oscillator of frequency ν must change in discrete steps of $h\nu$. Einstein used the Plank's idea and assumed that the lattice vibrations in the solid are of single frequency that leads to a result which approximately described the observed temperature dependence of the lattice contribution except at low temperatures. Debye improved upon this model by assuming a frequency distribution $g(\nu)$, of the frequency of lattice vibrations given by,

$$g(v) = \begin{cases} \frac{3v^2}{v_D^3} & \text{for } v \leq v_D \\ 0 & \text{for } v > 0 \end{cases} \quad (1.33)$$

In such case the relation between C_l and T can be given by

$$C_l = 9nR \left(\frac{T}{\theta_D} \right)^3 \int_0^x \frac{x^4 e^x dx}{(e^x - 1)^2} \quad \text{where} \quad \theta_D = \frac{h\nu}{k_B} \text{ and } x = \frac{\theta_D}{T} \quad (1.34)$$

here n is the no of atoms in a unit cell. The above expression can be re written as

$$C_l = 9nR \left(\frac{4T^3}{\theta_D^3} \int_0^{\theta_D/T} \frac{x^3 dx}{e^x - 1} - \frac{\theta_D/T}{e^{\theta_D/T} - 1} \right) \quad (1.35)$$

By expanding the above expression one can obtain the following simpler relation for the two limiting cases,

$$C_l = \begin{cases} 3nR \left[1 - \frac{1}{20} \left(\frac{\theta_D}{T} \right)^2 + \dots \right] & T \gg \theta_D \\ \beta T^3 & T < \theta_D/10 \end{cases} \quad (1.36)$$

where

$$\beta = \frac{12}{5} \frac{nR\pi^4}{\theta_D^3} \quad (1.37)$$

The high temperature limit of above equation ($T \gg \theta_D$) leads to the Dulong Petit's law and the low temperature limit leads to a T^3 variation. For intermediate temperatures the Eq. (1.34) has to be solved numerically.

The electronic contribution to the heat capacity arises only due to the free conduction electrons in the system. Their contribution to heat capacity depends upon their interaction within the compound. In we assume the conduction electrons to be totally free then the expression for the electronic heat capacity is given by [17]

$$C_e = \frac{2}{3} \pi^2 k_B^2 V N(E_F) T = \gamma T \quad (1.38)$$

where $N(E_F)$ is the electron density of states at the Fermi level and V is the volume of the material per mole. The term γ is a constant and called the electronic coefficient of specific heat. Substituting for $N(E_F)$ in the above equation, the expression for electronic coefficient is given by

$$\gamma = \frac{4\pi^3 m k^2}{3h^2} \left(\frac{3N Z V^2}{\pi} \right)^{1/3} \quad (1.39)$$

where Z is the number of free electrons per atom. Now if the electrons interact with the magnetic lattice as in the case of the heavy fermion systems, the expression for electron coefficient in terms of effective mass is given by

$$\gamma = \frac{\pi^3 m^* k_B^2}{k_F^2 h^2} \left(\frac{Z}{\Omega} \right) \quad (1.40)$$

where Ω is the unit cell volume and m^* is the effective mass of the system in terms of its original mass. The presence of magnetic interaction in a system also contributes to the specific heat of the solid. It can be shown that below the ordering temperature, the specific heat follow the T^3 relation given by [18,19]

$$C_{AF} \approx B T^3 \exp(-\Delta/T) \quad (1.41)$$

where B denotes the contribution arising from the antiferromagnetic magnons and Δ denotes a gap in the magnon excitation spectrum. This behavior is seen in many antiferromagnetic compounds, a fit to a typical antiferromagnetic compound is shown in Fig 1.8 [20] with the electronic contribution added to it. A similar approximate expression exists for a ferromagnetically ordered state given by

$$C_F \approx A T^{3/2} \exp(-\Delta/T) \quad (1.42)$$

where A represents the contribution from ferromagnetic magnons.

The magnetic entropy becomes a basic tool to guess the degeneracy of the ground state. The magnetic entropy of the system can be calculated from the magnetic contribution to the specific heat using the relation

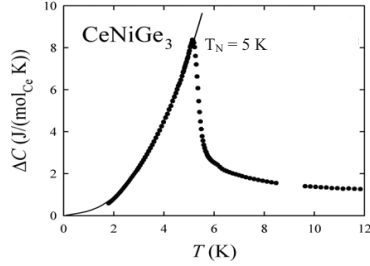


Fig. 1.8: Heat capacity fit in the AF ordered state with electronic term added to it [20].

$$S_{mag}(T) = \int_0^T \left(\frac{C_{mag}}{T} \right) dT \quad (1.43)$$

The magnetic contribution to the specific heat is obtained by separating the lattice and the electronic contribution (non magnetic part) from the total specific heat. The specific heat of the non-magnetic isostructural compound (La, Lu or Y counterpart) can be used as a good non magnetic approximation. Atomic mass renormalization of the specific heat of the nonmagnetic compound

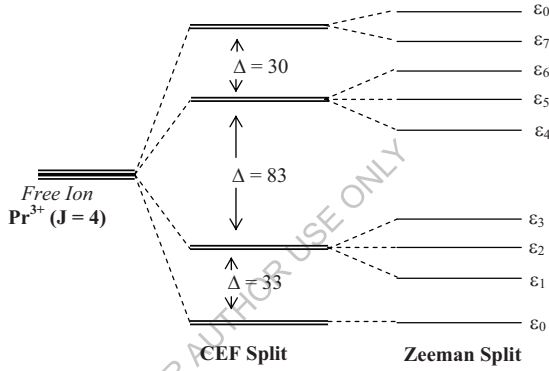


Fig. 1.9: Crystal Field splitting of $J = 4$ ground state of Pr^{3+} ion in PrIn_3 . These levels are further split in the presence of a magnetic field called the Zeeman splitting.

is required to for using it as nonmagnetic contribution. In the worst case if nothing is available (no nonmagnetic sample) then generating a theoretical curve with the Debye expression (Eq. 1.28) and adding the electronic contribution estimated from the low temperature part of the experimental curve is the best solution. In case of the rare earth compounds where only rare earth is magnetic and J is good quantum number, the total entropy obtained should match

$$S_{mag} = R \ln(2J + 1) \quad (1.44)$$

If there is apparent deviation (less than) from this expected value a possibility of crystal field effect can be suggested.

1.6 Crystal Electric Field Effects

In the above sections we discussed the magnetic, thermal and transport properties of the compounds aiming at the interesting behavior of the rare earth ions. These properties are affected by the surrounding environment of the ion. When the atoms are condensed to form a crystal, the electronic state of each ion is modified from the free ion state because of the orbital overlap and the crystal electric field generated by the electrostatic charge on the neighboring ions. In this section we will discuss the effect of CEF on the magnetic, transport and thermal properties of the rare earth compounds.

The rare earth elements include all the elements from La to Lu. Since Y also exhibits the properties similar to that of the rare earth elements, it is often grouped with them. In rare earth atoms, the spatial extent of the $4f$ orbital is smaller than $5d$ and $6s$ (Fig. 1.4), despite the fact that they are more energetic than the later ones [21]. Due to the spatial extent of the $4f$ orbital, about one tenth of the typical lattice spacing [21], and the effective shielding provided by the outer $5d$ and $6s$ orbitals, the $4f$ orbital is less affected by the crystalline environment. It means that the crystal field energy affecting the $4f$ orbital is less compared to the L - S coupling. Hence J is a good quantum number and all the effect of CEF is to split the $2J+1$ fold degenerate states to various sublevels. The splitting of J depends upon the symmetry of the CEF potential. If we consider the case of Pr^{3+} ion in the cubic symmetry, the $J = 4$ state splits into 4 different states as shown in Fig. 1.9 (e.g., PrIn_3 [22]), where as in hexagonal symmetry it splits into 6 levels [23]. Since Pr has even number of electrons, the ground state can be either a nonmagnetic singlet or in a few cases a nonmagnetic doublet [24]. In the case of rare earths having odd number of electrons, Kramers [25] showed that *the electronic levels containing an odd number of electrons must remain at least twofold degenerate, provided that no magnetic field is present.*

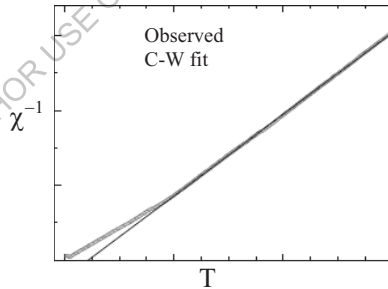


Fig. 1.10: Such a deviation of the χ^{-1} curve from the Curie-Weiss behavior indicates typical Crystal field effects at low temperatures.

There are various methods involved in the crystal field formalism. One of the widely used methods is the *Operator equivalent method*. Here the crystal field Hamiltonian is expressed in terms of the Steven's operator $O_m^l(J)$ by making use of the Wigner-Eckart theorem given by

$$H_{CEF} = \sum_{m,l} B_l^m O_l^m(J) \quad (1.45)$$

where B_l^m are the crystal field parameters. The above Hamiltonian is diagonalized using the standard perturbation techniques in the vector space spanned by the $2J + 1$ eigen functions of the Hamiltonian belonging to the given J . The number of crystalline electric field parameters required for its complete description depends upon the structural symmetry. For cubic, hexagonal and tetragonal structure, the number of parameters is 2, 4 and 5, respectively. The Hamiltonian in the case of a tetragonal structure can be written as

$$H_{CEF} = B_2^0 O_2^0 + B_4^0 O_4^0 + B_4^4 O_4^4 + B_6^0 O_6^0 + B_6^4 O_6^4 \quad (1.46)$$

The numerical value of the parameters in the above equation can be obtained from the neutron diffraction techniques. In many cases the parameters can be obtained by the least squares fit to the magnetic susceptibility or heat capacity. In such cases the values need not be reliable and unique.

1.6.1 Effect on Magnetization

The crystal field effect has the following manifestation on the magnetization behavior of the compound. If the crystal field is effective at high temperatures, then the paramagnetic susceptibility deviates from the straight line behavior at low temperatures. The effective moment obtained in the paramagnetic state will also be much less than that of the expected value. A typical behavior is

shown in Fig. 1.10. In some of the cases, the effect of CEF causes a large deviation in the transition temperature of the compound compared to that expected from the de-Gennes scaling [26].

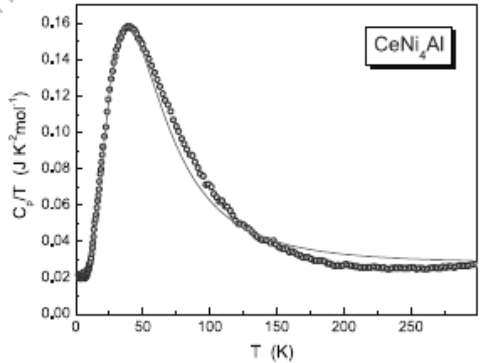


Fig. 1.11: Typical Schottky contribution to heat capacity with the fitted curve. Reported by [27].

1.6.2 Effect on Heat Capacity

The splitting of the ground state J into various sublevels by the CEF modifies the heat capacity of the material. At very low temperatures only the ground state is populated. Now when the heat is supplied, the system absorbs the heat in going from the ground state to the excited states and only a part of the total heat supplied goes in increasing the temperature. The crossover from a state at low temperature to a state at high temperature is a smooth one and manifests itself as a broad peak in the heat capacity known as the *Schottky anomaly*. Considering all the excited states into account the Schottky contribution to heat capacity is given by [17]

$$C_{Sch}(T) = R \left[\frac{\sum_i g_i e^{-E_i/T} \sum_i g_i E_i^2 e^{-E_i/T} - \left[\sum_i g_i E_i e^{-E_i/T} \right]^2}{T^2 \left[\sum_i g_i e^{-E_i/T} \right]^2} \right] \quad (1.47)$$

where R is the gas constant, E_i is the energy level (in units of temperature) and g_i is the degeneracy of the energy level. A typical Schottky curve fitted to above equation is shown in Fig. 1.11. [27].

1.6.3 Effect on Resistivity

At high temperatures, the resistivity is mainly dominated by the phonon contribution. Apart from the phonon contribution a major contribution comes from the disordered spins of a magnetic material in a paramagnetic state. The contribution is called the spin disorder resistivity (SDR) and is independent of temperature [28]. As the temperature is decreased, the phonon contribution decreases and slowly the SDR contribution dominate. If the compound orders magnetically then the spin disorder resistivity vanishes. In the absence of magnetic ordering, the SDR is affected by the CEF. The expression for SDR in the absence of electric field is given by [28]

$$\rho_{SDR} = \left(\frac{3\pi N m}{2\hbar e^2 E_F} \right) G^2 (g_J - 1)^2 J(J+1) \quad (1.48)$$

where m and e are mass and charge of the electron, respectively, N is the no of scattering centers and G is a constant having dimensions of Joule-m^3 . Considering the effect of CEF, the above equation can be written as [29]

$$\rho_{CEF} = \rho_{SDR} \frac{2}{J(J+1)} \sum_{\substack{i,i' \\ m_s, m'_s}} \langle m'_s, i' | S J | m_s, i \rangle^2 p_i f_{i'} \quad (1.49)$$

where ρ_{SDR} is the spin disorder resistivity in the absence of CEF and is given by (1.48), m_s and m'_s represent the spins of the conduction electrons in the initial and the final states and i and i' represent the crystal field states with corresponding energies E_i and $E_{i'}$. p_i is the probability of

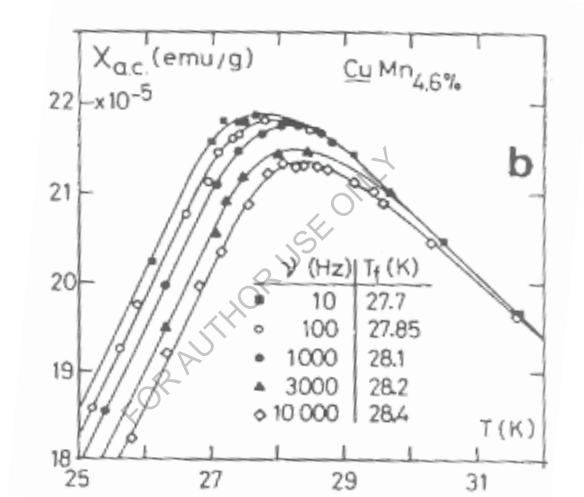


Fig. 1.12: Peak shift with frequency for a typical Cu-Mn spin glass. Reported by [30]

the rare earth ion being in a certain crystal field state i with energy E_i and is given by

$$p_i = \frac{\exp(-E_i/kT)}{\sum_j \exp(-E_j/kT)} \quad (1.50)$$

and the distribution function $f_{i'}$ is given by

$$f_{i'} = \frac{2}{1 + \exp(-E_{i'}/kT)} \quad (1.51)$$

1.7 Spin Glass Behavior

For the materials exhibiting Kondo effect it was observed that the compound contains a trace amount of magnetic impurity. Now when the impurity is increased to above a few percentage, the impurity spins start to interact with each other. Since the spins are less and are well separated from each other there is a random interaction taking place among them mediated via conduction electrons (*RKKY*) and the behavior exhibited by them is known as the Spin Glass behavior. Since the impurity ion replaces the host atoms from the random lattice sites, the net exchange field at any impurity site due to the remaining impurity spin will vary from site to site. This causes the spins to freeze in random direction below a certain temperature. The frozen state is called the *Spin Glass* state and the underlying alloy system is called the Spin Glass system.

The basic characteristic of the spin glass system is as follows. The DC susceptibility shows a difference below the freezing temperature in the field cooled (FC) and zero field cooled (ZFC) conditions. A similar behavior also exists in the case of anisotropic ferromagnets, but in spin glass systems the separation of the susceptibility under FC and ZFC condition takes place after the peak. At high temperatures, the spins are independent and a Curie-Weiss behavior is observed. A confirmatory

test for the spin glass behavior is a peak shift in the AC susceptibility. The peak in the AC susceptibility at freezing temperature shifts towards high temperature with increasing frequency of the AC field. A peak shift with frequency for a typical spin glass (Cu-Mn) [30] is shown in Fig. 1.12. A similar behavior also exists with the super paramagnetic compounds. To differentiate between these two behaviors, the peak shift with frequency is fitted to a law known as the Vogel-Fulcher law, given by

$$\omega = \omega_0 e^{\left(\frac{-E}{k_B(T_f - T_0)} \right)} \quad (1.52)$$

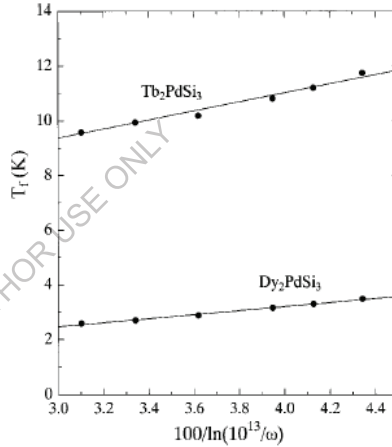


Fig. 1.13: The peak shift with frequency for spin glass systems fitted to Vogel-Fulcher law [33].

where $\omega_0 = 1/\tau_0$ and τ_0 is the relaxation time of the spins within the system. T_0 is called the Vogel Fulcher temperature and depends upon the interaction between the spins within the system [31]. E is the activation energy which depends on the potential barrier within the system and T_f is the freezing temperature. In a spin glass system, the spins are frozen and hence require much more relaxation time compared to a super paramagnet [32]. Hence a fit to above equation gives a ω_0 of the order of 10^8 to 10^{13} where as the values are unphysical (of the order of 10^{30}) for a super paramagnet. High value of T_0 (close to T_f) indicating more interaction between the spins also supports the spin glass behavior of the system. A fit to the Vogel Fulcher law for typical spin glass compounds, Tb_2PdSi_3 and Dy_2PdSi_3 [33] is shown in Fig. 1.13. The values obtained are $\omega_0 = 10^{13}$ Hz, $E_a = 165$ K and $T_a = 4.42$ K and $\omega_0 = 10^{13}$ Hz, $E_a = 75$ K and $T_a = 40.3$ K, respectively.

References

1. Charls Kittel, *Introduction to Solid State Physics* (John Wiley & Sons).
2. J.H. Van-Vleck, in *Theory of Electric and Magnetic Susceptibility* (Oxford University Press, London, 1931).
3. H.C. Hamakar, L.D. Wolf, H.B. Mackey, Z. Fisk and M.B. Maple, *Solid State Comm.*, **32** (1979) 289.
4. Nicola A. Spladin, *Magnetic Materials, Fundamental and device applications* (Cambridge University Press).
5. A.J. Freeman, in *Magnetic Properties of Rare Earth Metals*, edited by R.J. Elliot, 1972.
6. M.A. Ruderman and C. Kittel, *Phys. Rev.* **96** (1954) 99; T. Kasuya, *Prog. Theor. Phys. (Kyoto)* **16**, (1956) 45; K. Yoshida, *Phys. Rev.* **106** (1957) 893.
7. P.G. de Gennes, *J. Physique Radium* **23**, 510 (1962).
8. N.F. Mott and H. Jones, *The Theory of the Properties of Metals and Alloys* (Oxford University Press, London, 1958).
9. P.S. Salamakha, O.L. Sologub, C. Rizzolic, J.R. Hesterd, J. Stepien-Damme, A.P. Goncalvesa, E.B. Lopesa and M. Almeidaa, *Intermetallics*, **12** (2004) 1325.

10. M.B. Fontes, J.C. Troches, B. Giordanengo, S.L. Bud'ko, D.R. Sanches and E.M. Baggio-Saitovitch, *Phys. Rev. B* **60** (1999) 6781 and references their in.
11. J. Mathon, *Proc. R. Soc. London, Ser. A* **203** (1968) 355.
12. H. Yamada and S. Takada, *Prog. Theor. Phys.* **49**, (1973) 1401.
13. Y. Dalichaouch, M.C. Andrade and M.B. Mapple, *Phys. Rev. B.* (46) (1992) 8771.
14. J. Kondo, *Progr. Theo. Phys.* **32**, (1964) 37.
15. V.T. Rajan, *Phys. Rev. Lett.* **51** (1983) 803.
16. N. Andrei and J.H. Lowenstein, *Phys. Rev. Lett.* **46** (1981) 356.
17. E.S.R Gopal, *Specific Heat at Low Temperatures*, International cryogenics micrograph series, (Plenum Press, New York, 1966).
18. O.V. Lounasmaa and L.J. Sundstrom, *Phys. Rev.* **150**, (1966) 399.
19. N. Andri, K. Furuya and J.H. Lowenstein, *Rev. Mod. Phys.* **55** (1983) 331.
20. A.P. Pikul, D. Kaczorowski, T. Plackowski, A. Czopnik, H. Michor, E. Bauer, G. Hilscher, P. Rogl and Yu. Grin, *Phys. Rev. B* **67** (1999) 224417.
21. A.R. Macintosh and H.B. Moller, *Magnetic properties of rare earth Metals*, edited by R J Elliot (Plenum Press, London and NewYork, 1972).
22. A.M. Van-Diepan, R.S. Craig and W.E. Wallace, *J. Phys. Chem. Solids* **32** (1971) 1867.
23. J. Mrachkov and E. Leyarovski, *Physica B*, **150** (1988) 404.
24. J. Mrachkov and E. Leyarovski, *Physica B*, **154** (1988) 66.
25. H.A. Kramers, *Proc. Acad. Sci. Amsterdam*, **33** (1930) 953.
26. D.R. Noakes and G.K. Shenoy, *Phy. Lett.* **91** (1982) 35.
27. T. Tolinski, A. Szewczyk, M. Gutowska and A. Kowalczyk, *Phy. Stat Sol. B*, **242** (2005) R40.
28. A.J. Dekker, *J Appl. Phys.* **36** (1965) 906.
29. U.V.S. Rao and W.E. Wallace, *Phys. Rev. B*, **2** (1970) 4613.
30. J.L. Tholence, *Solid State Comm.*, **35** (1980) 13.
31. S. Strickman and E.P. Wohlfarth, *Phys. Lett.* **85A** (1981) 467.
32. C.Y. Huang, *J. Mag. Mag. Mater.*, **51** (1985) 1.
33. D.X. Li, S. Nimori, Y. Shiokawa, Y. Haga, E. Yamamoto and Y. Onuki, *Phys. Rev. B*, **68** (2003) 012413.

Chapter 2

Experimental Methods

In this chapter we will be discussing briefly the experimental methods used for preparation of samples and their characterizations at various temperatures and fields.

2.1 Sample Preparation

All the samples investigated in this thesis were prepared by the arc melting procedure followed by annealing at the required temperatures. The arc melting setup consists of a vacuum system and a sample chamber. The vacuum system comprises of a rotary and diffusion pump for evacuating the sample chamber. The sample chamber consists of a water cooled hearth made of oxygen-free-high-conductivity copper and a copper electrode with thoriated tungsten tip. The copper hearth and the tungsten tip act as the electrodes where the high current is applied from a current source. The samples are melted in argon atmosphere to minimize oxidation. The arc strikes when the tungsten tip touches the copper hearth because of the high current flowing through the tip (100 to 400 A). First the arc is moved to melt a titanium getter to remove traces of oxygen, if present, in the argon. Then the arc is slowly moved to the samples to be melted. The arc furnace used is a commercially available one supplied by *Vacuum Techniques* (Bangalore). The melted ingots were wrapped in tantalum foil and sealed in evacuated quartz tube for annealing. The tantalum foil is required to prevent the sample from reacting with the quartz tube.

2.2 Phase Detection (X-ray Diffraction)

To investigate the phase purity and crystallographic parameters of the sample, powder X-

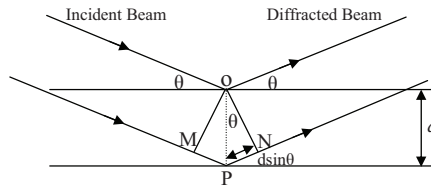


Fig. 2.1: Diffraction of X-ray by a set of parallel atomic planes separated by a distance d .

ray diffraction patterns of all the investigated samples were taken on a commercial X-ray diffractometer (Panalytical). The principal of X-ray diffraction is as follows.

When an X-ray beam is incident on a set of parallel planes separated by a distance d as shown in Fig. 2.1, the reflected beam from any two adjacent planes will have a path difference of $2d \sin \theta$, where θ is the angle between the planes and the incident beam. The beam reflected from the two different planes will form a constructive interference if the path difference between them follows the Bragg's law [1] relation

$$2d \sin \theta = n\lambda \quad (2.1)$$

where n is an integer called the order of reflection and λ is the wavelength of the X-ray used. Depending upon the wavelength of the X-ray used and the distance between the planes, the rays reflected from various planes will constructively interfere to give a diffraction pattern [2]. The diffracted radiation is measured as a function of angular position of the detector.

The wavelength of the incident X-ray used is 1.541 Å of Cu- K_α . The other radiation Cu- K_β , which also gets incident with Cu- K_α , is filtered by Ni filter. Before the rays are incident on the sample they are passed through a soller slit, in order to collimate the radiation. After diffraction from the sample, X-ray beam passes through antiscatter slit and a soller slit before it finally reaches to the detector. The powder sample which is exposed to X-ray should be well powdered (particles as small as possible) so that all possible orientations of the crystallites are equally exposed to the X-ray.

To check for the homogeneity of the compound formed and to obtain the lattice parameters, a Reitveld analysis of the obtained X-ray pattern is to be carried out [3]. A FullProf program was used for this purpose. The program requires an input file containing the following information; (i) a correct space group of the compound to be analyzed, ii) crystallographic (x, y, z) positions of each constituent atom in the unit cell with proper occupancy, iii) a rough estimate of the lattice parameters of the compound and iv) wavelengths (K_α and K_β) of the X-rays used along with the 2θ range of scanning. The program automatically takes care of the other parameters like background coefficients, asymmetry, scale factor, strain parameters, etc. The program theoretically generates a curve optimizing all these parameters to fit the observed X-ray pattern. The quality of the fit is judged by the χ^2 value and the goodness of the fit value.

2.3 Resistivity Measurements

Resistivity measurements of some of the investigated samples were performed over the temperature range of 2–300 K using a standard four probe method. In the four probe method, two

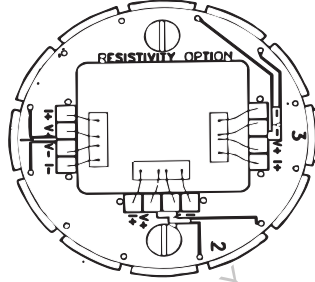


Fig. 2.2: Top view of the resistivity puck with three samples mounted for resistivity measurement.

outer probes are used to supply the current and the inner two to measure the voltage. Since the voltage is measured by a high resistance voltmeter, ideally without drawing any current; this procedure takes care of the contact resistance involved. The resistivity measurement was done in a PPMS (Physical Property Measurement System) (Quantum Design, USA). In a PPMS, the resistivity measurement requires the samples to be loaded on a puck. A typical resistivity puck is shown in Fig. 2.2. The samples are positioned near the centre of the puck as shown. All the connecting wires are first soldered to the gold plated puck contacts. After that each wire is stuck to the sample using a silver paste. After the silver paste dries up, the puck is inserted into the User Bridge for contact resistance measurement. In the case of intermetallic samples (metallic behavior), the contact resistance should come out to be less than $1\ \Omega$. This makes the puck ready for inserting into the system. In a PPMS system, the puck sits on a platform in a variable temperature insert (VTI) where it makes electrical contacts with the system. The VTI can provide temperature variations between 1.8 K–350 K. A superconducting magnet provides magnetic fields in the range of 0 to ± 90 kOe.

The resistance of the sample was measured by an AC drive mode, in which a DC current is passed through the sample in one direction and the voltage drop is measured. After that, the procedure is repeated by reversing the direction of the current and the final resistivity is calculated

by averaging the absolute value of both the readings. This procedure is helpful to avoid the thermo *emf* generated in the sample due to the thermal gradients. But in some of the cases where the samples are electrically directional dependent, the above procedure is followed by passing the current only in one direction, called the DC mode. The resistivity of the sample is then calculated using the formula

$$\rho = R \frac{A}{l} \quad (2.2)$$

where R is the measured resistance, A is the cross-sectional area of the sample and l is the distance between the two voltage leads.

2.4 Magnetization Measurements

Magnetization measurements of all the investigated samples were done on different magnetometers depending upon the requirement and availability. Magnetization measurements were carried out either in a SQUID (Quantum Design, USA) magnetometer or in a VSM (Quantum Design, USA or Oxford Instruments, UK).

VSM (Vibrating Sample Magnetometer)

The Vibrating Sample Magnetometer [3] is based on the principle of magnetic induction, whereby a changing magnetic flux induces an *emf* in a coil. The time dependent induced voltage is given by

$$V_{coil} = \frac{d\Phi}{dt} = \left(\frac{d\Phi}{dz} \right) \left(\frac{dz}{dt} \right) \quad (2.3)$$

where Φ is the magnetic flux enclosed by the coil, z is the movement of the magnet causing the flux change and t is the time. For sinusoidal oscillating magnet the voltage is given by

$$V_{coil} = 2\pi f C m A \sin(2\pi f t) \quad (2.4)$$

where C is the coupling constant, m is the moment of the magnet, A and f are the amplitude and frequency of the oscillation, respectively. In a VSM the magnetization of the sample is determined by measuring the coefficient of the sinusoidal voltage response from the coil. The process with the experimental setup is as follows.

Figure 2.3 shows a schematic diagram of Quantum Design VSM. The VSM head, sample rod, pickup coils and magnet are the part of the VSM system where as the block diagram explains

its working in brief. The VSM requires the sample to be loaded on the sample holder, which is further fixed to the sample rod and inserted into the VSM. The top of the sample rod sits on the armature of a linear motor, which vibrates the rod. Then the sample is centered in the VSM pick up coil such that it is at the centre of the two pick up coils. The precise amplitude and frequency of oscillation of the sample is controlled by a servo control mechanism using a read back encoder

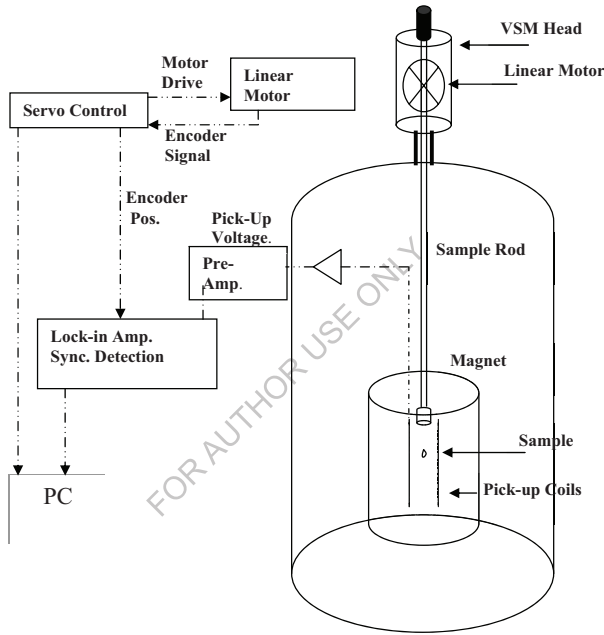


Fig. 2.3 Schematic diagram of VSM

signal from the linear motor. The oscillating sample induces emf in the two reference coils. The voltage induced in both the pickup coils is fed to the lock-in amplifier. The magnetization of the sample is proportional to the difference between the voltages from the two coils. The output voltages also depend upon the amplitude and the frequency of the vibration and to get rid of it, the signal is fed to a lock-in amplifier. The lock-in amplifier uses the position encoder signal as a reference for the synchronous detection. This signal is obtained from the servo control system,

which interprets the encoder signal from the VSM linear motor. The VSM detection module detects the in-phase and the quadrature phase signal from the encoder and from the amplified voltage from the pickup coils. These signals are averaged and sent to the VSM application, running on a PC. The calibration of the system is done using a high purity Pd standard. The system design is appropriate for the systems which require or are independent of the vibration and field parallel to each other.

2.4.1 SQUID (Superconducting Quantum Interference Device)

A commercial RF SQUID magnetometer (Quantum Design, USA) was used for the DC magnetic susceptibility and isothermal magnetization measurements of some of the investigated samples with a temperature range of 2 to 300 K and a maximum field of ± 70 kOe.

A SQUID magnetometer measures the magnetic moment of the sample using a superconducting quantum interference sensor. The principle of this sensor is based on the phenomena of

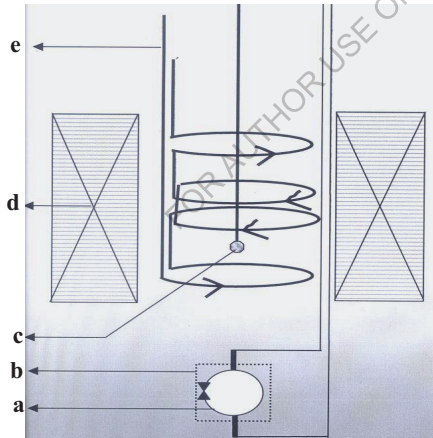


Fig. 2.4: A simplified view of a SQUID magnetometer ; **a.** RF SQUID sensor, **b.** magnetic shield, **c.** sample, **d.** superconducting magnet, **e.** second derivative coil.

quantum interference [4] occurring in the tunneling superconducting (SC) current across a Josephson junction [5]. The operating principle of the magnetometer is as follows. In this system the SQUID sensor is the part of a RF resonance circuit. The circuit is kept at equilibrium with a

certain RF bias current. When a change in the magnetic flux is sensed, it disturbs the equilibrium. A feed back RF current is introduced in the circuit to bring the circuit back into equilibrium state. The magnitude of this feed back current is proportional to the magnetic moment which brought about the change in the magnetic flux.

A schematic diagram of a magnetometer employing a RF squid sensor is shown in Fig. 2.4. It consists of a superconducting (SC) magnet, highly balanced second derivative gradient coil (about 3 cm in length) located at the centre of the magnet and RF SQUID sensor. The superconducting magnet is used to generate large magnetic fields up to 70 kOe. The second derivative gradient coil is superimposed on the DC magnetic field at which the measurement is being made. This is used to cancel the effect of any small change in the uniform field that occurs due to some external agency. The linear motion of the sensor through this detection coil induces an electric current in the coil and this current is fed to the RF SQUID sensor by the superconducting isolation transformer (not shown). The RF sensor is highly affected by the magnetic field, so is kept 11 cm below the SC magnet and is shielded from the stray fields using a Nb superconducting shield. The isolation transformer is used to isolate the SQUID sensor from the detection coils. There is a heater present on the SC transformer which heats the transformer to the normal state in order to eliminate the persistent current generated in the detection coils, when the magnetic field is changed during the measurements.

The sample to be studied is wrapped in a tissue and is pushed in a straw. The mass of the sample is decided by the moment expected from the sample. The straw is then attached with a standard nonmagnetic sample rod and inserted in the coils. The sample is first positioned well below the pickup loop and the signal corresponding to the sample position is measured. The sample is then raised in discrete steps through the coil array by use of a computer controlled stepper motor. At each step, the sample is stopped and the measurement is made. The detected signal at each step corresponds to the magnetic moment of

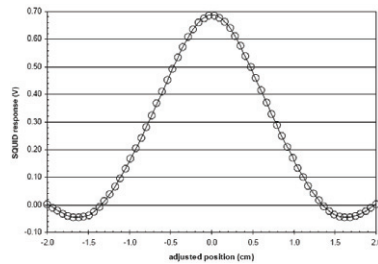


Fig. 2.5: The circles represent the SQUID voltage produced during the scan and the line represents the fit to it.

the sample. These measurements are taken at certain number of steps across the pickup coils. Thus, the moment obtained would follow the gradient function of the coil as shown in Fig. 2.5. The observed set of data points are fitted to the gradient function of the coil and a single accurate value of the magnetic moment of the sample is obtained (the value corresponding to the central peak of the curve). The minimum moment that can be detected by SQUID is of the order of 10^{-7} emu and the maximum limit is 3 emu.

2.4.2 AC Susceptibility Measurement

The AC susceptibility of some of the investigated samples was measured in a commercially available AC susceptometer. The method is employed to study the spin dynamics of the magnetic materials. The description of its working is as follows.

The heart of the AC susceptibility system is a coil which consists of two separate identical secondary coils wound on a nonmagnetic bobbin. A primary coil is wound uniformly on the secondary coils. The current to produce an AC field (~ 1 to 5 Oe) is passed through the primary coil. When there is no sample, any AC current passed through the primary coil will ideally produce a null signal, since both the secondary coils have equal turns. In practice, a small signal appears across the secondary terminals, referred to as the background signal. The two terminals of the secondary coils are connected to the differential input of a lock-in amplifier which is adjusted to take care of the background signal. Now when the sample is placed inside one of the secondary coils, the AC field created by the primary induces a varying magnetic moment on the sample which in turn induces a proportional signal across the secondary. The true signal produced by the sample is obtained by subtracting the background signal. The sample signal consists of a signal of reference frequency (frequency of the AC field) along with other noise frequencies. The lock-in amplifier detects the reference signal frequency by phase sensitive method rejecting the other noise frequencies. The in-phase signal detected by the lock-in amplifier is proportional to the real part of the susceptibility and the out of phase signal is proportional to the imaginary part of the susceptibility. The reference frequency is generally selected to be an odd value (133, 1333, etc.) to avoid the noise produced from the even harmonics of the AC mains (50 Hz).

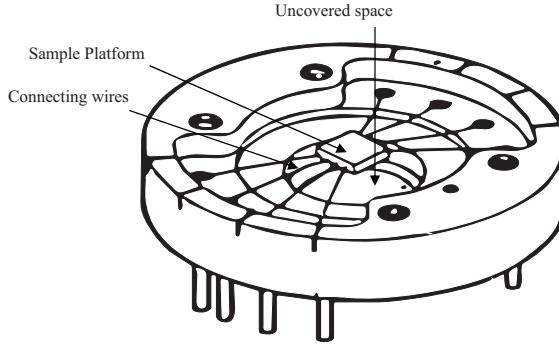


Fig. 2.6: Schematic diagram of a heat capacity puck

2.5 Heat Capacity

Heat capacity of a sample is an essential tool to investigate the thermal and magnetic properties of the sample. It also plays a very important role in understanding the behavior of the conduction electrons at low temperature. The heat capacity of all the investigated samples was measured using the *relaxation method* in a heat capacity attachment of PPMS (Quantum Design, USA). The relaxation method requires the sample to be isolated from the surrounding atmosphere, hence it has to be put up in a high vacuum and on a platform with minimal contacts to the surrounding atmosphere.

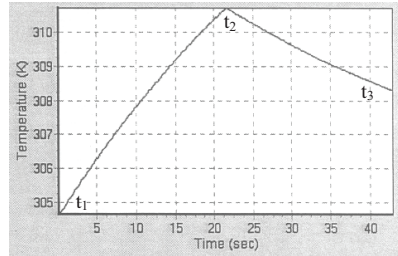


Fig. 2.7: Temperature vs time plot for platform temperature during a cycle of measurement.

The experimentally measured heat capacity of the material is the heat capacity at constant pressure (C_p). The measurement requires the sample to be mounted on a sample platform in a heat capacity puck as shown in Fig. 2.6. The sample platform is a $\sim 2 \times 2$ mm surface hanging on eight thin delicate connecting wires with the puck as required for the relaxation method discussed

above. The sample should be cut in such a way that it sits within the platform and has a mass within 20 mg (less mass reduces the measuring time). The lower surface of the sample is required to be smooth to ensure better contact with the platform. While loading the sample, the puck is placed on a holder which supports and holds the sample platform through vacuum. The sample is then put on the grease applied to the platform, to ensure better contact. The heat capacity of the grease is measured before as addenda for subtraction. The measurement process is as follows.

The bottom of the sample platform contains a heater and a thermometer which are electrically connected by the connecting wires. These wires also provide the thermal connection between the platform and the puck and also support the platform. A high vacuum (using a cryopump) is maintained within and surrounding the puck. This ensures that the thermal conductance between the platform and puck is dominated by the connecting wires. This helps in accounting for the heat supplied and gained during the thermal cycle. During the measurement, a known amount of heat pulse is applied for a fixed time. The sample from its initial temperature t_1 rises to some other temperature t_2 as shown in Fig. 2.7. Then it is allowed to relax for the same time interval (time taken for the temperature to rise to maximum) by which the sample cools to a temperature t_3 . After each such thermal cycle, the temperature response of the sample platform (with sample) is fitted to a model called *Two-Tau model*, which accounts for both the thermal relaxation of the sample platform to the puck temperature and the relaxation between the sample platform and the sample itself. The fitting gives the heat capacity value of the sample platform (including sample). The sample heat capacity is obtained by subtracting the addenda measurement, which also involves the same procedure but the platform response is fitted to One-Tau model.

2.6 References

1. C. Kittel, *Introduction to Solid State Physics* (John Wiley & Sons).
2. C. Suryanarayana and M.G. Norton, *X-ray Diffraction, A Practical approach* (Plenum Press).
3. Foner and Simon, *Versatile and Sensitive Vibrating Magnetometer*, *Rev. Sci. Instr.*, **30** (1959) 548.
4. J.C. Jaklevic, J. Lambe, A.H. Silver and J.E. Mercereau, *Phys. Rev. Lett.*, **12** (1964) 159.
5. B.D. Josephson, *Phys. Rev. Lett.* **7** (1962) 251.

Chapter 3

Magnetic Properties of Ternary Indides $R_2\text{CoIn}_8$ (R = rare earths & Y)

3.1 Introduction

Ternary indides involving rare earth elements form a large family of compounds. These compounds exhibit a variety of interesting physical properties such as heavy fermion, superconductivity, pressure induced superconductivity, Kondo behavior, valence fluctuation, various types of magnetic orderings, metamagnetic transitions, crystal field effects, etc. Most of these properties arise mainly due to the presence of the rare earth ions. This gives us an opportunity to explore the behavior of $4f$ electrons for fundamental studies and its possible applications.

Various physical properties arise in intermetallic compounds containing rare earth and transition metals because of the interplay between $4f$ and $3d$ orbitals. The $4f$ orbital lies deep inside the atom and hence is not much affected by the orbital overlap when rare earths form compounds. However, for Ce and Yb compounds, the $4f$ orbital is not completely isolated within the atom but gets hybridized with the conduction band. In technical terms, the f electron is said to be embedded in the Fermi sea of conduction electrons or the $4f$ energy levels are found in the vicinity of the Fermi energy. This gives rise to interesting properties like heavy fermion behavior, valence fluctuation, Fermi liquid behavior, etc. Since Yb belongs to the heavy rare earth group, these properties are less significant compared to the Ce compounds. These compounds are characterized by a temperature T^* (Kondo lattice temperature), above which the $4f$ moments are coupled weakly with the conduction electrons and hence the compound exhibits usual metallic behavior. As the temperature is lowered below T^* , the coupling becomes increasingly strong, giving rise to various interesting physical phenomena. To give a qualitative explanation of the origin of the above mentioned interesting properties, we define the coupling between the local $4f$ spin and the conduction electron spin by a coupling constant, $g = N_F |J|$ where $J < 0$ and N_F is the density of states at the Fermi level. For $g \ll 1$, the coupling is weak and the magnetic ordering of the $4f$ electrons takes place via RKKY interaction (e.g., Gd metal). For $g < 1$, there can be a coexistence of the heavy fermion state with a local moment magnetic ordering as found

in CeAl_2 ($T_N/T^* > 1$, T_N is the Neel Temperature) and a non Fermi liquid type behavior at low temperatures [1]. As $g \rightarrow 1$, the compounds show properties like band magnet and coexistence between superconductivity and heavy fermion behavior as in the case of CeCu_2Si_2 ($T_N/T^* < 1$) [2]. For $g > 1$, properties like valence fluctuation (CePd_3) and Kondo insulator ($\text{Ce}_3\text{Pt}_3\text{Bi}_4$) behaviour arise [3,4].

$R_2\text{CoIn}_8$ series of compounds belong to a family of compounds represented by the general formula $R_n M \text{In}_{3n+2}$ (R = rare earths, M = Co, Rh and Ir, $n = 1$ and 2) [5,6,7]. The crystal structure of $R_n M \text{In}_{3n+2}$ can be seen as n layers of $R\text{In}_3$ stacked sequentially along the c axis with an intervening single layer of $M\text{In}_2$. They crystallographic studies on these compounds [5,6] suggested that the compounds form for almost all the rare earths except for La, Eu and Yb. Since Ce being the interesting candidate among the entire rare earths, various studies have been reported on the Ce compounds in both the above series with various transition elements using single crystals. Some of the interesting properties exhibited by the Ce compounds are as follows. For transition metal $M = \text{Rh}$, both the $n = 1$ and $n = 2$ compounds, CeRhIn_5 and Ce_2RhIn_8 , are antiferromagnets with Neel temperatures $T_N = 3.8$ K and 2.8 K, respectively [8,9]. The electronic specific heat coefficient γ is estimated to be ≈ 50 mJ/K²mol-Ce for CeRhIn_5 and ≈ 370 mJ/K²mol-Ce for Ce_2RhIn_8 [10,11]. The low value of γ found in the former compound indicates a moderate type heavy fermion behavior, where as the latter one shows a pure heavy fermion behavior. The ground state of CeRhIn_5 and Ce_2RhIn_8 transforms from antiferromagnetic state to superconducting state at 2 K under a pressure of 1.6 and 3.8 GPa [8,12], respectively. For $M = \text{Ir}$, both CeIrIn_5 and Ce_2IrIn_8 show heavy fermion behavior with γ values of about 700 mJ/K²mol-Ce [9,13]. CeIrIn_5 is a superconductor with a transition temperature of $T_c = 0.4$ K at ambient pressure and Ce_2IrIn_8 is paramagnetic down to 50 mK with no evidence of any phase transition. For $M = \text{Co}$, CeCoIn_5 is a heavy fermion superconductor with a transition temperature of $T_c = 2.3$ K [14]. The γ value is ≈ 300 mJ/K²mol-Ce at T_c . Ce_2CoIn_8 is also a heavy fermion superconductor with a transition temperature $T_c = 0.4$ K and $\gamma = 500$ mJ/K²mol-Ce [15]. Considering such interesting properties in Ce compounds and to the best of our knowledge there were no reports on compounds with other rare earths, we decided to study the same compounds with other rare earths. To start with, we selected the $R_2\text{CoIn}_8$ series of compounds and studied their physical properties with magnetization, specific heat and resistivity measurements. The rare earth elements include R

= Ce, Pr, Sm, Gd, Tb, Dy, Ho and Y. This chapter deals with the structural, magnetic, thermodynamic and transport properties of the $R_2\text{CoIn}_8$ series of ternary indides.

3.2 Sample Preparation and Crystal Structure

Starting materials used for the preparation of $R_2\text{CoIn}_8$ series of compounds were the high purity metals R ($\approx 99.95\%$), Co (99.9%) and In (99.99%) from Alfa Aesar, U.K. The rare earth metals are highly susceptible to oxidation and hence the oxidized layers need to be removed before melting. Stoichiometric amounts of metals were melted in an Arc furnace on a water cooled cooper hearth under a titanium gettered argon atmosphere. The button was flipped over and re-melted, repeating the process at least 3 times to ensure homogeneity of the compounds formed. An extra 5% Indium (of the total Indium weight) was added to compensate for the loss of Indium (due to vaporization) during melting. The buttons were then wrapped in tantalum foil, sealed in evacuated quartz tube and annealed for one month at 600°C and cooled slowly to room temperature. The powder X-ray diffraction patterns of all the samples were taken on a Siemens X-ray diffractometer at room temperature, using $\text{Cu-K}\alpha$ radiation and pure Si as an internal standard. In order to know the origin of the structure and its stability, X-ray patterns before and after the annealing of the samples were compared. It was found that the as-melted samples do not form in a single phase (Fig. 3.1a) and the phase forms only after annealing (Fig. 3.1b). Some of the diffraction lines of the as melted samples could be indexed to $R\text{In}_3$, $M\text{In}_2$ and In phases. This shows that the annealing causes the inter diffusion of various phases to form $R_2\text{CoIn}_8$ phase. Our experiments to improve the homogeneity of the compounds by annealing at higher temperatures (750°C) failed. The compound decomposed back into $R\text{In}_3$ phase along with other impurity phases.

A small amount of Indium impurity was found in some of the compounds (as shown by arrow in Fig. 3.1b). Since In does not have any magnetic properties, its presence is neglected in the discussion of the magnetic properties of the compounds. Er_2CoIn_8 could not be formed by this technique, three of our trials failed. Report on this series of compounds [5] states that the Er compound forms only with $R_2\text{CoIn}_8$ phase and not with $R\text{CoIn}_5$ phase. One of the possible reasons is that, since both the series of compounds ($R_2\text{CoIn}_8$ and $R\text{CoIn}_5$) have the same 'origin', Er_2CoIn_8 might be on the border of crystallographic stability. La based compound is not formed in any of the series. The possible reason might be attributed to the larger size of the La

atom.

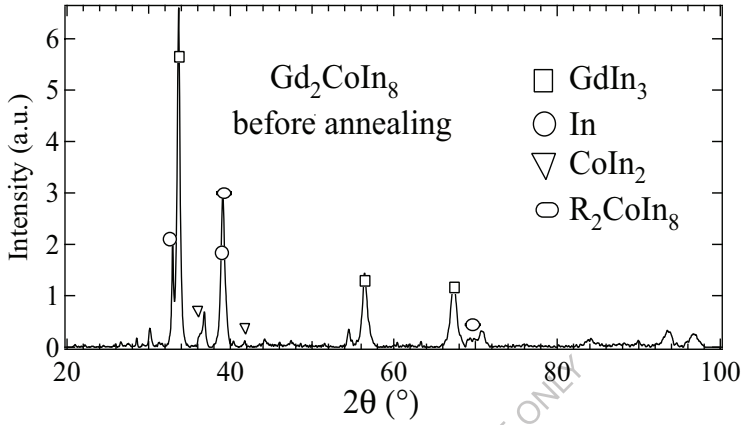


Fig. 3.1a: Room Temperature X-ray diffraction pattern for Gd_2CoIn_8 before annealing.

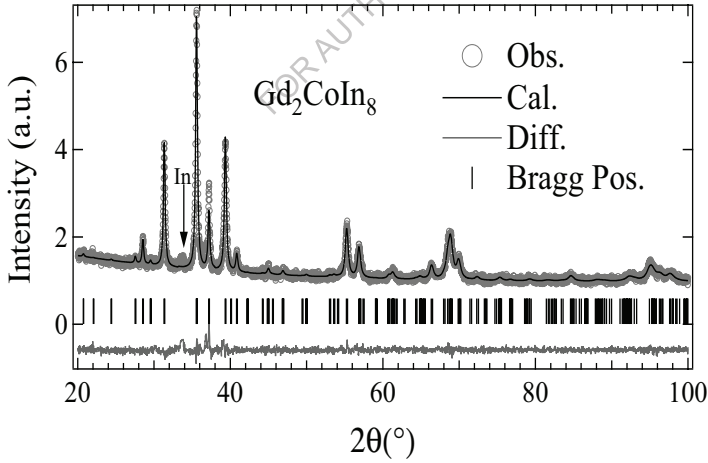


Fig. 3.1b: The Rietveld analysis of the observed diffraction pattern of Gd_2CoIn_8 after the annealing. The vertical bars indicate Bragg position. The arrow indicates an In peak.

$R_2\text{CoIn}_8$ series of compounds form in a Ho_2CoGa_8 type tetragonal structure with a space group $P4/mmm$. In order to confirm the phase homogeneity and to calculate the lattice and crystallographic parameters of the compounds, Rietveld analysis of the X-ray pattern of all the compounds was carried out using FullProf program. The Lattice parameters thus obtained are pre-

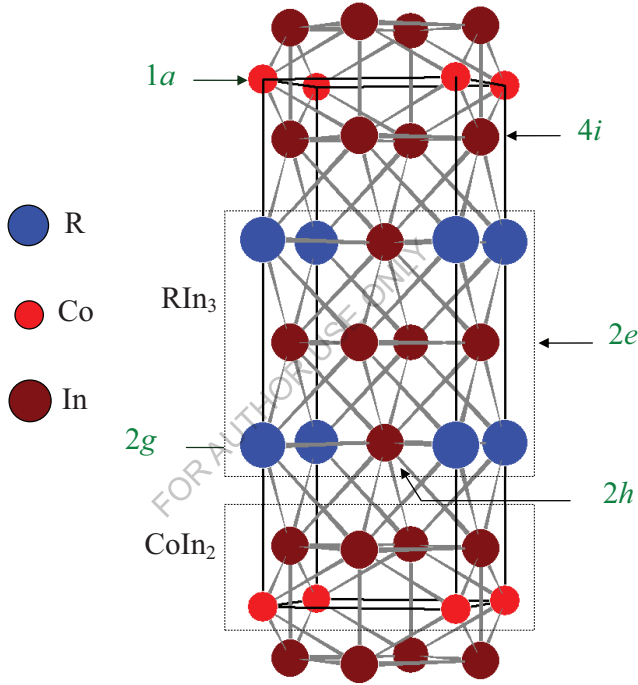


Fig. 3.2: Crystal Structure of $R_2\text{CoIn}_8$ compound. Atoms connected by solid lines represent a unit cell.

sented in Table 3.1 and the refined X-ray pattern for a typical compound, Gd_2CoIn_8 , is shown in Fig. 3.1b. The crystallographic parameters for each of the constituent atom (at various crystallographic sites) in Gd_2CoIn_8 are presented in Table 3.2. Site symmetry is expected to remain the

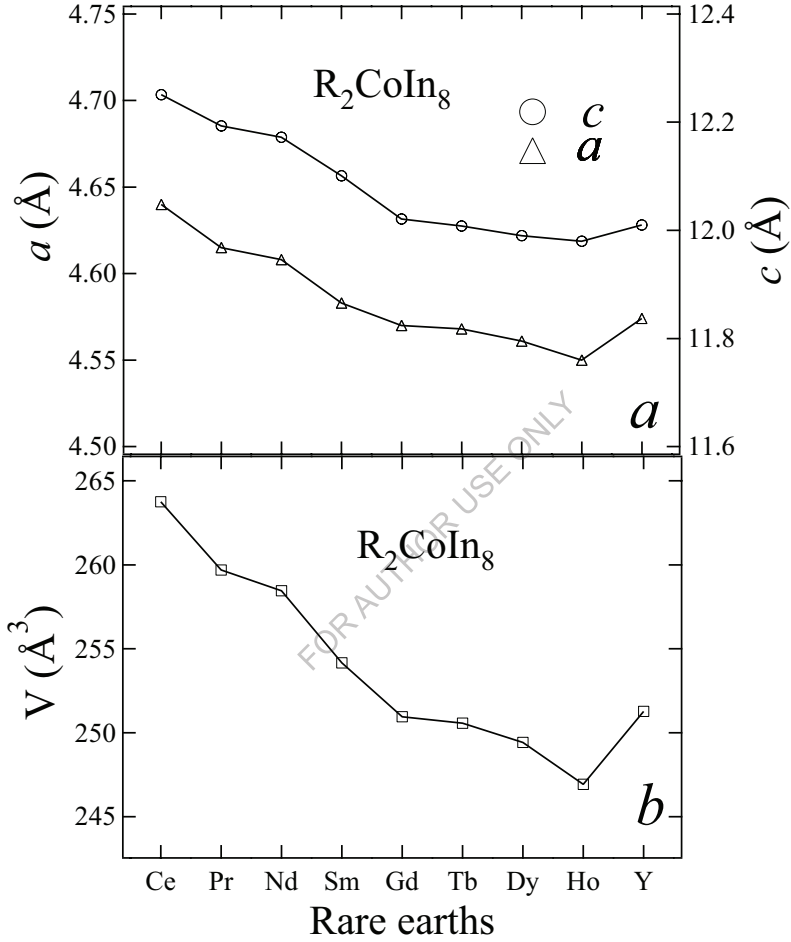


Fig. 3.3: (a): variation of lattice parameters of $R_2\text{CoIn}_8$ series of compounds with rare earths. (b): variation of unit cell volume for the same with rare earths

Table 3.1 : Lattice parameters, unit cell volume and the c/a ratio for $R_2\text{CoIn}_8$ series of compounds.

| Compound | a (Å) | c (Å) | V (Å ³) | c/a |
|-----------------------------------|---------|---------|-----------------------|---------|
| Ce ₂ CoIn ₈ | 4.64 | 12.251 | 263.759 | 2.6403 |
| Pr ₂ CoIn ₈ | 4.615 | 12.193 | 259.689 | 2.64204 |
| Nd ₂ CoIn ₈ | 4.608 | 12.172 | 258.456 | 2.64149 |
| Sm ₂ CoIn ₈ | 4.583 | 12.101 | 254.168 | 2.64041 |
| Gd ₂ CoIn ₈ | 4.57 | 12.021 | 250.948 | 2.63042 |
| Tb ₂ CoIn ₈ | 4.568 | 12.008 | 250.566 | 2.62872 |
| Dy ₂ CoIn ₈ | 4.561 | 11.99 | 249.425 | 2.62881 |
| Ho ₂ CoIn ₈ | 4.55 | 11.98 | 246.927 | 2.63297 |
| Y ₂ CoIn ₈ | 4.574 | 12.01 | 251.267 | 2.62571 |

same for all the compounds in the series. The integer multiple of the crystallographic site represents the atomic contribution of the individual atoms to the unit cell present at that site. The crystal structure generated by the FullProf program after the refinement of the X-ray pattern is shown in Fig. 3.2. The black lines connecting the two Co planes represent a unit cell. The crystallographic sites represented by each atom within the unit cell are as follows. The In atoms at the $z = \frac{1}{2}$ plane represent a crystallographic e site and those present at the centre of the rare earth planes belong to the crystallographic h site. The Co atoms occupying the corners represent the crystallographic a site and the In atoms near the Co atoms within the cell represent the i site.

The central portion of the $R_2\text{CoIn}_8$ unit cell between the rare earth planes (along the c axis) represents a unit cell of $R\text{In}_3$ phase. The lattice parameters (a and b) of the tetragonal $R_2\text{CoIn}_8$ compounds are also approximately equal to that of the corresponding cubic $R\text{In}_3$ compounds. The remaining Co-In structure below and above the $R\text{In}_3$ unit cell forms a CoIn_2 layer. Hence the $R_2\text{CoIn}_8$ unit cell can be considered as a $R\text{In}_3$ unit cell sandwiched between the two CoIn_2 layers along the c axis. The lattice parameters (a and c) and the unit cell volume of the $R_2\text{CoIn}_8$ compounds are plotted against the corresponding rare earths in Fig. 3.3. The lattice parameters decrease with increasing rare earth atomic number. This is attributed to the well known Lanthana-

nide contraction of the rare earth elements. The decrease in the lattice parameters is smooth without any hump, indicating a similar valency for all the rare earth (R^{3+}) ions in the compounds. Ce_2CoIn_8 has larger lattice parameters than that of Pr_2CoIn_8 , which is a characteristic of the Ce^{3+} compound. The average ratio of the lattice parameters (c/a) of the compounds is ≈ 3.64 , indicating a huge asymmetry in the crystal structure. This increases the structural anisotropy of the compound and also affects the physical phenomena exhibited by them.

Table 3.2 : Crystallographic parameters for Gd_2CoIn_8 compound

| Atom | Site Symmetry | x | y | z | $U_{eq}(\text{\AA}^2)$ | Occupancy |
|------|---------------|------|------|-------|------------------------|-----------|
| Gd | 2g | 0.00 | 0.00 | 0.306 | 0.989 | 2 |
| Co | 1a | 0.00 | 0.00 | 0.000 | 0.875 | 1 |
| In | 2e | 0.00 | 0.50 | 0.500 | 0.058 | 2 |
| In | 2h | 0.50 | 0.50 | 0.308 | 0.023 | 2 |
| In | 4i | 0.00 | 0.50 | 0.118 | 0.107 | 4 |

3.3 Results and Discussions

3.3.1 R_2CoIn_8 ($R = Y, Ce$ and Pr)

3.3.1.1 Magnetization Measurements

In order to verify whether magnetism arises from the magnetic transition element Co, the magnetic susceptibility of the nonmagnetic rare earth compound Y_2CoIn_8 was measured first, which is shown in Fig. 3.4. The curve is nearly temperature independent representing a Pauli paramagnetic behavior. There is a slight upturn at low temperatures, which may be due to a small paramagnetic impurity in the sample. In order to ascertain the effect of such an impurity phase, the susceptibility was fitted to the modified Curie-Weiss law given by

$$\chi = \chi_0 + \frac{C}{T - \theta_p} \quad (3.1)$$

where χ_0 is the temperature independent susceptibility. The fit is shown as a solid line in Fig. 3.4 and gives $\chi_0 = 5.8 \times 10^{-3}$ emu/mole and an effective paramagnetic moment of $0.05 \mu_B$. Such a small value of the effective moment and a huge value of χ_0 indicate that the upturn in the sus-

ceptibility is due to some very minor impurity in the sample. This implies that the Co atoms are nonmagnetic in these compounds.

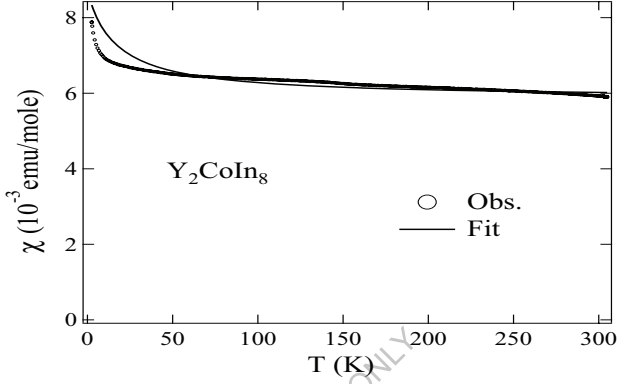


Fig. 3.4: Susceptibility vs Temperature curve for Y_2CoIn_8 with modified Curie-Weiss law fit.

The low temperature magnetic susceptibility of Ce_2CoIn_8 is shown in Fig. 3.5a. The susceptibility increases with decrease in temperature (expected for free spin paramagnetism) and becomes nearly temperature independent at low temperatures after going through a small hump at ≈ 8 K, reminiscent of a magnetic ordering at low temperatures. A similar hump in the susceptibility of Ce_2CoIn_8 single crystals was reported by Chen *et al* [16], also at approximately the same temperature. Such a hump-type behaviour is also found in the susceptibility of CeRhIn_5 [17] which, however, was attributed to the contribution from the orbitally degenerate Kondo impurities [18]. From the magnetization at 2 K, as shown in Fig. 3.6, the possibility of any magnetic ordering with ferromagnetic component can be ruled out. In the absence of neutron diffraction measurements, we also attribute the hump at ≈ 8 K to be arising from the ground state of the Ce ions (considered as Kondo impurities), and not due to any magnetic ordering. The nearly temperature independent susceptibility at low temperatures is the characteristic of heavy fermion compounds [1]. The inverse molar susceptibility, $\chi^{-1}(T)$, plotted in Fig. 3.5b follows a nearly linear temperature dependence above 100 K. The $\chi^{-1}(T)$ data points within the temperature range 100 to 300 K were fitted to the equation (Curie-Weiss law)

$$\chi^{-1} = \frac{T - \theta_p}{C} \quad (3.2)$$

where the Curie constant (C) and the paramagnetic Curie temperature (θ_p) were taken as the fitting parameters. The value of C from the best fit gives an effective moment of $2.2 \mu_B$ and a

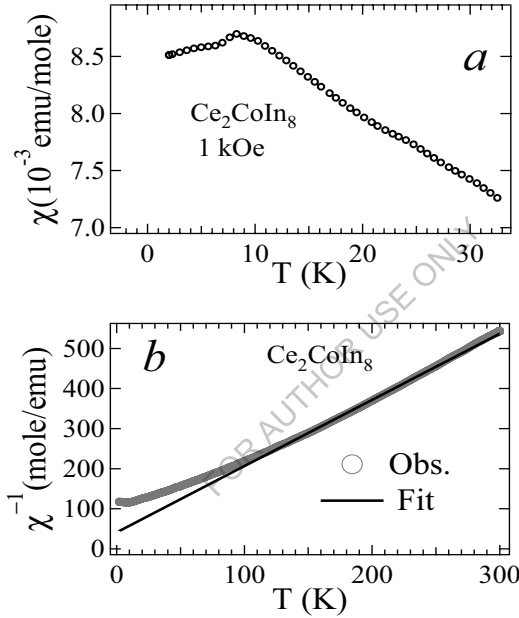


Fig. 3.5: *a:* Susceptibility vs Temperature plot for Ce_2CoIn_8 . *b:* χ^{-1} vs T curve for the same with a Curie-Weiss fit.

paramagnetic Curie temperature of -25 K. The value of the effective moment obtained is less than the value expected for free Ce^{3+} ion ($2.54 \mu_B$). This is generally attributed to the crystal field effects. The large negative value of θ_p normally suggests the presence of antiferromagnetic or Kondo type interactions. The $\chi^{-1}(T)$ curve deviates from the Curie-Weiss behavior below 100 K. Such a behavior is also attributed to the crystal electric field effects which split the six-fold degenerate $J = 5/2$ ground state of Ce^{3+} ion. Since the moment arises only due to the Ce^{3+} ions

(Y_2CoIn_8 is a Pauli-paramagnet, as discussed already), then according to the Kramer's rule, the

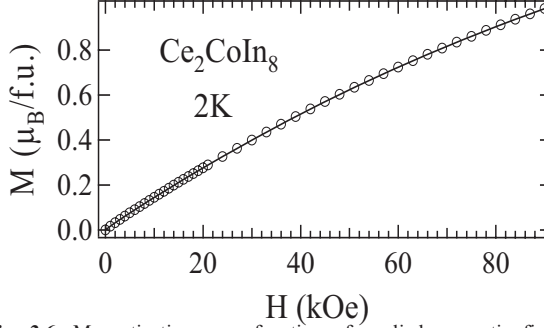


Fig. 3.6: Magnetization as a function of applied magnetic field at 2 K for Ce_2CoIn_8 .

electronic levels in a system containing an odd number of electrons must remain at least two-fold degenerate, provided that no magnetic field is present. We can say that the ground state of Ce_2CoIn_8 , if splits, would be at least a doublet.

The molar susceptibility $\chi(T)$ and the inverse for Pr_2CoIn_8 as a function of temperature are shown in Fig. 3.7a and 3.7b, respectively. The susceptibility shows a Langevin paramagnetic behavior followed by a temperature independent susceptibility at low temperatures (\approx below 16 K). The $\chi^{-1}(T)$ curve follows a linear behavior down to \approx 100 K. The curve was fitted to the Curie-Weiss law (Eqn. (3.2)) which gave an effective moment of $2.6 \mu_B$ and a Curie temperature of -3 K. The deviation of $\chi^{-1}(T)$ from the Curie-Weiss law below \approx 100 K and the reduced paramagnetic moment of Pr^{3+} ion (compared to the expected value of $3.58 \mu_B$) indicate the presence of crystal field effects. The five quadrant magnetic isotherm at 2 K and up to 70 kOe is shown in Fig. 3.8. The linear nature of the magnetic isotherm throughout the applied fields shows the absence of any ferromagnetic ordering. If we consider the effect of crystal field, the $2J+1$ -fold degenerate ground state splits into several sublevels. In the case of rare earth ion possessing an even number of $4f$ electrons, a non-magnetic ground state is expected for a singlet [19] or a non-magnetic doublet [20]. The non magnetic ground state would remain stable down to very low temperatures if the exchange interactions do not exceed a certain critical value [21]. In such cases, the temperature independent Van Vleck susceptibility is expected at low temperatures. In the case of Pr_2CoIn_8 , only Pr^{3+} is magnetic which has two $4f$ electrons, making it a suitable can-

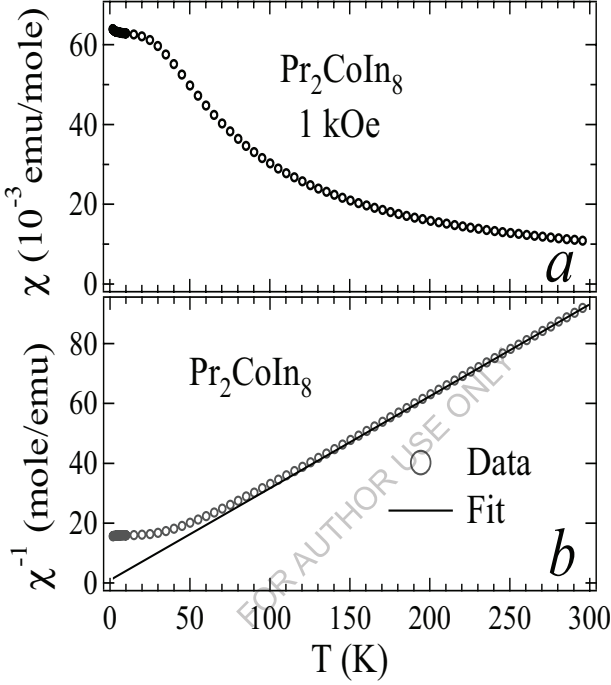


Fig. 3.7: (a) Susceptibility vs Temperature curve. (b) Inverse Susceptibility curve with Curie-Weiss fit (solid line) for Pr_2CoIn_8 .

didate for such a behavior. Considering this, we performed the crystal field calculations on Pr_2CoIn_8 , fitting the $\chi^{-1}(T)$ curve. The $\chi^{-1}(T)$ curve with crystal field fit is shown in Fig. 3.9.

The crystal field levels were calculated using a computer simulation. The crystalline electric field Hamiltonian with the leading terms for tetragonal symmetry is given by

$$H_{CEF} = B_2^0 O_2^0 + B_2^2 O_2^2 \quad (3.3)$$

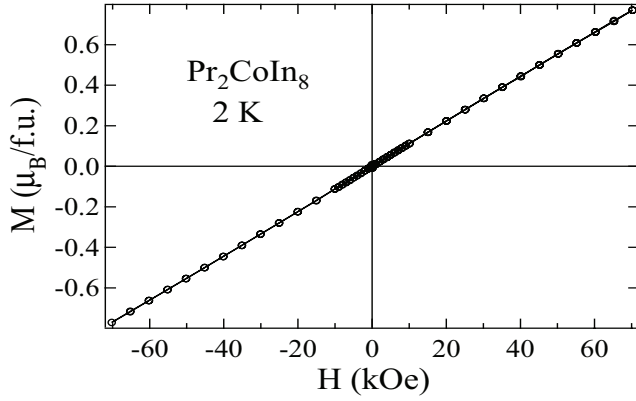


Fig. 3.8: The five quadrant magnetization curve at 2 K for Pr_2CoIn_8

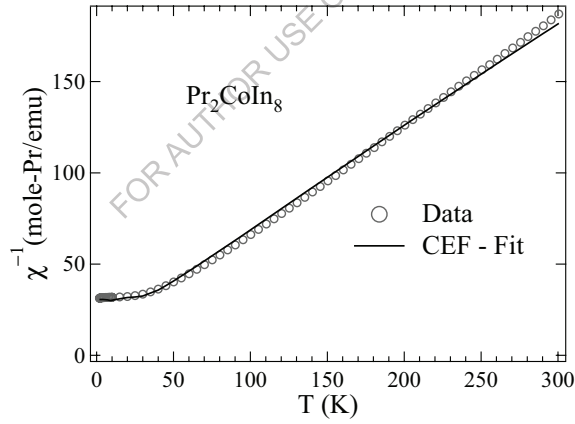


Fig. 3.9: Inverse Susceptibility curve for Pr_2CoIn_8 . The solid line represents a fit for the crystal field effect.

where O_n^m are the Steven's operators in terms of the angular momentum operators and B_n^m are the constants which measure the strength of the crystal field. The above Hamiltonian along with the Zeeman terms ($g_J \mu_B JH$) is diagonalised to obtain the energy eigen values and the energy

eigenvectors for the applied field H parallel and perpendicular to the c axis. The resultant susceptibility arising only from the crystal field, was calculated using the formula

$$\chi_{CEF} = \frac{1}{3}\chi_{\parallel} + \frac{2}{3}\chi_{\perp} \quad (3.4)$$

The eigen functions and the eigen energy values thus obtained under zero field conditions are tabulated in Table 3.3. The ground state is a non-magnetic doublet, which is rarely found. This brings in the possibility of the wave functions adding up to give rise to a non-magnetic state [20].

Table 3.3: Energy levels, state representation, degeneracy and wave functions for crystal field split $J = 4$ state of Pr^{3+} ion in Pr_2CoIn_8 (in the absence of magnetic field).

| Energy (K) | Degeneracy | Wave function |
|---------------|------------|---|
| 0 | 2 | $0.0443 \pm 4\rangle - 0.4096 \pm 2\rangle + 0.8127 0\rangle$ $\mp 0.1719 \pm 3\rangle + 0.6859 \pm 1\rangle$ |
| 33 | 1 | $-0.3463 \pm 3\rangle + 0.6164 \pm 1\rangle$ |
| 35 | 1 | $\pm 0.1212 \pm 4\rangle \mp 0.6966 \pm 2\rangle$ |
| 53 | 1 | $-0.1408 \pm 4\rangle + 0.5591 \pm 2\rangle + 0.5789 0\rangle$ |
| 64 | 1 | $\pm 0.6858 \pm 3\rangle \pm 0.1719 \pm 1\rangle$ |
| 68 | 1 | $0.6164 \pm 3\rangle + 0.3463 \pm 1\rangle$ |
| 94 | 2 | $\mp 0.6966 \pm 4\rangle \mp 0.1212 \pm 2\rangle$ $0.6915 \pm 4\rangle - 0.1401 \pm 2\rangle + 0.0658 0\rangle$ |

3.3.1.2 Resistivity Measurements

We start the discussion on the electron transport characteristics of the above compounds from the phonon contribution which is common to all compounds. Since Y_2CoIn_8 is a purely a non-magnetic compound, its resistivity includes only the phonon contribution. The variation of resistivity with temperature (2 K to 300 K) for Y_2CoIn_8 is shown in Fig. 3.10. The resistivity decreases with decrease in temperature showing a metallic type behavior down to 2 K. The behavior of this non-magnetic compound can be described by the Bloch-Gruneisen relation,

$$\rho(T) = \rho_0 + 4R\theta_D \left(\frac{T}{\theta_D} \right)^5 \int_0^x \frac{x^5 dx}{(e^x - 1)(1 - e^{-x})}, \quad x = \frac{\theta_D}{T} \quad (3.5)$$

where the first term, ρ_0 is the temperature independent residual resistivity and the second term which goes as T^5 accounts for the electron-phonon scattering process. The Debye temperature is denoted by θ_D and the coefficient R gives the strength of the electron phonon interaction. The values of the parameters obtained from the fit (shown as solid line in Fig. 3.10) are: $\theta_D = 190$ K,

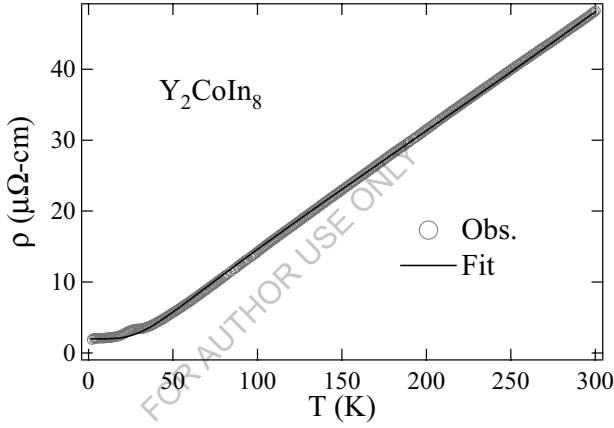


Fig. 3.10: Resistivity of Y_2CoIn_8 . Solid line represents the fit to Bloch-Grüneisen equation (see text).

$R = 0.153 \mu\Omega\text{-cm}$ and $\rho_0 = 2 \mu\Omega\text{-cm}$. The value of R for a typical metal like Cu is $\sim 0.02 \mu\Omega\text{-cm}$ and hence the value obtained in the present case shows that the electron phonon interaction is much stronger in the compound compared to pure metals. The temperature independent resistivity arises at very low temperatures due to the scattering of the conduction electrons by the impurities and the defects in the sample. At low temperatures the phonon contribution becomes vanishingly small and hence contributions from impurities/imperfections dominate. The value of ρ_0 is usually found to be less than $1 \mu\Omega\text{-cm}$ for single crystals and hence the value obtained for our sample, $\rho_0 = 2 \mu\Omega\text{-cm}$ is reasonable for a polycrystalline material.

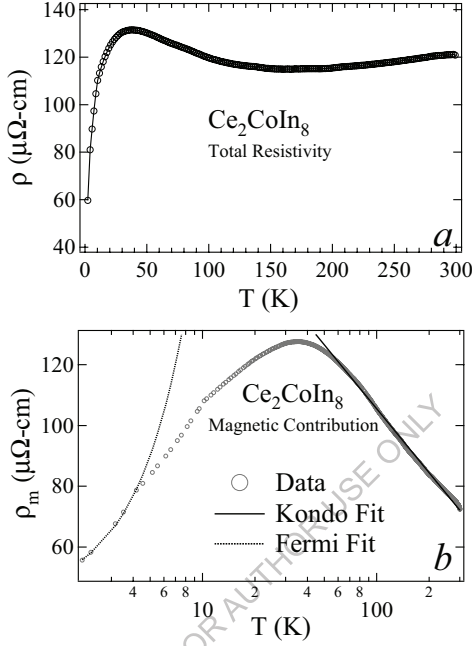


Fig. 3.11: (a) Total resistivity of Ce_2CoIn_8 . (b) Magnetic contribution to the resistivity of Ce_2CoIn_8 as a function of $\log T$. The dashed line show a T^2 fit at low temperature and the solid line is a fit to Kondo formula (3.8).

Figure 3.11a shows the resistivity of Ce_2CoIn_8 as a function of temperature. The curve is typical for materials showing Kondo behavior. When the temperature decreases from 300 K, the resistivity decreases initially. This implies a dominant phononic behavior at high temperatures. Around 160 K, the resistivity shows a minimum and then increases with the decrease in temperature. The increase in resistance is due to the dominating Kondo behavior, which originates from the scattering of the conduction electrons by the Kondo impurities. In the case of Ce_2CoIn_8 , the $4f$ electrons of Ce^{3+} immersed in the Fermi sea of conduction electrons can act as a Kondo impurity. The resistivity then shows a peak at ≈ 35 K and then decreases rapidly with temperature. This behavior is generally attributed to a crossover from strongly incoherent scattering of conduc-

tion electrons at high temperatures to the development of strongly correlated Bloch states at low temperature [22]. Below ≈ 10 K, the resistivity is linear in temperature and such a functional dependence is commonly found in the case of magnetically mediated superconductors [23], which is true for this compound, which shows superconductivity at ~ 0.4 K [15]. The magnetic contribution to the total resistivity of the compound was separated by subtracting the phonon contribution of the Y compound. Now assuming that the phonon contribution to the resistivity of Ce_2CoIn_8 is well described by its nonmagnetic counterpart Y_2CoIn_8 , the total resistivity can be written as

$$\rho_{\text{tot}}(\text{Ce}_2\text{CoIn}_8) = \rho_0(\text{Ce}_2\text{CoIn}_8) + \rho_{\text{ph}}(\text{Y}_2\text{CoIn}_8) + \rho_{\text{mag}}(\text{Ce}_2\text{CoIn}_8) \quad (3.6)$$

where

$$\rho_{\text{ph}}(\text{Y}_2\text{CoIn}_8) = \rho_{\text{tot}}(\text{Y}_2\text{CoIn}_8) - \rho_0(\text{Y}_2\text{CoIn}_8) \quad (3.7)$$

The magnetic contribution $\rho_0 + \rho_{\text{mag}}$ for Ce_2CoIn_8 , separated by this procedure is plotted in Fig. 3.11b. Since the resistivity of Ce_2CoIn_8 does not saturate down to 2 K, the separated magnetic part consists of ρ_0 also. The high temperature part of the resistivity (\approx above 50 K) shows a dominant Kondo behavior and could be fitted to the Kondo formula given by [24]

$$\rho_{\text{mag}} = \rho_0^{\text{SDR}} - c_K \ln(T) \quad (3.8)$$

where $\rho_0^{\text{SDR}} = \rho_0 + \rho_{\text{SDR}}$, c_K is the Kondo coefficient and ρ_{SDR} is the spin disorder resistivity (SDR). Both ρ_{SDR} and ρ_0 are independent of temperature. The best fit to the resistivity curve of the above equation was obtained with $\rho_0^{\text{SDR}} = 246 \mu\Omega \cdot \text{cm}$ and $c_K = 70 \mu\Omega \cdot \text{cm}$. The value of the Kondo coefficient c_K is moderately high and can be compared to the other strong heavy fermion compounds like CeIn_3 , $\text{Ce}_2\text{Pt}_2\text{In}$, etc, with c_K values in the range of 200-300 $\mu\Omega \cdot \text{cm}$. According to Kondo's theory [24], the Kondo coefficient is proportional to the density of states at the Fermi level. This indicates a moderately high density of states at the Fermi level for the given compound. The low temperature part of the magnetic contribution to resistivity can be fitted to the equation

$$\rho(T) = \rho_0 + AT^x \quad (3.9)$$

with $\rho_0 = 43.8 \mu\Omega \cdot \text{cm}$, $A = 4.2 \mu\Omega \cdot \text{cm}/\text{K}^2$ and $x = 1.5$. The deviation of the fit from the pure quadratic behavior ($x = 2$) indicates a non Fermi liquid behavior of the compound. Such a behavior in heavy fermion compounds is generally attributed to spin fluctuations [22]. Similar results have also been reported for CeIrIn_5 , CeRhIn_5 and Ce_2IrIn_8 compounds [16,8,14].

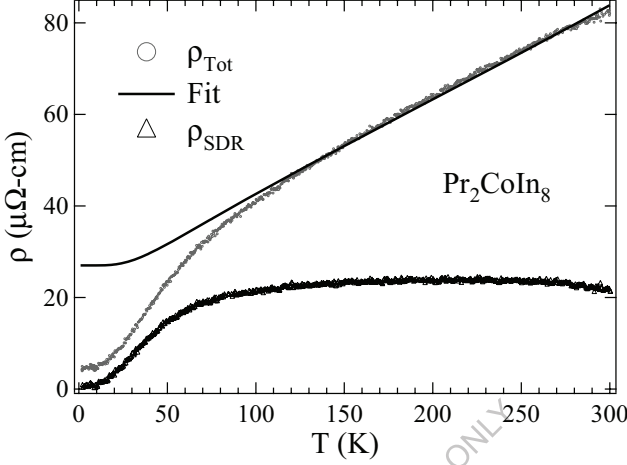


Fig. 3.12: Total Resistivity of Pr_2CoIn_8 . Solid line shows the fit to eqn (3.5) given in the text for the high temperature part of the resistivity. Figure also shows the difference plot obtained after subtracting the phonon contribution from the total resistivity which gives the Spin Disorder Resistivity with a CEF effect at low temperatures.

The total measured resistivity for Pr_2CoIn_8 is given in Fig. 3.12 from 2 to 300 K. The curve initially shows a metallic behavior, falling linearly with temperature. Around 120 K the curve deviates from the linear behavior and falls rapidly with temperature and saturates at low temperatures. Since there is no magnetic ordering down to 2 K, the deviation of the resistivity from the expected path can be attributed to the crystal field effects, since the crystal field effects at approximately the same temperature is evident from the susceptibility data. The fit to the resistivity curve above 100 K to the B-G equation (3.5) gives the values $\theta_D = 190$ K, $R = 0.19 \mu\Omega\text{-cm}$ and $\rho_0 = 27 \mu\Omega\text{-cm}$. Here ρ_0 includes both the residual resistivity and ρ_{SDR} , since it is a magnetic compound. If we take the actual value of residual resistivity from the experimental curve as $4 \mu\Omega\text{-cm}$, then we get $\rho_{SDR} = 23 \mu\Omega\text{-cm}$. Subtracting the phonon contribution (obtained after subtracting ρ_0 from the fit) from the total resistivity should also give a constant spin disorder resistivity ($\approx 23 \mu\Omega$). However, the value of ρ_{SDR} shows deviation at low temperatures (< 100 K) as

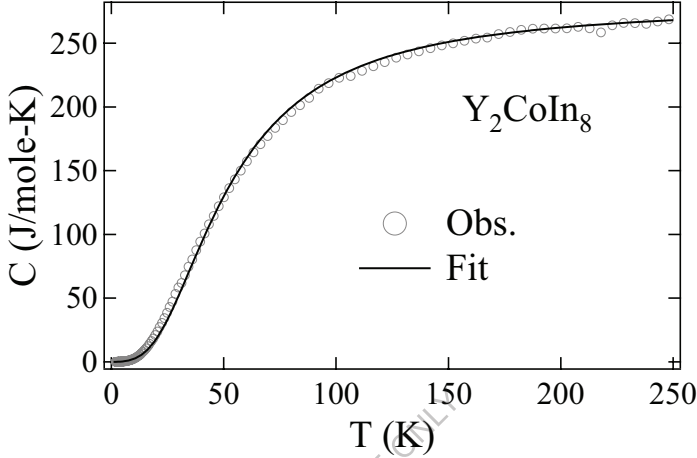


Fig. 3.13: Heat capacity of Y_2CoIn_8 with a fit including Debye and electronic terms.

shown in Fig. 3.12 which can again be attributed to a dominating crystal field effect at low temperatures. Comparing the parameters obtained from the fit with that of the non magnetic Y_2CoIn_8 ($\theta_D = 190$ K, $R = 0.153 \mu\Omega\text{-cm}$ and $\rho_0 = 2 \mu\Omega\text{-cm}$) it can be seen that the Debye temperature remains the same, since it depends on the structure and the lattice parameters of the compound which do not vary appreciably. The electron phonon coefficient R has increased for Pr_2CoIn_8 implying an increase in the electron phonon interactions compared to Y_2CoIn_8 . This result is also supported by the value of the electronic specific heat coefficient γ (as discussed below) which is higher for Pr_2CoIn_8 (21.3 mJ/mole- K^2) than Y_2CoIn_8 (13 mJ/mole- K^2).

3.3.1.3 Heat Capacity Measurements

Y_2CoIn_8 is the nonmagnetic compound in the series and hence one expects only the phononic and electronic contributions to the specific heat of the compound. Then the total specific heat can then be written as

$$C_{\text{tot}} = C_{\text{elec}} + C_{\text{phonon}} = \gamma T + 9nR \left(\frac{T}{\theta_D} \right)^3 \int_0^{\frac{\theta_D}{T}} \frac{x^4 e^x dx}{(e^x - 1)^2}, \quad x = \frac{\theta_D}{T} \quad (3.10)$$

where γ is the electronic coefficient, n ($= 11$) is the number of atoms in the formula unit, R is the gas constant and θ_D is the Debye temperature. The specific heat curve for Y_2CoIn_8 was fitted to equation (3.10), shown as solid line in Fig. 3.13, which gave $\theta_D = 211$ K. The value of $\gamma = 13$ mJ/mole-K² was estimated from the extrapolation of the C/T vs T^2 curve to the $T = 0$ axis. This Debye temperature is different from that obtained from the analysis of the resistivity data ($\theta_D = 190$ K). Hence the θ_D value obtained from the specific heat was put back in the Bloch-Gruneisen relation and the resistivity curve was fitted again. There was only a minor change in the curve, indicating a negligible dependence of resistivity on the Debye temperature. However, the value of θ_D obtained from resistivity did not agree with the heat capacity fit. Hence the actual

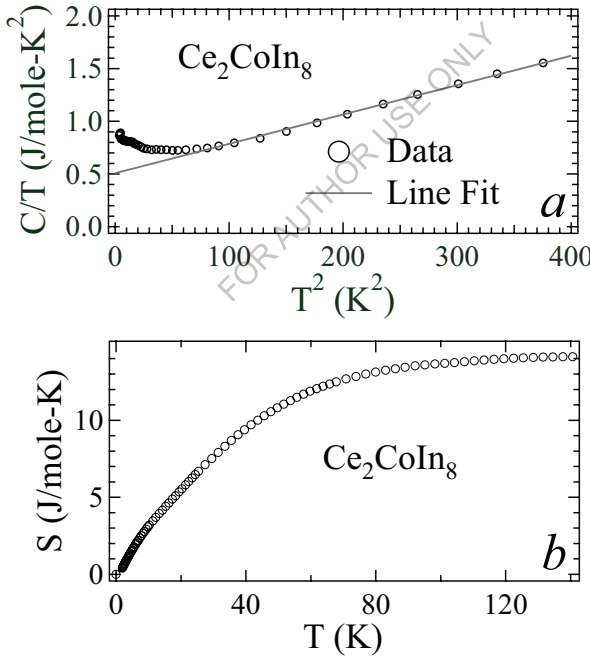


Fig. 3.14: *a:* C/T vs T^2 curve for Ce_2CoIn_8 with a straight line fit. *b:* Magnetic entropy for Ce_2CoIn_8 obtained by subtracting the phonon part using Y_2CoIn_8 .

value of θ_D is taken as 211 K.

Fig. 3.14a shows the C/T vs T^2 curve for Ce_2CoIn_8 . The curve decreases linearly with temperature up to ≈ 9 K and then deviates with an upward turn at low temperatures. The γ value obtained from the intercept of the straight line at low temperature is 250 mJ/mole-K²-Ce. The γ value reported for the single crystal of this compound is 500 mJ/mole-K²-Ce [11]. However, they have obtained this value by taking the value at the lowest temperature. If we also take the value of γ at the lowest temperature then we get $\gamma = 460$ mJ/mole-K²-Ce. Heavy fermion means an increase in the effective mass of the conduction electrons. The effective mass of the electron, m^* is given by

$$m^* = \frac{\hbar^2 k_F^2 \gamma}{\pi^2 (Z/\Omega) k_B^2} \quad (3.11)$$

where k_F is the Fermi wave vector given by $k_F = (3\pi^2 Z/\Omega)^{1/3}$ and Z is the number of conduction electrons per unit cell. Other symbols have their usual meaning. Substituting the values of $Z = 6$ (assuming that Ce contributes 3 electrons per atom), $\Omega = 263.75 \text{ \AA}^3$ (unit cell volume) and $\gamma = 460$ mJ/mole-K²-Ce in the above equation we get $m^* \approx 55m_e$, where m_e is the free electron mass. In the case of heavy fermion compounds, the Wilson ratio (ratio of the susceptibility to that of the electronic specific heat) can be calculated as

$$\frac{\chi_0}{\gamma} = \frac{3\mu_B^2}{\pi^2 k_B^2} \quad (3.12)$$

where χ_0 is the susceptibility at 0 K and the other parameters have their usual meanings. The ratio comes out to be 1.8×10^{-9} , which is comparable with the ideal value of 1.372×10^{-9} .

The magnetic contribution to the specific heat of the compound was isolated by subtracting the specific heat of the non magnetic counterpart Y_2CoIn_8 (after renormalizing for the atomic mass). The magnetic contribution to the entropy was then calculated using the relation

$$S_{\text{mag}}(T) = \int_0^T \frac{C_{\text{mag}}(T)}{T} dT \quad (3.13)$$

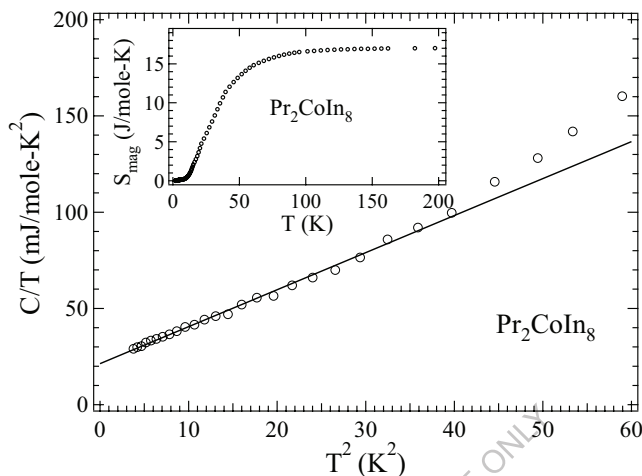


Fig. 3.15: C/T vs T^2 curve for Pr_2CoIn_8 with a straight line fit (main panel). Inset shows the magnetic entropy for Pr_2CoIn_8 .

The temperature variation of the calculated of S_{mag} is shown in Fig. 3.14b. The maximum value comes out to be 14.2 J/mole-K-Ce, which is less than the theoretical value $R \ln(2J+1) = 14.8$ J/mole-K, where $J = 5/2$ for Ce^{3+} ion and $R = 8.314$ J/mole-K is the gas constant. The exact reason for the low value is not known but a possibility can be attributed to the crystal field effects. The effective moment was also less than that expected due to the same reason (already discussed in the magnetization result).

The heat capacity behavior of Pr_2CoIn_8 is similar to that of the nonmagnetic compound Y_2CoIn_8 . The low temperature C/T vs T^2 curve is shown in Fig. 3.15. The straight line fit to the curve gives the value of electronic coefficient γ to be 21.3 mJ/mole- K^2 . The magnetic contribution to the heat capacity was isolated by subtracting the heat capacity of Y_2CoIn_8 . The value of magnetic entropy obtained using the equation (3.12) is 17.2 mJ/mole- K^2 -Pr (inset of Fig. 3.15). The value is less than that expected for a Pr^{3+} ion (18.2 mJ/mole- K^2). The reason may be again due to the crystal field effects. The magnetic contribution to the heat capacity at low temperatures is shown in Fig. 3.16. Since there is no magnetic ordering in this compound, the peak observed at

low temperatures can be attributed to a Schottky type anomaly. In order to verify this, the Schottky contribution to the heat capacity was calculated using the equation

$$C_{\text{Sch}}(T) = R \left[\frac{\sum_i g_i e^{-E_i/T} \sum_i g_i E_i^2 e^{-E_i/T} - \left[\sum_i g_i E_i e^{-E_i/T} \right]^2}{T^2 \left[\sum_i g_i e^{-E_i/T} \right]^2} \right] \quad (3.14)$$

where R is the gas constant, E_i is the energy level (in units of temperature, as given in Table 3.3) and g_i is the degeneracy of the energy level. The curve obtained using the above equation is also plotted as a solid line in Fig. 3.16. Even though the agreement is not very good, the shape of the calculated curve resembles that of the observed curve. It is quite possible that this deviation occurs since all the crystal field parameters are not included in the calculation of the magnetic susceptibility.

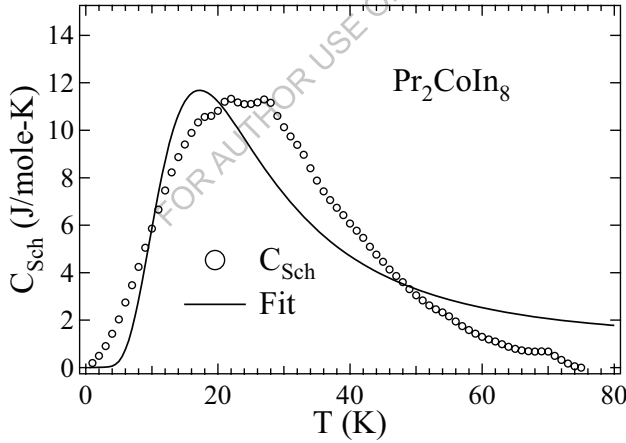


Fig. 3.16: Schottky anomaly obtained by subtracting the heat capacity of Y_2CoIn_8 , with a fit to the Schottky equation (3.14).

3.3.2 $R_2\text{CoIn}_8$ ($R = \text{Nd, Sm, Gd, Tb, Dy and Ho}$)

Unlike the Ce and Pr compounds, the other magnetic rare earth compounds in $R_2\text{CoIn}_8$ series undergo antiferromagnetic transitions at low temperatures. The transition temperatures are

given in Table 3.4. The transition temperatures are compared with the corresponding $R\text{In}_3$ com-

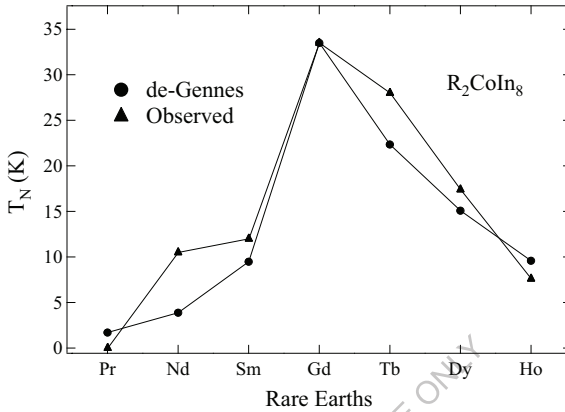


Fig. 3.17: Neel temperature of $R_2\text{CoIn}_8$ series of compounds plotted with their corresponding expected de-Gennes scaling values.

pounds which act as a basic building block for these compounds. The transition temperatures of $R_2\text{CoIn}_8$ compounds decrease compared to the corresponding $R\text{In}_3$ compounds except for Nd_2CoIn_8 where it increases ($T_N = 10.5$ K) compared to NdIn_3 ($T_N = 7$ K). According to the de-Gennes scaling, the T_N of the isostructural members of the rare earth series is proportional to $(g_J - 1)^2 J(J+1)$, where g_J is the Lande factor and J is the total angular momentum. The Neel temperatures of $R_2\text{CoIn}_8$ compounds are shown in Fig. 3.17 along with the corresponding expected values obtained using the de-Gennes scaling. The Neel temperatures of Nd_2CoIn_8 and Tb_2CoIn_8 are found to vary appreciably from their expected values. The reason may be attributed to the strong crystal field effects. Because of the asymmetric structure of the compounds the crystal field plays a crucial role in determining the properties of these compounds.

3.3.2.1 Gd_2CoIn_8

The low temperature susceptibility of Gd_2CoIn_8 is shown in Fig. 3.18a for applied fields of 0.2 kOe and 50 kOe. The susceptibility at 0.2 kOe shows an antiferromagnetic type transition

Table 3.4: Neel temperatures for $R\text{In}_3$ and $R_2\text{CoIn}_8$ series of compounds. Paramagnetic Curie temperature (θ_p) and effective magnetic moment (μ_{eff}) for $R_2\text{CoIn}_8$ compounds are also given.

| R | $R\text{In}_3$ | $R_2\text{CoIn}_8$ | | |
|----|----------------|--------------------|----------------|--------------------------------|
| | T_N (K) | T_N (K) | θ_p (K) | μ_{eff} (μ_B) |
| Y | P-P | P-P | - | - |
| Ce | HF | P | -3 | 2.6 |
| Pr | P | P | -9 | 3.6 |
| Nd | 7 | 10.5 | -5 | 3.6 |
| Sm | 16 | 12 | -7 | 0.8 |
| Gd | 45 | 33.5 | -39 | 7.9 |
| Tb | 36 | 30 | -19 | 9.7 |
| Dy | 23 | 17.4 | -11 | 10.6 |
| Ho | 11 | 7.6 | -2 | 10.6 |

P-P : Pauli paramagnet, HF : heavy fermion, P : Paramagnetic

at ≈ 33 K and then shows an upturn at ≈ 5 K. The susceptibility at 50 kOe also shows a similar behaviour, but the sharpness of the upturn has decreased because of the broadening of the antiferromagnetic peak. The upward turn at low temperatures may be due to some paramagnetic impurity in the sample (undetected in the X-ray) or due to a spin reorientation with a ferromagnetic component arising at low temperatures. However, the magnetic isotherm at 2 K (inset of Fig. 3.18b) shows a straight line behavior, which excludes the presence any ferromagnetic component in the compound at that temperature. The inverse susceptibility is fitted to the Curie-Weiss law as shown in Fig 3.18b which gives an effective moment of $7.9 \mu_B$ and a paramagnetic curie temperature of -39 K (Table 3.4). The large negative value of the paramagnetic Curie temperature also indicates a strong antiferromagnetic interaction among the Gd moments.

The heat capacity curve of Gd_2CoIn_8 is shown in Fig. 3.19. It shows an anomaly at Neel temperature. The magnetic entropy obtained is 17.1 J/mole-K-Gd (inset of Fig. 3.19), which is

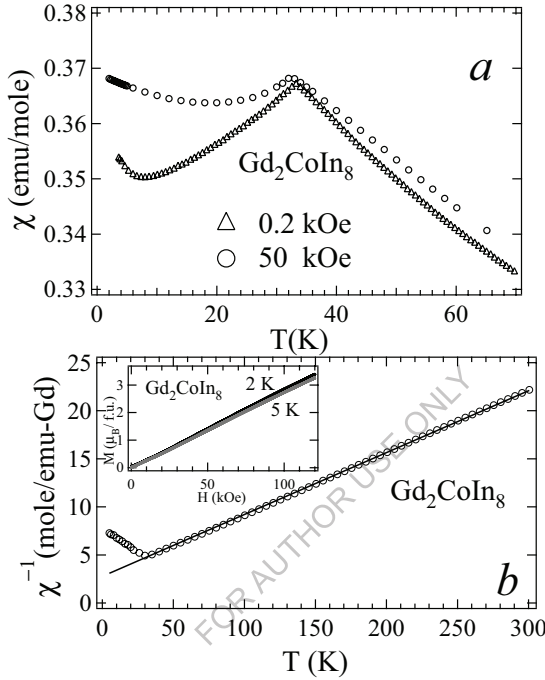


Fig. 3.18: *a*: Susceptibility vs Temperature at various applied magnetic fields for Gd_2CoIn_8 . *b*: χ^{-1} vs Temperature with a Curie-Weiss fit in the paramagnetic region. Inset of (b) shows the magnetic isotherms at 2 K and 5 K.

close to the expected value of 17.28 J/mole-K-Gd. The resistivity of the compound was measured from 2-300 K, which is shown in Fig.3.20*a*. Resistivity shows a normal metallic behavior down to T_N and drops below T_N because of the vanishing spin disorder resistivity. In the ordered state, the resistivity gives a better fit to T^2 behavior rather than a T^3 behavior (see Fig.3.20*a*). A T^3 behavior is expected for an antiferromagnet, whereas the T^2 behavior is usually associated with an isotropic ferromagnet [25]. The exact reason for the T^2 behavior even though the compound shows an antiferromagnetic ordering is not clear. The magnetoresistance (MR) of the compound

at 2 K as a function of field is shown in Fig.3.20*b*. The magnetoresistance was calculated using the standard relation

$$\text{MR} = \frac{\rho(H) - \rho(0)}{\rho(0)} \quad (3.15)$$

It shows a monotonic increase of the positive magnetoresistance as expected for an antiferromagnet.

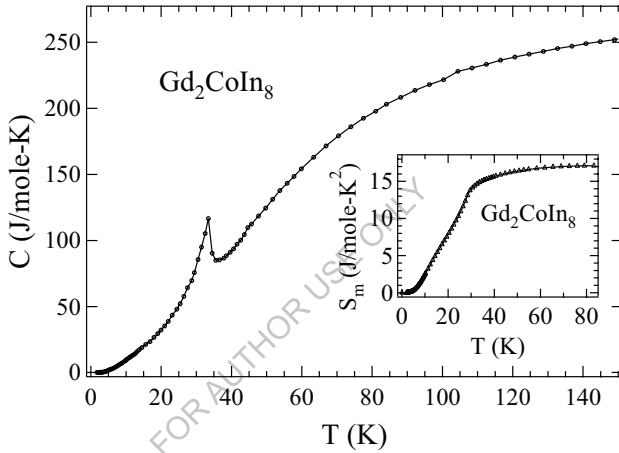


Fig. 3.19: Heat capacity curve of Gd_2CoIn_8 . Inset shows the variation of the magnetic entropy.

3.3.2.2 Dy_2CoIn_8

The low temperature part of the susceptibility for Dy_2CoIn_8 at various applied magnetic fields is shown in Fig. 3.21*a*. The magnetization at low fields ($H = 1$ kOe) indicates the presence of two magnetic transitions, one transition at 17 K and the other near 5 K (shown by an arrow in the figure). The magnetic transition at 17 K appears to be of antiferromagnetic in nature and the transition near 5 K may be due to a spin reorientation [26]. No apparent deviation was observed between the FC and ZFC magnetization measurements at 1 kOe, ruling out any possibility of spin glass type ordering. At 50 kOe, the 17 K transition broadens and shifts to ~ 15 K where as the magnetic ordering near 5 K disappears. The shifting of the peak towards low temperatures is expected for an antiferromagnetic type ordering. At still higher fields ($H = 90$ kOe), both the

ordering features in the magnetic susceptibility disappear and the susceptibility at low tem-

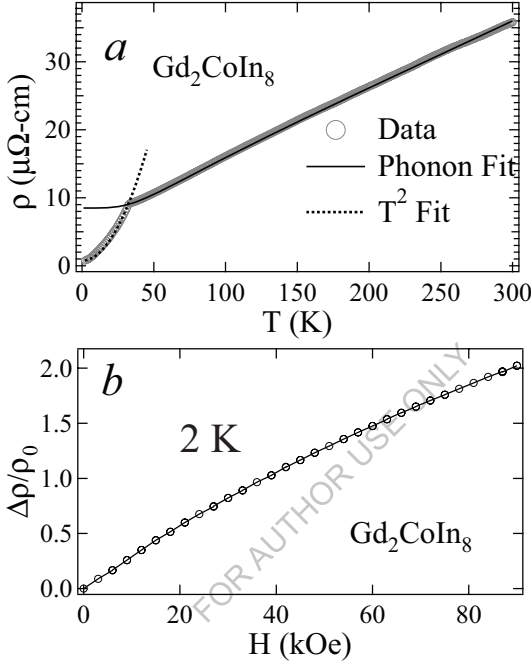


Fig. 3.20: *a*: Resistivity curve for Gd_2CoIn_8 with a fit to the phononic contribution in the paramagnetic state and T^2 fit in the ordered state. *b*: Magnetoresistance curve for the same.

peratures shows a behavior similar to that of ferromagnetic ordering. The magnetic susceptibility in the paramagnetic state obeys a Curie-Weiss law behavior and was fitted to equation (3.1), as shown in Fig. 3.21*b*. The values obtained from the fit are given in Table 3.4. In order to trace out

the origin of the two peaks in the susceptibility data, the magnetization was also measured as a function of applied magnetic fields at various temperatures, the plots of which are shown in Fig. 3.22. The curves start as straight lines, confirming the presence of AFM ordering, but it is clear that two metamagnetic transitions also occur at 36 kOe (denoted as H_{M1}) and 82 kOe (H_{M2}).

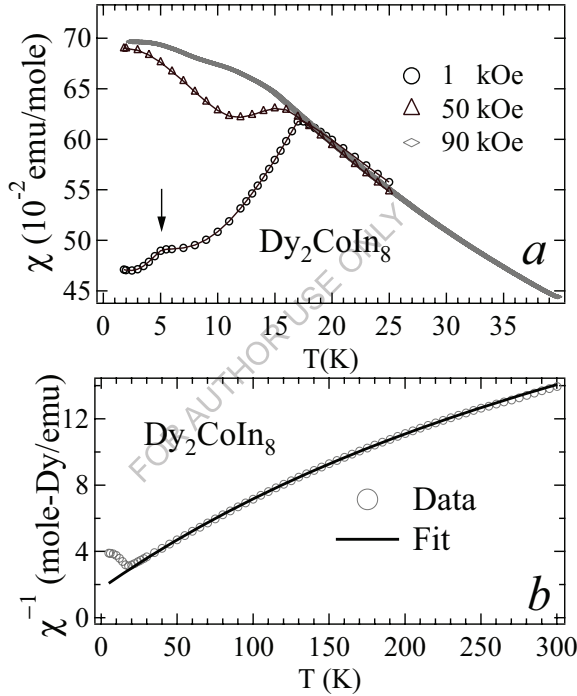


Fig. 3.21: *a*: Magnetic susceptibility vs Temperature at various fields for Dy_2CoIn_8 . *b*: χ^{-1} vs Temperature with a modified Curie-Weiss fit in the paramagnetic region.

The presence of these metamagnetic transitions supports our assumption that the magnetic transition near 5 K may be due to a reorientation of the spins in the antiferromagnetically ordered state. The metamagnetic transitions in the magnetic isotherm at 2 K are sharp and the sharpness fades with the increasing temperature, giving only a straight line at 25 K. Since the compound under-

goes two metamagnetic transitions at high fields, $H_{M1} \sim 36$ kOe and $H_{M2} \sim 82$ kOe, the broadening in susceptibility as a function of temperature for applied fields of $H = 50$ kOe and 90 kOe is expected as the system undergoes transitions to spin re-oriented states with increased magnetization below the ordering temperatures. Application of a field higher than H_{M2} (90 kOe) shifts the ordering temperature further and the saturation of the magnetization is observed at low temperatures. The equivalent moment obtained at 120 kOe is $7 \mu_B/\text{f.u.-Dy}$, which is less than the theoretical saturation moment of Dy^{3+} ion ($10 \mu_B$). But the value is high enough for the com-

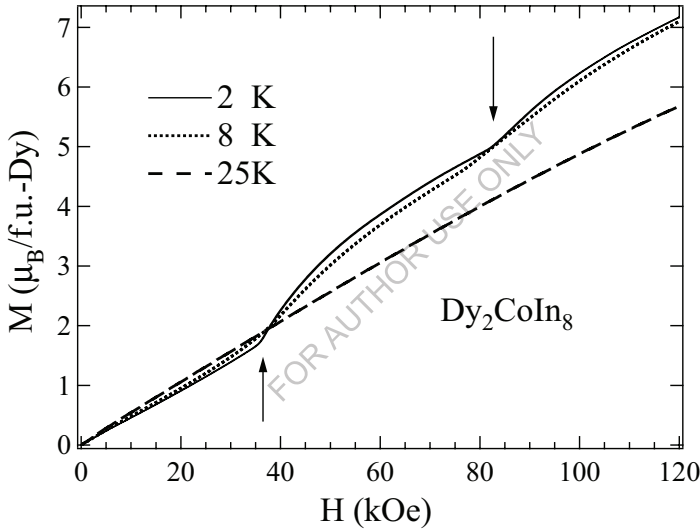


Fig. 3.22: Magnetization vs Field at various Temperatures for Dy_2CoIn_8 .

pound to be in the ferromagnetic state.

The magnetic behavior of Dy_2CoIn_8 seen in the magnetization is also reflected in the specific heat data, the results of which are given in Fig. 3.23. In zero applied field, the specific heat shows two peaks, in agreement with the low field magnetization measurements. As the field is increased, the position of the peak at 17 K gets shifted towards lower temperatures as expected for an antiferromagnetic transition whereas the peak near 5 K gets smeared out. This could possibly be related to the metamagnetic transitions observed in this compound. However, the effect of

these metamagnetic transitions in specific heat measurements can only be seen as a reduction in the peak height at the ordering temperatures as shown in Fig. 3.23. The magnetic entropy of the compound comes out to be ≈ 23.3 J/mole-K-Dy. The value is close to the theoretically expected

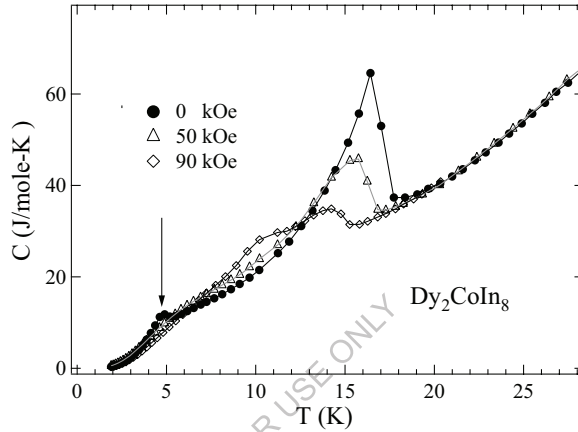


Fig. 3.23: Low temperature heat capacity curve for Dy_2CoIn_8 at 0, 50 and 90 kOe.

value of ≈ 23.1 J/mole-K-Dy.

The resistivity behaviour of Dy_2CoIn_8 is shown in Fig. 3.24. The resistivity shows a usual metallic behavior down to the ordering temperature of ≈ 17 K and then drops rapidly below the ordering temperature. In the paramagnetic region the curve was fitted to the Bloch-Grüneisen relation (Eqn. (3.5)) which is shown as the solid line in the figure. The best fit gave the parameters, $\theta_D = 190$ K, $R = 0.163 \mu\Omega\text{-cm}$ and $\rho_0 = 11.2 \mu\Omega\text{-cm}$. The electron phonon coefficient R is greater than that of the nonmagnetic counterpart Y_2CoIn_8 . This indicates an increase in the electron phonon interaction in this compound. ρ_0 is the sum of the residual and the spin disorder resistivity, $\rho^{SDR} + \rho_{res}$. The residual resistivity can not be isolated because the curve does not saturate at low temperatures. The spin disorder resistivity plays an important role in the resistivity of the magnetic materials. In the paramagnetic state it has a constant value since the spins are randomly aligned, and in the ordered state depending upon the ordering (canted spins) it has some

finite value. In the ideal case when the spins are parallel, it should have a minimum value. The resistivity behavior in the antiferromagnetically ordered state, when the anisotropy is present, is given by [32]

$$\rho = \rho_0^s + b\Delta^2 \sqrt{\frac{k_B T}{\Delta}} e^{-\Delta/k_B T} \left[1 + \frac{2}{3} \left(\frac{k_B T}{\Delta} \right) + \frac{2}{15} \left(\frac{k_B T}{\Delta} \right)^2 \right] \quad (3.16)$$

where b is a constant and Δ represents the anisotropy energy gap. ρ_0^s represents the sum of the residual resistivity and the spin disorder resistivity in the ordered state, if present. The resistivity data in the ordered state could be fitted to two different curves generated by the above equation for two different values of ρ_0^s and the same value of Δ (see Fig. 3.25). The curve fitted to the data above 5 K gives $\rho_0^s = 2.3 \mu\Omega\text{-cm}$ and that below ≈ 5 K gives $\rho_0^s = 1.4 \mu\Omega\text{-cm}$ with $\Delta = 4$ K. The lower value of ρ_0^s below 5 K suggests that the spins are more ordered below 5 K when compared to the state above 5 K. Now considering the anomaly in the specific heat and the mag-

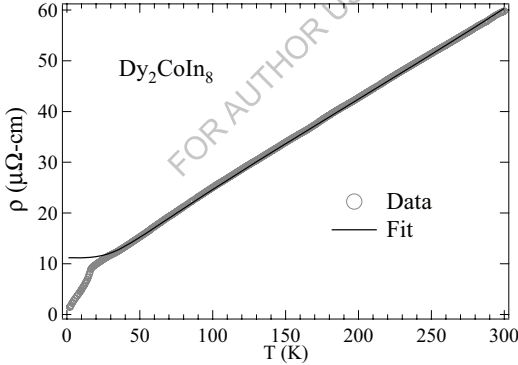


Fig. 3.24: Resistivity cure for Dy_2CoIn_8 with a B-G fit in the paramagnetic region

netization measurements at approximately the same temperature, we confirm that the anomaly at 5 K is due to a spin reorientation. Fig. 3.26 shows the magnetoresistance behavior of the compound at 2 K as a function of applied field. Initially the resistivity increases with the field upto ≈ 83 kOe and then decreases with increase in the field. This field corresponds to the second metamagnetic transition in the magnetization behavior of the compound. The decrease in the

magnetoresistance with field is the characteristic of a ferromagnetic compound. Hence we can say that the field induced metamagnetic transition drives the compound to a ferromagnetic state above 83 kOe.

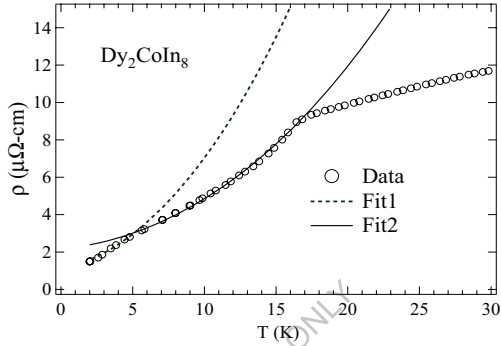


Fig. 3.25: Low temperature ordered state resistivity for Dy_2CoIn_8 with a fit to equation (3.16).

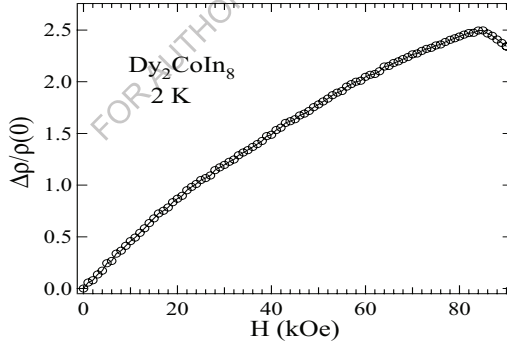


Fig. 3.26: Magnetoresistance for Dy_2CoIn_8 at 2 K.

3.3.2.3 Ho_2CoIn_8

The low temperature susceptibility of Ho_2CoIn_8 at various fields is shown in Fig. 3.27a. The low field susceptibility (1 kOe) indicates the presence of an antiferromagnetic transition at \approx

7.5 K. The susceptibility at 50 kOe show a huge broadening of the antiferromagnetic peak and it shifts towards low temperatures, consistent with an AFM ordering. At 80 kOe the peak vanishes altogether and the susceptibility increases with temperature. The linear behavior of the magnetic isotherm at 2 K at low fields (below 20 kOe) (Fig. 3.27*b*) proves the antiferromagnetic behavior

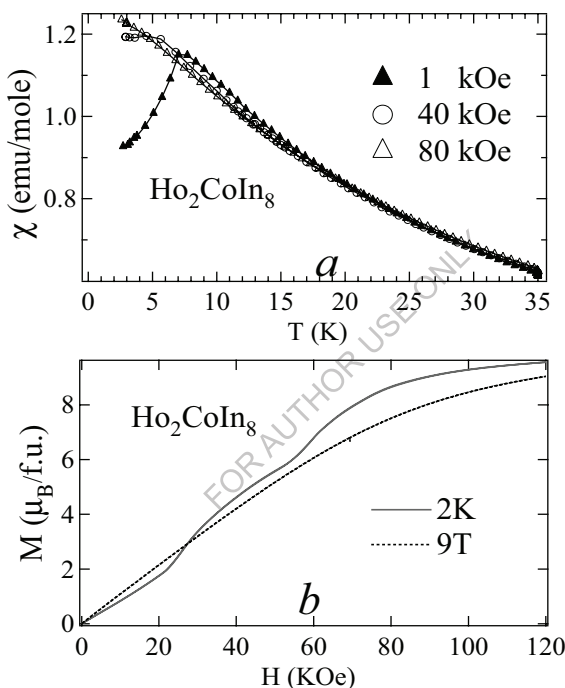


Fig. 3.27: *a*: Susceptibility vs Temperature at various fields for Ho_2CoIn_8 .
b: Magnetic isotherms at 2 K and 9 K.

of the compound. Increase in the field causes the compound to undergo two metamagnetic transitions, one at ≈ 25 kOe and another at ≈ 55 kOe. Further increase in the field produces a saturation with a magnetization of $\approx 9.1 \mu_B$ at 120 kOe. The magnetization value is near to the saturation value of Ho^{3+} ion ($10 \mu_B$). This suggests that the compound is nearly in the ferromagnetic state at 120 kOe.

The low temperature heat capacity (HC) of the compound at various fields is shown in Fig. 3.28. When the magnetic field is zero, the HC shows an anomaly at the antiferromagnetic transition temperature of the compound. Application of a field (50 kOe) broadens the peak and splits it to 3 different peaks. This may be due to the combined effect of magnetic and crystal field effects on the energy levels. At 90 kOe all the peaks vanish altogether, consistent with that found in the magnetization behavior.

The resistivity curve for Ho_2CoIn_8 is shown in Fig. 3.29a. The resistivity shows its usual metallic behavior down to the ordering temperature of ≈ 7.5 K and then drops rapidly below the ordering temperature. The solid line in the figure represents the fit to the Block-Gruneisen relation (Eqn. (3.5)) in the paramagnetic region. The best fit gave the parameters $\theta_D = 190$ K, $R = 0.175 \mu\Omega\text{-cm}$, and $\rho_0 = 8 \mu\Omega\text{-cm}$. In the ordered state the resistivity curve was fitted to Eqn. (3.16) (dotted line in Fig. 3.29b), which is found to be not in a good agreement with the data. However, it was found that the data below the magnetic ordering could well be fitted to a linear behavior, shown as the solid line in Fig. 3.29b. The reason for this straight line behaviour is not

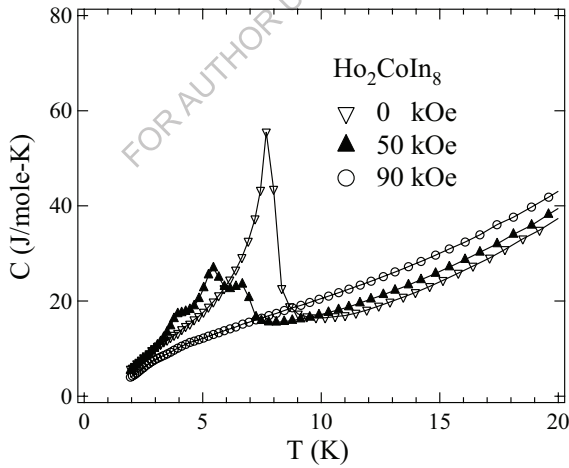


Fig. 3.28: Low temperature heat capacity curve at various fields for Ho_2CoIn_8 .

clear. The magnetoresistance of the compound at 2 K is shown in Fig. 3.30 as a function of field. Initially the magnetoresistance increases with increase in the field showing a behavior typical for

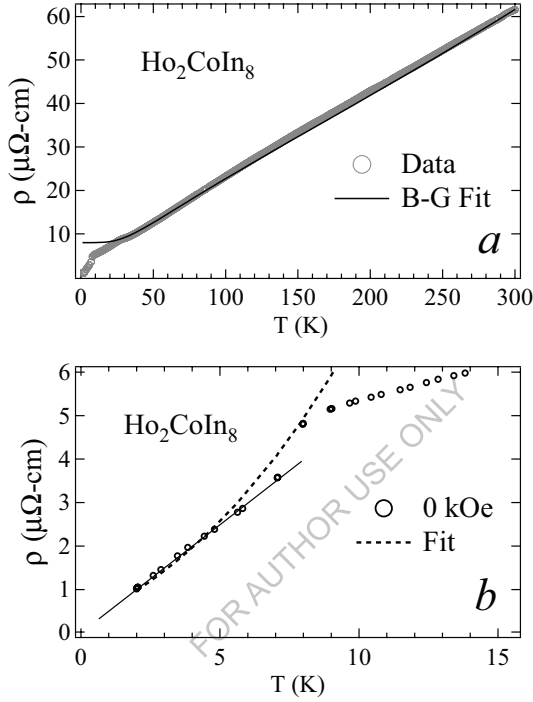


Fig. 3.29: *a*: Resistivity cure for Ho_2CoIn_8 with a B-G fit in the paramagnetic region. *b*: Low temperature ordered state resistivity with a fit to equation (3.16) (dotted line).

an antiferromagnet. At ≈ 22 kOe a signature of its deviation from the initial path is seen, which corresponds to the 1st metamagnetic transition in the magnetization isotherm. At ≈ 54 kOe the curve takes a downward turn and then decreases with field up to ≈ 80 kOe, after which, it becomes nearly temperature independent. The decrease in the magnetoresistance again indicates the ferromagnetic state achieved by the compound after the 2nd metamagnetic transition.

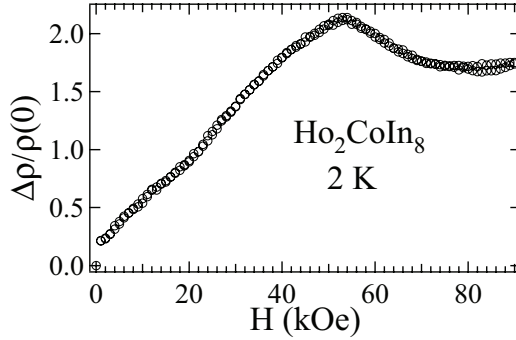


Fig. 3.30: Magnetoresistance for Ho_2CoIn_8 the same at 2 K.

3.3.2.4 Sm_2CoIn_8

The low temperature susceptibility of Sm_2CoIn_8 at 0.5 kOe, 1 kOe and 50 kOe is shown in Fig. 3.31. The low field susceptibility (0.5 kOe) shows an antiferromagnetic type peak at ≈ 12 K and an upturn below 5 K. The susceptibility for fields of 1 kOe and 50 kOe also shows the same antiferromagnetic type peak at ≈ 12 K, but the susceptibility value below the antiferromagnetic transition shows an increase. To further investigate the magnetic behaviour, magnetization was measured as a function of applied field at 2 K. The magnetic isotherm is very peculiar, as shown in Fig. 3.32. As the field is increased from zero, the magnetization remains almost zero initially and then increases linearly with field for $H > 4$ kOe. At $H \approx 26$ kOe, the magnetization shows a sharp increase, reminiscent of a metamagnetic transition. At still higher fields, the magnetization curve tries to saturate. When the field is decreased, the curve shows a hysteresis behavior similar to that of a ferromagnet. After that, within a complete hysteresis cycle the magnetization behaves like a ferromagnet, forgetting its original antiferromagnetic behavior (a straight line in the M - H curve) at low fields in the virgin curve. Before discussing these results in detail, let us look at the inverse susceptibility curve (Fig. 3.33). It is clear that the susceptibility does not follow a Curie-Weiss behaviour. The first excited state of Sm^{3+} ion lies very near to the ground state ($\Delta E_{7/2-5/2} \approx 1400$ K). This results in thermally induced mixing of the excited states with the ground state. Hence the susceptibility in the paramagnetic state can not be fitted to the Curie-Weiss Law. The Curie-Weiss Law modified to fit the susceptibility in such cases is given by [27]

$$\chi = \frac{N_A}{k_B} \left(\frac{\mu_{\text{eff}}^2}{3(T - \theta_p)} + \frac{\mu_B^2}{\delta} \right) \quad (3.17)$$

where N_A is the Avogadro number, k_B is the Boltzmann's constant, μ_B is the Bohr magneton, μ_{eff} is the effective magnetic moment in units of μ_B , θ_p is the paramagnetic Curie temperature and $\delta = 7\Delta E/20$ in which ΔE is the difference between the ground state and the first excited state. For Sm^{3+} ion, the first term in the above equation represents a Curie-Weiss contribution from $J = 5/2$ ground state, while the second term is the temperature independent Van Vleck correction arising from the accessible first excited $J = 7/2$ state. The solid line in Fig. 3.33 repre-

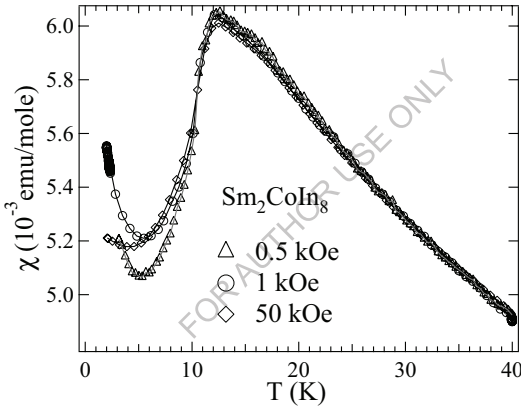


Fig. 3.31: Magnetic susceptibility vs Temperature at various fields for Sm_2CoIn_8 .

sents the fit to the data using equation (3.16). In the absence of crystal field effects, the probable values of μ_{eff} and δ are $0.845 \mu_B$ and 490 K , respectively. The values obtained from the susceptibility fit of Sm_2CoIn_8 are $\mu_{\text{eff}} = 0.8 \mu_B$ and $\delta = 190 \text{ K}$. The difference in the values of δ and μ_{eff} can be attributed to the crystal field effects.

The resistivity behavior of the compound is shown in Fig. 3.34a. The resistivity follows a metallic behavior almost down to the magnetic ordering temperature. The resistivity in the paramagnetic state was fitted to the B-G relation (Eqn. (3.5)), which is shown as the solid line in Fig.

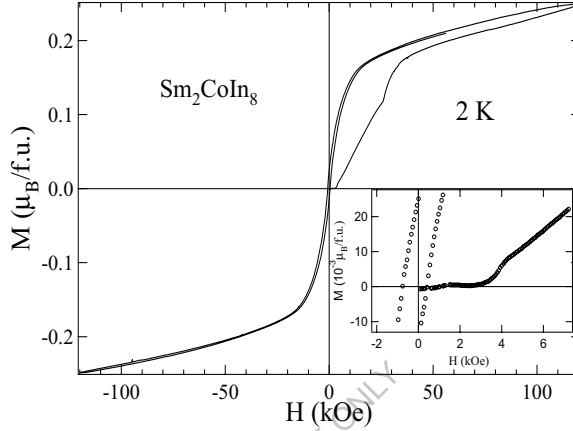


Fig. 3.32: Magnetization Isotherm for Sm_2CoIn_8 at 2 K. Inset shows the expanded version near the low field region.

3.34a. The parameters obtained from the fit are: $\theta_D = 190$ K, $R = 0.13 \mu\Omega\text{-cm}$ and $\rho_0 = 14 \mu\Omega\text{-cm}$. In the ordered state the resistivity data was fitted to Eqn. (3.16) which gave the parameters as $\rho_0^s = 2.5 \mu\Omega\text{-cm}$ and $\Delta = 19$ K. The large value of the energy gap Δ indicates the huge anisotropy

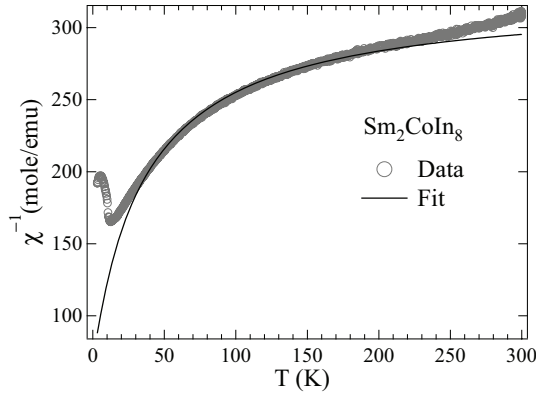


Fig. 3.33: χ^{-1} vs Temperature plot with the fit in the paramagnetic region.

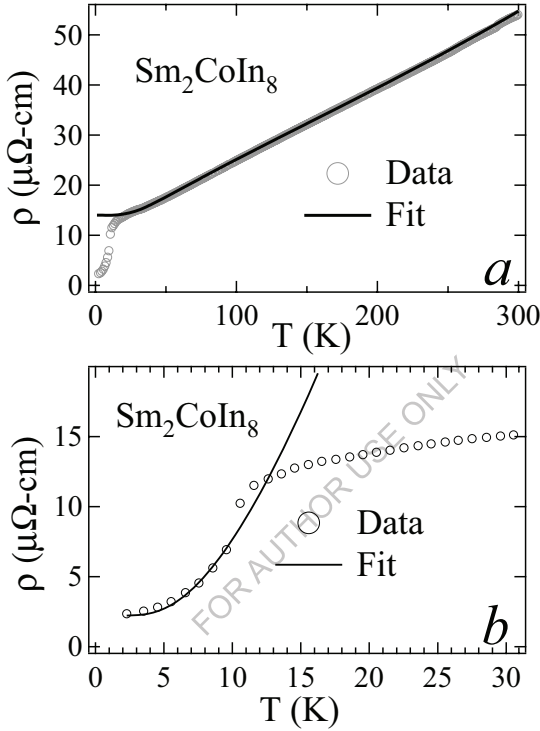


Fig. 3.34: *a*: Resistivity cure for Sm_2CoIn_8 with a B-G fit in the paramagnetic region. *b*: Low temperature ordered state resistivity for the same with a fit to equation (3.16).

of the compound. The magnetoresistance of the compound at 2 K is shown in Fig. 3.35, which shows only a linear increase with the field. This indicates that the dominant interaction in the compound is antiferromagnetic.

The heat capacity behavior of the compound is shown in Fig. 3.36 for various applied fields. The curves show an anomaly only at the antiferromagnetic transition temperature of the compound (≈ 12 K) and no anomaly at low temperatures corresponding to the sudden increase in the magnetic susceptibility. The heat capacity in the presence of magnetic field shows no shift in

the peak temperature with the field. Even the height of the peak also remains approximately the same. Hence we can assume that there is a strong antiferromagnetic interaction present in the

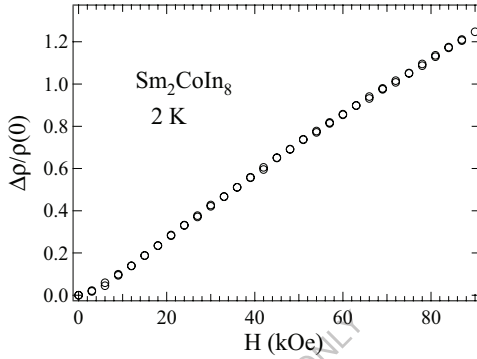


Fig. 3.35: Magnetoresistance for Sm_2CoIn_8 at 2 K.

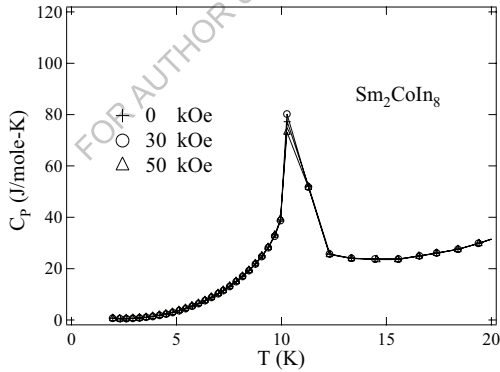


Fig. 3.36: Low temperature Heat capacity for Sm_2CoIn_8 at various fields.

compound.

The upturn of the susceptibility below 5 K and the increase in susceptibility (Fig. 3.31) with field (from 0.5 kOe to 1 kOe) can be attributed to the presence of a ferromagnetic component due to the incomplete cancellation of the antiferromagnetically ordered spins. The virgin curve of the

magnetic isotherm at low fields (below 5 kOe) shows nearly zero magnetization (inset of Fig. 3.32). The exact reason for this behavior is not known but a possibility can be attributed to the anisotropic behavior of the ferromagnetic component. Above 5 kOe the magnetization curve shows a straight line followed by metamagnetic transition at ≈ 26 kOe, which may be due to the spin reorientation. The magnetization curve does not follow the same path when the field is decreased, but shows a curve similar to that of a ferromagnetic compound. The magnetoresistance at 2 K increases monotonically with field, as expected for a pure antiferromagnet. The heat capacity at 50 kOe has exactly similar behavior to that of a zero field one. Considering these behaviors, we suggest that the metamagnetic transition induces a small ferromagnetic component in the compound which dominates the magnetization behavior; otherwise the compound has a dominating strong antiferromagnetic behavior. The hysteretic behavior in the compound is due to the strong anisotropic behavior of the Sm^{3+} ions. The Sm^{3+} ions are well known for strong anisotropic behavior in the ferromagnetic compounds [28].

3.3.2.5 Tb_2CoIn_8

Low temperature susceptibility vs temperature-curve for Tb_2CoIn_8 at various fields (0.5 kOe, 5 kOe, 60 kOe and 90 kOe) is shown in Fig. 3.37. The low field susceptibility shows two

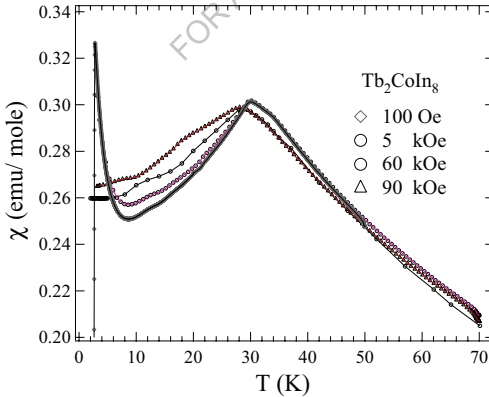


Fig. 3.37: Susceptibility vs Temperature at various fields for Tb_2CoIn_8

magnetic transitions at ≈ 30 K and ≈ 2.5 K, respectively. The transition at 30 K seems to be antiferromagnetic in nature. The susceptibility at low temperatures shows an increase first and then at ≈ 2.5 K falls sharply. If we take the increase in susceptibility due to the development of a ferromagnetic component, then the sudden fall may indicate the onset of a spin-flip transition back to the AFM state. In order to trace the origin of both the transitions, the susceptibility was measured as a function of temperature at various fields, which is also shown in Fig. 3.37. The transition at 2.5 K disappears but the susceptibility still rises for 5 kOe. Both for 60 kOe and 90 kOe, the susceptibility shows only one magnetic transition, but the peak temperature shifts towards low temperatures. This indicates an antiferromagnetic nature of the magnetic ordering. The important feature note is that the susceptibility does not show a smooth variation below the magnetic ordering for all the applied fields. In order to further investigate the magnetization behavior, the magnetization as a function of field was measured at 2 K, which is shown in Fig. 3.38. The curve starts with a linear behaviour, but shows the first metamagnetic transition at ≈ 3 kOe. As the field is increased further, there are other metamagnetic transitions type discontinuities between 40 and 85 kOe and the last one at ≈ 93 kOe. The first metamagnetic transition at 3 kOe may be due to a spin reorientation and may be responsible for the second magnetic transition at 2.5 K observed in the low field magnetic susceptibility. Since only Tb is magnetic in this compound and it is well known for various types of magnetic structures, the observed magnetic properties can be attributed to the possibility of complex magnetic structures in this compound.

The specific heat behavior of the compound at various fields is shown in Fig 3.39. The curves show an anomaly at the transition temperature of the compound. The transition temperature shifts towards low temperatures with field indicating the antiferromagnetic behavior of the compound. Even though the HC curve has a smooth variation below the transition temperature unlike the magnetic susceptibility, a nearly linear behavior is observed at low temperatures instead of a T^3 behavior. To look at the exact nature of the HC curve below T_N , the curve was re-plotted as C/T vs T which is shown as the inset of Fig 3.39. The curve shows a broad hump in the temperature range from 5 to 15 K. It is very difficult to make out whether there is any anomaly corresponding to the discontinuity in the magnetic susceptibility at ≈ 2.5 K. The broad hump might be a characteristic of a Schottky type anomaly. The calculated magnetic entropy comes out to be ≈ 21.8 J/mole-K-Tb, a little higher than that expected for free Tb^{3+} ion (21.3 J/mole-K).

The low temperature resistivity of the compound is shown in Fig 3.40. It shows a deviation at ≈ 30 K due to the antiferromagnetic ordering of the compound. In the ordered state the re-

sistivity shows a little elongated hump and deviation below 3 K. The magnetoresistance is positive, as shown in the inset of Fig. 3.40, indicating an antiferromagnetic behavior of the compound. The magnetoresistance has a huge value in this compound, the origin of which is not clear at present.

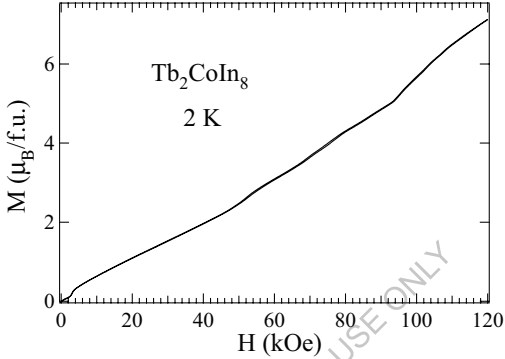


Fig. 3.38: Magnetization Isotherm at 2 K for Tb_2CoIn_8 .

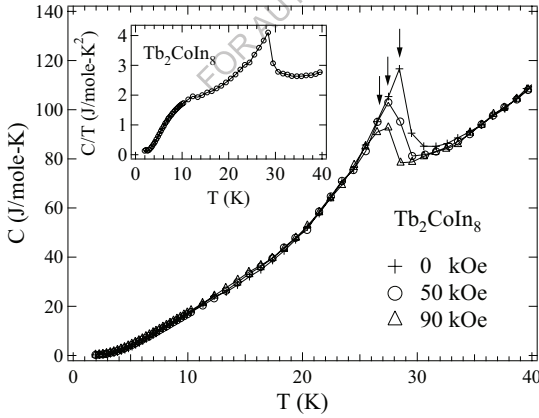


Fig. 3.39: Low temperature HC curve at various fields for Tb_2CoIn_8 .

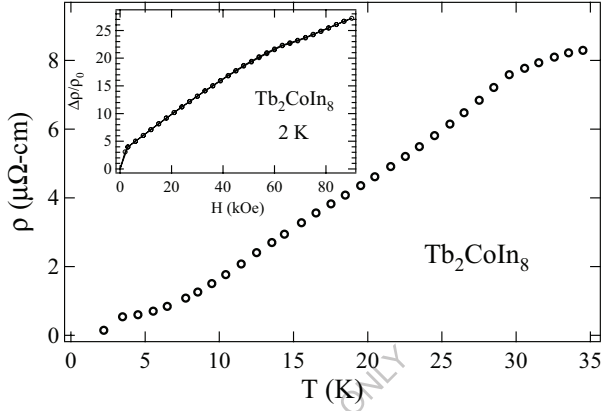


Fig. 3.40: Low temperature resistivity of Tb_2CoIn_8 . Inset shows the magnetoresistance for Tb_2CoIn_8 at 2 K.

3.4 Summary:

In conclusion we have studied the magnetic properties of the $R_2\text{CoIn}_8$ series of compounds. Y_2CoIn_8 shows a Pauli-paramagnetic behaviour indicating a non-magnetic behavior for Co in these compounds. Ce_2CoIn_8 shows a heavy fermion behavior at low temperatures and a Kondo effect at high temperatures. Pr_2CoIn_8 shows a crystal field effect at low temperatures. The other magnetic rare earths ($R = \text{Sm}, \text{Nd}, \text{Gd}, \text{Tb}, \text{Dy}$ and Ho) show antiferromagnetic ordering at low temperatures with $T_N = 12, 10.5, 33.6, 30, 17.5$ and 7.6 K, respectively. Dy_2CoIn_8 shows spin reorientation at low temperature and metamagnetic transitions in the magnetic isotherms. It shows a field induced ferromagnetic state at 2 K and above ≈ 82 kOe. Ho_2CoIn_8 also shows metamagnetic transitions and a field induced ferromagnetic transition at 2 K and above ≈ 54 kOe. Gd_2CoIn_8 is a strong antiferromagnet. Sm_2CoIn_8 shows a dominating antiferromagnetic behavior with a ferromagnetic component at low temperatures. The hysteresis curve above the metamagnetic transition behaves as an anisotropic ferromagnet even if the field is reduced to zero. Tb_2CoIn_8 shows a spin reorientation/ ferromagnetic component at low temperatures and metamagnetic transitions in the magnetic isotherms. It also shows a possibility of complicated magnetic structure below the transition temperature.

3.5 References

1. H.R. Ott, *Prog. Low Temp. Phys.* **11** (1987) 215
2. B. Andraka; C.S. Jee; J.S. Kim,; H. Li; M.W.Meisel and G.R. Stewart, *Physica B*, **171** (1991) 384.
3. J.D. Thompson, *Transport and Thermal Properties of f electron systems* (Plenum Press NewYork 1993)
4. H. Lustfield and A. Bringer, *Solid State Comm.* **28** (1978) 119
5. Ya.M. Kalychak, V.I. Zeremba, V.M. Baranyak, V.A. Bruskov and P.Yu. Zavalij, *Izv. Acad. Nauk SSSR Metall* **1** (1989) 209.
6. Ya.M. Kalychak, *J. Alloys Compd.* **291** (1999) 80.
7. E.G. Moshopolou, Z. Fisk, J.L. Sarrao and J.D. Thompson, *J. Solid State Chem.* **158** (2001) 25
8. H. Hegger, C. Petrovic, E.G. Moshopolou, M.F. Hundley, J.L. Sarrao, Z. Fisk and J.D. Thompson, *Phys.Rev. Lett.* **84** (2000) 4986
9. J.D. Thompson, R. Movshovich, Z. Fisk, F. Bouquet, N.J. Curro, R.A. Fisher and P.C. Hammel, *J. Magn. Magn. Mater.* **226** (2001) 5.
10. C. Petrovic, P.G. Pagliuso, M.F. Hundley, R. Movshovich, J.L. Sarrao, J.D. Thompson, Z. Fisk and P. Monthoux, *J. Phys.: Condens. Matter* **13** (2001) L337.
11. H. Shishido, R. Settai, D. Aoki, S. Ikeda, H. Nakawaki, N. Nakamura, T. Iizuka and Y. Inada *J. Phys. Soc. Jpn.* **71** (2002) 162.
12. M. Nicklas, V.A. Shidorov, H.A. Borges, P.G. Pagliuso, M.F. Hundley, J.L. Sarrao and J.D.Thompson, *cond-mat/0204064*.
13. J.S. Kim, J. Alwood, G.R. Stewart, J.L. Sarrao and J.D. Thompson, *Phys. Rev. B* **64** (2001) 134524.
14. C. Petrovic, R. Movshovich, M. Jaime, P.G. Pagliuso, M.F. Hundley, J.L. Sarrao, J.D. Thompson and Z. Fisk: *Europhys. Lett.* **53** (2001) 354.
15. G. Chen, S. Ohara, M. Hedo, Y. Uwatoko, K. Saito, M. Sorai and I. Sakamoto, *J. Phys. Soc. Jap.* **71** (2002) 2836.
16. G. Chen, S. Ohara, M. Hedo, Y. Uwatoko and I. Sakamoto, *J. Phys.: Condens. Matter* **15** (2003) S2175.

17. H. Hegger, C. Petrovic, E.G. Moshopoulou, M.F. Hundley, J.L. Sarrao, Z. Fisk and J.D. Thompson, *Phys. Rev. Lett.* **84** (2001) 4986.
18. V.T. Rajan, *Phys. Rev. Lett.* **51** (1983) 803.
19. K.H.J. Buschow, *J. Chem. Phys.* **50** (1969) 137.
20. J. Mrachkov and E. Leyarovski, *Physica B* **154** (1988) 66.
21. B. Bleaney, *Proc. Roy. Soc.* **A276** (1963) 19.
22. P. Schlottmann, *Phys. Rep.*, **181** (1989) 1
23. N. D. Mathur, F. M. Grosche, S. R. Julian, I. R. Walker, D. M. Freye, R. K. W. Haselwimmer and G. G. Lonzarich, *Nature* **394** (1998) 39
24. J. Kondo, *Prog. Theor. Phys. Jpn.* **32** (1964) 37.
25. M.B. Fontes, J.C. Troches, B. Giordanengo, S.L. Bud'ko, D.R. Sanches and E.M. Baggio-Saitovitch, *Phys. Rev. B* **60** (1999) 6781 and references their in.
26. Devang A. Joshi, C. V. Tomy, R. Nagarajan, R. Nirmala, S. K. Malik, *J. Appl. Phys.* **97** (2005) 10A920.
27. H.C. Hamakar, L.D. Wolf, H.B. Mackey, Z. Fisk and M.B. Maple, *Solid State Comm.*, **32** (1979) 289.
28. K.H.J. Buschow, *Rep. Prog. Phys.*, **54** (1991) 1123

Chapter 4

Magnetic Properties of Ternary Gallides RNi_4Ga (R = rare earths)

4.1 Introduction

RNi_5 compounds exhibit many interesting properties and are investigated both for practical applications and fundamental studies. $LaNi_5$ is one of the best candidates for hydrogen absorption [1] and $PrNi_5$ is used in the upper stage of the nuclear adiabatic demagnetization device to achieve micro Kelvin temperatures (27 μ K) [2]. $SmNi_5$ is studied for permanent magnet applications by the substitution of Co and Fe for Ni [3]. Compounds with R = Nd, Sm, Tb, Dy, Ho, Er and Tm undergo ferromagnetic transition at low temperatures [4]. The magnetic order in $TbNi_5$ is found to exhibit a helical structure in the temperature range 17–23 K [5]. $LuNi_5$ and $LaNi_5$ are found to be Pauli paramagnets and hence it is deduced that Ni does not have any magnetic moment in RNi_5 compounds [4]. However, it is found that the magnetic ordering of the rare earths can induce a magnetic moment on Ni, even though it is negligibly small compared to that on the magnetic rare earth [6].

Various substitutional studies have been carried out at the Ni site using both magnetic and non magnetic elements [7, 8, 9, 10]. It is found that when Ni is substituted by magnetic elements like Mn, Fe, or Co, the substituted elements order magnetically first at a much higher temperature and in turn increase the overall T_c of the compound to that value. [e.g., for $HoNi_5$, $T_c = 20.5$ K, for $HoNi_4Fe$, $T_c = 110$ K]. However, when the non magnetic elements like B or Al is substituted for Ni, generally the T_c decreases (e.g., for $HoNi_4B$, $T_c = 6$ K) [9], but shows many interesting effects; e.g., $SmNi_4B$ has a higher T_c than $GdNi_4B$ [9]. In $TbNi_{5-x}Al_x$, T_c increases initially (upto $x = 1$) and then decreases with x . The anisotropic behavior of the compound [11] increases, but the helical behavior gets suppressed. $SmNi_4B$ shows high coercivity at low temperatures [12]. In all the cases (both magnetic and non magnetic substitutions), Ni still remains nonmagnetic.

The interesting properties exhibited by RNi_5 compounds when Ni is substituted with non-magnetic elements, prompted us to investigate further by substituting another nonmagnetic element Ga at the Ni site. Only the Ce compound in this series is reported [13], which shows a valence fluctuation behaviour. Hence we have not included the studies on $CeNi_4Ga$ in this thesis.

4.2 Sample Preparation and Crystal Structure

Polycrystalline samples of the series $R\text{Ni}_4\text{Ga}$ ($R = \text{La, Pr, Nd, Sm, Gd, Tb, Dy, Ho, Er, Tm}$ and Lu) were prepared by repeated arc melting of the stoichiometric amounts of the constituent elements on a water cooled cooper hearth in a purified argon atmosphere. The buttons were flipped and melted, repeating the process several times to ensure the homogeneity of the samples. Titanium getter was used as an oxygen absorber. The starting materials were rare earth elements (99.95%), Ni (99.5%) and Ga (99.99%) purity. Because of the volatile nature of Ga, a small amount of extra Ga was added to compensate for the loss during melting. The total weight loss during the arc melting was less than 0.5% and hence the alloy compositions were assumed to re-

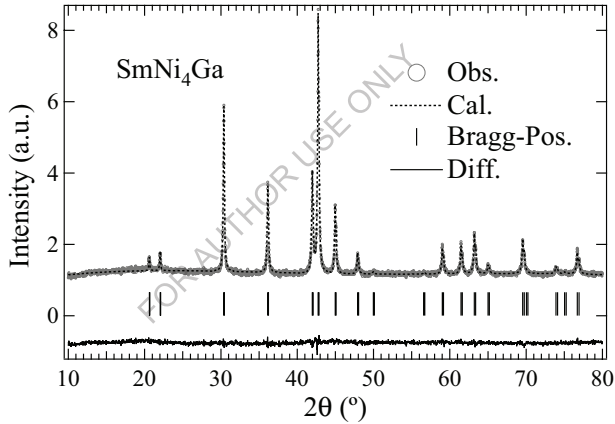


Fig. 4.1: Rietveld refinement of X-ray pattern of SmNi_4Ga showing the experimental, calculated and their difference curve along with the Bragg

main unchanged from the original stoichiometric ratios. The as-melted buttons were wrapped in Tantalum foil, sealed in an evacuated quartz tube and annealed at 800 °C for 15 days. The compound YbNi_4Ga did not form in single phase by the method described, may be due to the high volatile nature of Yb and the Eu compound was not tried at all. The compounds formed are brittle by nature. By comparing the cross-sections of the same sample before and after annealing, it was found that the annealed samples had developed more cracks compared to that of the as melted samples. The increase in the width of the cracks with annealing of the compound also indicates

the high brittleness of the compounds. The room temperature powder X-ray diffraction patterns

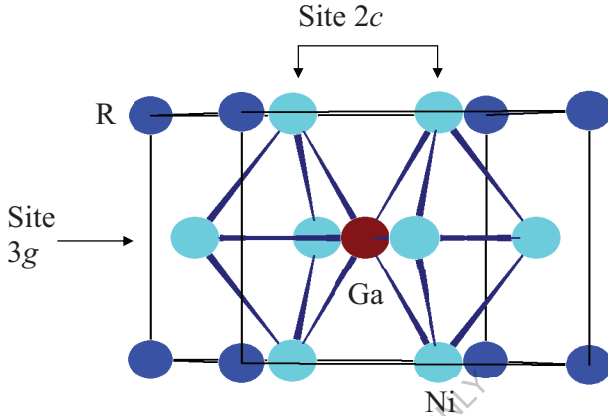


Fig. 4.2: Crystal structure of RNi_4Ga compound with a $1/3$ hexagonal unit cell. The crystallographic sites, $2c$ and $3g$ ($z = 1/2$ plane) are indicated by arrows. The corners represent the crystallographic site $1a$.

of the samples were obtained using a Panalytical X-ray diffractometer equipped with Cu- K_α radiation. The X-ray patterns of the samples before and after the annealing were compared. It was found that the pattern remained the same except that the intensity of the diffraction lines increased for the annealed ones under similar X-ray exposure times. This indicates that, annealing has improved the homogeneity of the sample. The formation of the compounds in the as melted state indicates a good solubility of Ga_x in RNi_{5-x} samples for $x = 1$. The samples do not form readily for $x = 2$, which were confirmed by preparing $DyNi_3Ga_2$ where the compound formed only after prolonged annealing. This indicates that the solubility decreases with increasing Ga concentration in $RNi_{5-x}Ga_x$ compounds.

In order to obtain the structure type and the lattice parameters, a Rietveld refinement (FullProf program) of the obtained XRD pattern was carried out for all the compounds. The Rietveld refinement of the X-ray pattern of a typical compound, $SmNi_4Ga$, is shown in Fig. 4.1. To start with, the lattice parameters and space group of the parent compound were given as the input to the fitting program. It was found that all the RNi_4Ga series of compounds form in the $CaCu_5$ type hexagonal structure with a space group $P6/mmm$, maintaining the structure of the parent

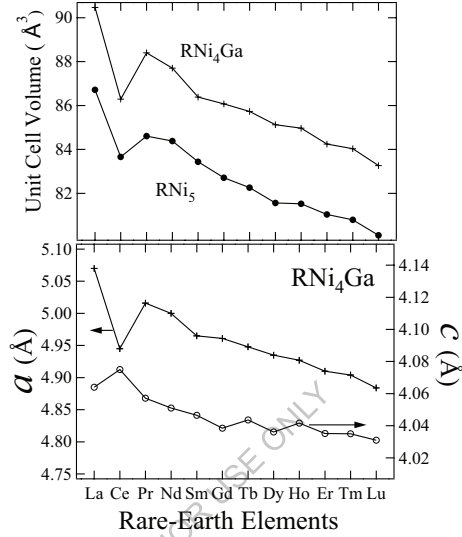


Fig. 4.3: Variation of the unit cell volume (upper panel) and lattice parameters a and c (lower panel) for the rare earth series.

compound. The crystallographic parameters obtained from the best fit of the X-ray patterns are given in Table 4.1.

Figure 4.2 shows the hexagonal crystal structure (1/3 of the unit cell) of the Ga substituted parent RNi_5 compounds. Rare earths occupy the corners, crystallographically referred to as $2a$ site for a hexagonal structure. In the parent RNi_5 compounds, Ni atoms can occupy two different crystallographic sites, (i) $2c$ sites with an occupancy of two, located in the $z = 0$ planes where the R atoms are also located and (ii) $3g$ sites with an occupancy of three, located in the $z = \frac{1}{2}$ plane. However, in the Ga substituted compounds, the refinement of the X-ray pattern gives the best fit of the experimental data (see the difference plot in Fig. 4.1) when Ga is considered occupying only the $3g$ site with an occupancy of one. It is quite possible that Ga gets substituted only at the $3g$ site in order to retain the structure, because of the absence of R atoms in this plane which allows a larger Ni-Ga distance compared to that of the $2c$ site.

Table 4.1: Crystallographic parameters for $R\text{Ni}_4\text{Ga}$ compounds. The occupancy is compared with the corresponding parent compound $R\text{Ni}_5$.

| Atom | Site Symmetry | x | y | z | $U_{eq}(\text{\AA}^2)$ | Occupancy | |
|------|---------------|-------|-------|------|------------------------|----------------|-------------------------|
| | | | | | | $R\text{Ni}_5$ | $R\text{Ni}_4\text{Ga}$ |
| R | 1a | 0.00 | 0.00 | 0.00 | 0.068 | 1 | 1 |
| Ni | 2c | 0.333 | 0.666 | 0.00 | 0.045 | 2 | 2 |
| Ni | 3g | 0.50 | 0.00 | 0.50 | 0.052 | 3 | 2 |
| Ga | 3g | 0.50 | 0.00 | 0.50 | 0.023 | - | 1 |

The lattice parameters and the unit cell volume of $R\text{Ni}_4\text{Ga}$ compounds are listed in Table 4.2 along with the corresponding parameters for $R\text{Ni}_5$ [4] compounds for comparison. The lattice parameters and the unit cell volume of $R\text{Ni}_4\text{Ga}$ compounds are larger than that of the corresponding parent compounds. The reason for the increase in the lattice parameter can be attributed to the expansion of the unit cell due to the substitution of the larger Ga atom (1.41 Å) in place of the Ni atom (1.24 Å). Both the unit cell volume and the lattice parameters show the same trend of lanthanide contraction (Fig. 4.3) as expected for the trivalent rare earth ions, except for Ce because of its mixed valent behavior in both the series [13, 14].

4.3 Results and Discussions

4.3.1 Primary Discussion:

4.3.1.1 Magnetization Measurements

In order to study the magnetic properties of $R\text{Ni}_4\text{Ga}$ compounds, magnetization of the compounds were measured as a function of temperature and magnetic field. The first aim was to verify whether the substitution of Ga at the Ni site, which resulted in the expansion of the lattice, brought about any changes in the magnetic state of Ni, which otherwise is nonmagnetic in $R\text{Ni}_5$ compounds. For this purpose the magnetic properties of nonmagnetic rare earth compounds, LaNi_4Ga and LuNi_4Ga were first measured which are presented in Figure 4.4. The susceptibility does not show any indication of a magnetic ordering (which is confirmed by the heat capacity measurements also) and is nearly temperature independent (Pauli-paramagnetic behavior) except a little upturn at low temperatures. In order to elucidate whether such an upturn in the susceptibil-

ity is due to the development of a moment on Ni or is due to a paramagnetic impurity in the sample, the susceptibility of LaNi_4Ga was fitted to the modified Curie-Weiss Law (Eqn. (3.5)) and is shown as the solid line in Fig. 4.4. The effective moment thus obtained is only $0.08 \mu_B$. Even for this moment value, the paramagnetic susceptibility expected at low temperatures is much higher than that of the observed values. Hence the low temperature upturn can be considered to be arising from some unknown negligible impurity contribution. Thus, the susceptibility of the non magnetic rare earth compounds clearly demonstrate that the substitution of Ga in $R\text{Ni}_5$ compounds keeps the nonmagnetic behavior of Ni intact.

The low temperature part of the susceptibility for compounds with magnetic rare earths are

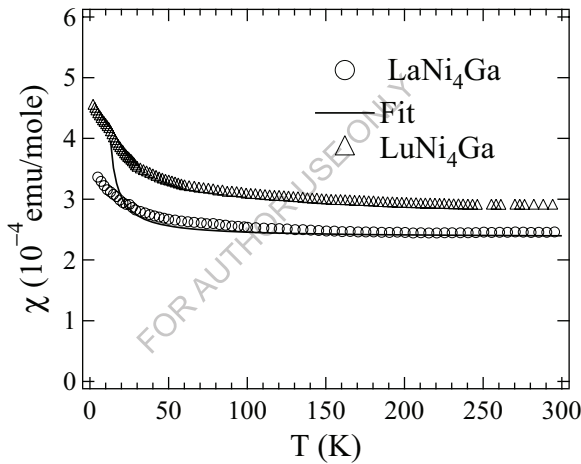


Fig. 4.4: Susceptibility as a function of temperature for the nonmagnetic rare earth compounds, LaNi_4Ga and LuNi_4Ga . Solid line represents a fit to the Curie Weiss equation.

shown in Figs. 4.5, 4.6 and 4.7. The susceptibility of PrNi_4Ga (Fig. 4.5a) shows a pure paramagnetic behaviour without any indication of a magnetic ordering down to 2 K. The magnetic isotherm of the sample at 2 K (Fig. 4.8a) gives a straight line, consistent with the paramagnetic behavior of the sample. The susceptibility of the compounds with other magnetic rare earths $R = \text{Nd}, \text{Sm}, \text{Gd}, \text{Tb}, \text{Dy}, \text{Ho}, \text{Er}$ and Tm shows a peak at low temperatures reminiscent of a magnetic

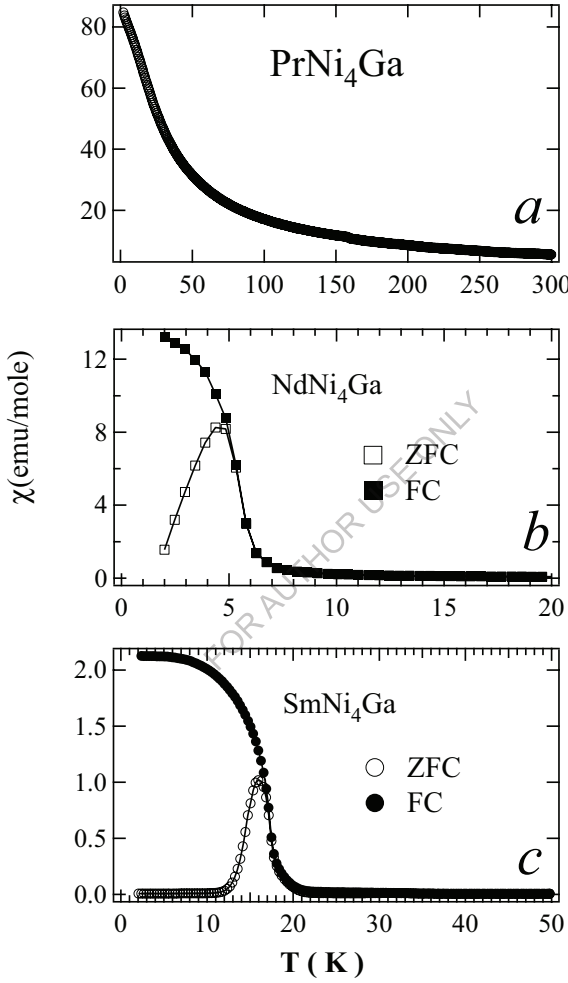


Fig. 4.5: Susceptibility vs Temperature curves under FC and ZFC conditions for $R\text{Ni}_4\text{Ga}$ ($R = \text{Pr}, \text{Nd}$ and Sm) compounds.

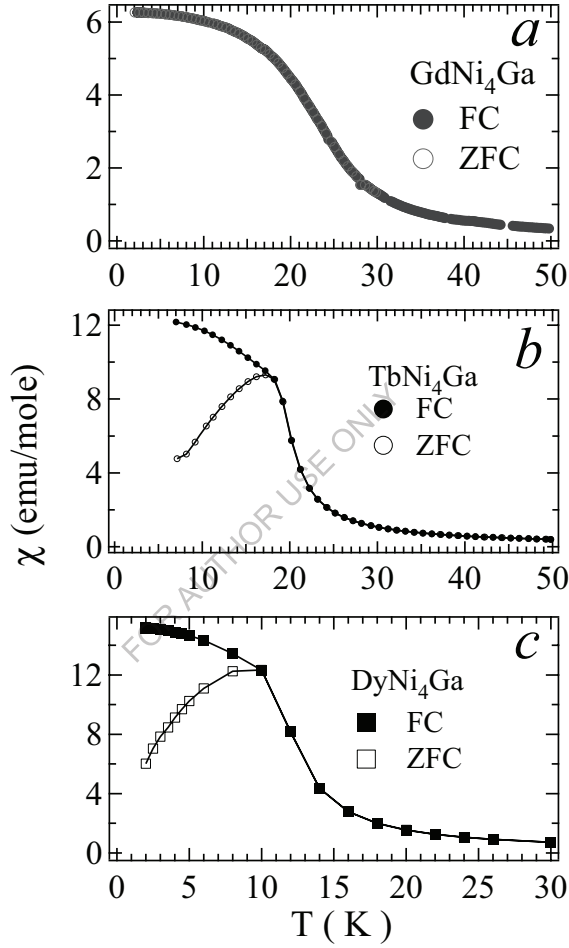


Fig. 4.6: Susceptibility vs Temperature curves under FC and ZFC conditions for $R\text{Ni}_4\text{Ga}$ ($R = \text{Gd}$, Tb and Dy) compounds.

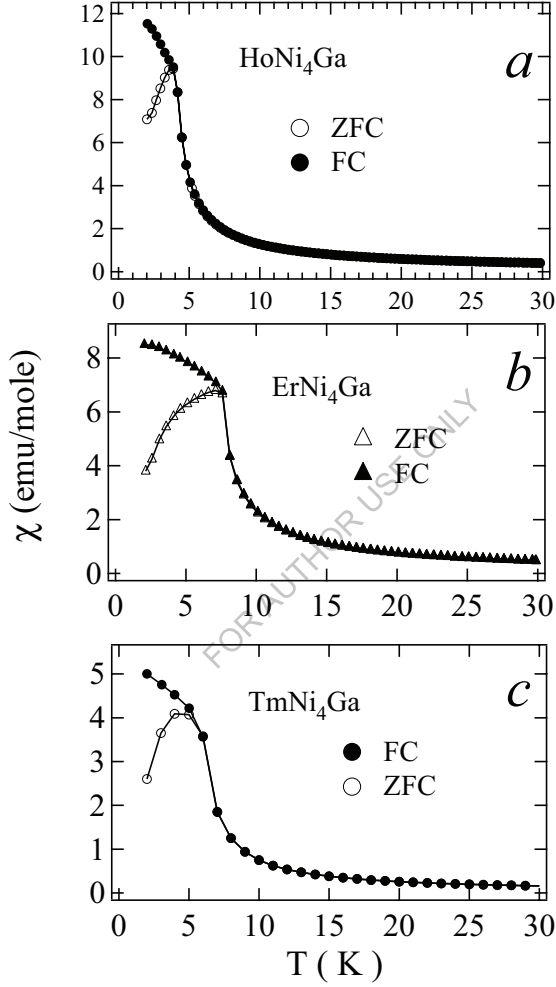


Fig. 4.7: Susceptibility vs Temperature curves under FC and ZFC conditions for $R\text{Ni}_4\text{Ga}$ ($R = \text{Ho}, \text{Er}$ and Tm) compounds.

ordering. To confirm the nature of the ordering, magnetic isotherms were measured at 2 K for all the compounds which are shown in Figs. 4.8 and 4.9. The saturation behavior of the magnetization is typical of a ferromagnetically ordered compound. Hence the magnetic ordering in these compounds can be considered to be of ferromagnetic. The magnetic ordering of the compounds

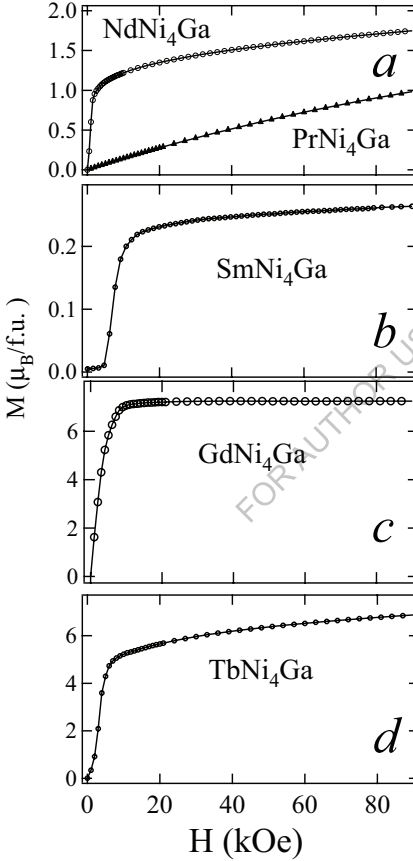


Fig. 4.8: Magnetic Isotherm for $R\text{Ni}_4\text{Ga}$ (Pr, Nd, Sm, Gd and Tb) compounds at 2 K.

was further confirmed by the ac susceptibility measurements, the results of which are shown in Fig. 4.10. The transition temperatures were determined from the peak positions in ac susceptibility which agree well with the dc susceptibility measurements and are given in Table 4.3.

The DC susceptibility of the compounds was measured under zero field cooled (ZFC) and field cooled (FC) conditions. For ZFC measurements, the sample is cooled down to the lowest temperature in the absence of an applied magnetic field, the required field is applied and then the data was taken while the temperature was increased. In FC measurements, the sample is cooled to the lowest temperature in the presence of an applied field from well above the transition temperatures and the data was taken while the temperature was increased. In the magnetically ordered state (below T_c), all the compounds, except GdNi_4Ga , show thermomagnetic hysteresis, which is evident by the separation between the FC and ZFC curves.

The susceptibility measured in the FC state at 500 Oe field increases with decrease in temperature and after a sharp jump at T_C , the susceptibility tends to saturate. For measurements in the ZFC

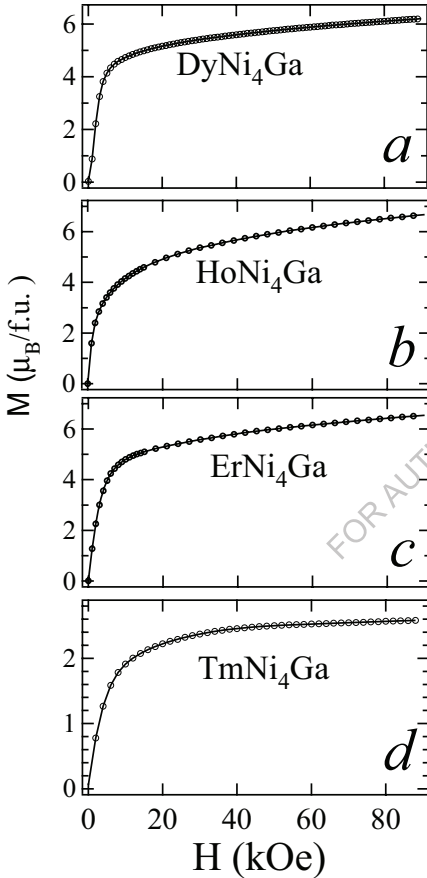


Fig. 4.9: Magnetic Isotherm for RNi_4Ga (Dy, Ho, Sm, Er and Tm) compounds at 2 K.

state, the magnetization follows the same path as that of the FC curves down to the transition temperature, deviates from the FC curve followed by a maximum and then decreases somewhat similar to that of an anti-ferromagnetic type transition. Since the thermomagnetic irreversibility is absent in the Gd compound and considering the fact that the magnetic anisotropy is minimum for Gd due to the absence of total orbital angular momentum, we can effectively presume that the anisotropy of the rare earth ion plays a role in the thermomagnetic irreversibility in the rest of the compounds.

Thermomagnetic irreversibility is well known in Spin-Glass and magnetically frustrated systems. However, such a behavior is observed in anisotropic ferromagnets also. Thermo-magnetic irreversibility in an anisotropic ferromagnetic system can occur, if the alignment of the domains is restricted by an energy barrier (anisotropic energy). So cooling the specimen without the magnetic field will lead to a pinning of the domain walls. The subsequent application of

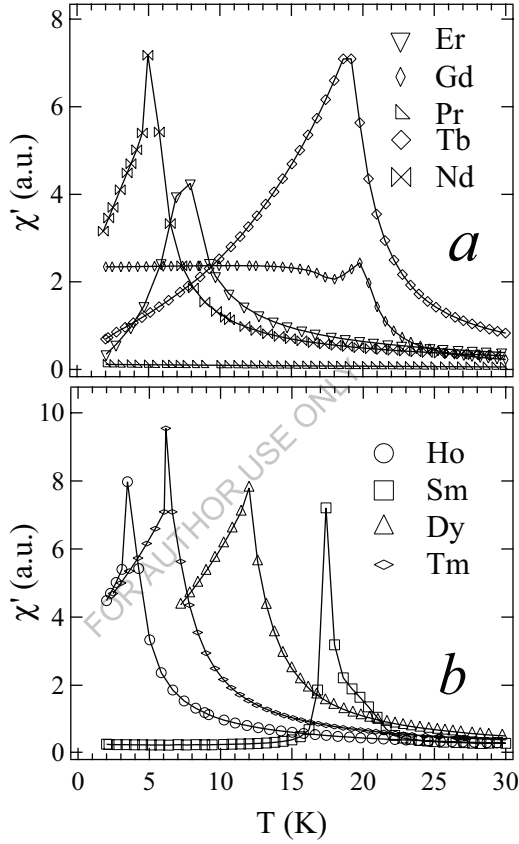


Fig. 4.10: Real part of the AC susceptibility of $R\text{Ni}_4\text{Ga}$ series of compounds. (a): $R = \text{Er, Gd, Pr, Tb and Nd}$. (b): $R = \text{Ho, Sm, Dy and Tm}$.

the magnetic field results in the alignment of some of the domains. The increase in the temperature also helps in overcoming the energy barrier. Hence the magnetization increases initially with temperature up to a temperature near T_c at which a peak occurs. The peak is the resultant of

a competitive process between the applied field and the thermal energy after which the thermal energy dominates and the magnetization decreases. In the FC mode, the presence of an applied field just above the transition temperature helps the alignment of the domains in the direction of field while cooling below T_C . The anisotropic behavior is also confirmed from the typical magnetization values in the low temperature magnetic isotherms. The maximum magnetization ($\mu_B/\text{f.u.}$) achieved for $R = \text{Nd, Sm, Gd, Tb, Dy, Ho, Er}$ and Tm at 2 K and 9 T are 1.76, 0.27, 7.2,

Table 4.2: Comparison of the lattice parameters (a and c) and the unit cell volume of $R\text{Ni}_5$ and $R\text{Ni}_4\text{Ga}$ compounds.

| R | $R\text{Ni}_5$ | | | $R\text{Ni}_4\text{Ga}$ | | |
|-----------|----------------|---------|-----------------------|-------------------------|---------|-----------------------|
| | a (Å) | c (Å) | V (Å ³) | a (Å) | c (Å) | V (Å ³) |
| La | 5.014 | 3.983 | 90.4664 | 5.071 | 4.064 | 86.7155 |
| Ce | 4.878 | 4.06 | 86.2935 | 4.945 | 4.075 | 83.6619 |
| Pr | 4.957 | 3.976 | 88.4014 | 5.016 | 4.057 | 84.6062 |
| Nd | 4.952 | 3.975 | 87.7041 | 5.001 | 4.051 | 84.3803 |
| Sm | 4.924 | 3.974 | 86.3845 | 4.965 | 4.046 | 83.4415 |
| Gd | 4.906 | 3.968 | 86.0749 | 4.961 | 4.038 | 82.7075 |
| Tb | 4.894 | 3.966 | 85.7325 | 4.948 | 4.043 | 82.2619 |
| Dy | 4.872 | 3.968 | 85.1244 | 4.932 | 4.036 | 81.5651 |
| Ho | 4.872 | 3.966 | 84.9662 | 4.929 | 4.041 | 81.5239 |
| Er | 4.858 | 3.965 | 84.2451 | 4.910 | 4.036 | 81.0356 |
| Tm | 4.852 | 3.963 | 84.0354 | 4.904 | 4.035 | 80.7948 |
| Lu | 4.832 | 3.961 | 83.2687 | 4.884 | 4.031 | 80.0897 |

6.9, 6.2, 6.7, 6.5 and 2.6, respectively. These values are much smaller than the theoretical values of the saturation moment expected for the corresponding free R^{3+} moments except for GdNi_4Ga . This deviation can also be attributed to the magnetic anisotropy of the R moments, except for Gd which has got the least anisotropy. The remnant magnetization is negligibly small in all these

compounds except for SmNi_4Ga and TbNi_4Ga (details of these compounds will be discussed in section 4.3.3).

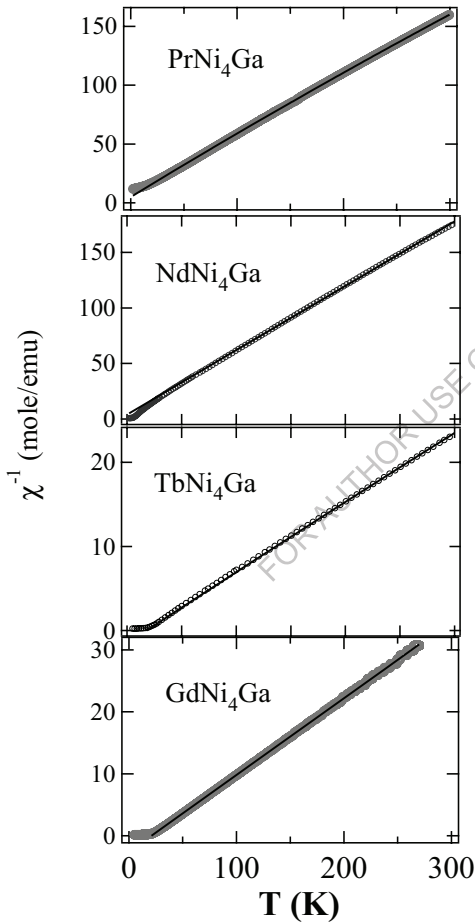


Fig. 4.11: Inverse susceptibility vs Temperature curve for $R\text{Ni}_4\text{Ga}$ (Pr, Nd, Gd and Tb) compounds. The line through the data points represents the Curie-Weiss fit.

The inverse susceptibility in the paramagnetic region is almost a straight line and could be fitted to the Curie-Weiss law (Eqn. (3.2)) except for SmNi_4Ga . The inverse susceptibility and the Curie-Weiss fit for all the compounds are shown in Fig. 4.11 and 4.12. The paramagnetic Curie temperatures and the effective magnetic moments obtained from the fit are given in Table 4.3. The effective paramagnetic moments are close to, but less than, the theoretically expected values for free R^{3+} atoms except for CeNi_4Ga and TmNi_4Ga . In the case of CeNi_4Ga the reason for the smaller effective paramagnetic moment is due to the mixed valent behavior of the compound [13,14]. For TmNi_4Ga , one of the possibilities for the smaller value of the effective moment may be a large crystal field effect in the compound.

The inverse susceptibility of SmNi_4Ga is shown in Fig. 4.13. For SmNi_4Ga , the first excited state of Sm^{3+} lies very close to the ground state ($\Delta E_{7/2-5/2} \approx 1400$ K) and hence the susceptibility in the paramagnetic state does not obey the Curie-Weiss

Law. The data was fitted to the modified Curie-Weiss law [15]

$$\chi = \frac{N_A}{k_B} \left(\frac{\mu_{\text{eff}}^2}{3(T - \theta_p)} + \frac{\mu_B^2}{\delta} \right) \quad (4.1)$$

Here N_A is the Avogadro number, k_B is the Boltzmann's constant, μ_B is the Bohr magneton,

μ_{eff} is the effective magnetic moment, θ_p is the paramagnetic Curie temperature and $\delta = 7\Delta E/20$ where ΔE is the difference between the ground state and the first excited state. For the Sm^{3+} , the first term in the above equation represents a Curie-Weiss contribution from the $J = 5/2$ ground state, while the second term is the temperature independent Van Vleck correction arising from the $J = 7/2$ state, which is the first accessible excited state. In the absence of crystal field effects, the probable values of μ_{eff} and δ are $0.845 \mu_B$ and 490 K , respectively. The values obtained from the fit (shown as solid line in Fig. 4.13) to the susceptibility of SmNi_4Ga are $\mu_{\text{eff}} = 0.81 \mu_B$ and $\delta = 270 \text{ K}$. The smaller value of δ may be attributed to the crystal field effects.

The magnetic ordering temperatures of the $R\text{Ni}_4\text{Ga}$ compounds are found to be less than the corresponding $R\text{Ni}_5$ parent compounds (Table 4.3). Since Ni is nonmagnetic, the ferromagnetic ordering in $R\text{Ni}_5$ compounds occurs due to the

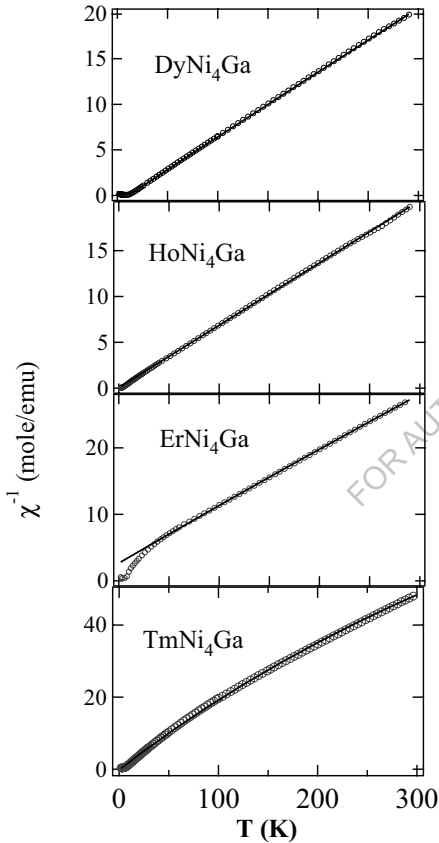


Fig. 4.12: Inverse susceptibility vs Temperature curve for $R\text{Ni}_4\text{Ga}$ (Dy, Ho, Er and Tm) compounds. The line through the data points represent the Curie-Weiss fit.

ordering of only the rare earth ions. The RKKY interaction responsible for the magnetic ordering is mediated by the conduction electron polarization. One of the possible reasons which can be attributed to the decrease in T_C is the increase in the distance between the rare earth ions as evi-

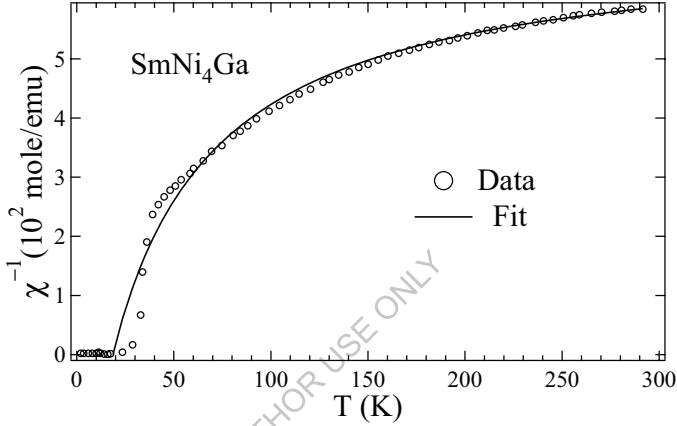


Fig. 4.13: χ^{-1} vs T curve for SmNi₄Ga with a fit to the modified Curie-Weiss equation.

dent from the increase in lattice parameters of the compounds when Ga is substituted for Ni. This reduces the absolute value of the conduction electron polarization responsible for the RKKY interaction. According to the well known de-Gennes scaling, T_C of the isostructural members of the rare earth series is proportional to $(g_J - 1)^2 J(J+1)$, where g_J is the Lande factor and J is the total angular momentum. In the title compounds, this behavior is not closely followed (Fig. 4.14), especially in the case of TbNi₄Ga and SmNi₄Ga where the T_C deviates appreciably from their expected values. Such a behavior is found only in SmNi₅ in the case of the parent compounds and is generally attributed to the crystalline electric field (CEF) effects [16]. It has been shown that the crystal fields of a suitable sign can enhance the ordering temperature of a compound compared to that expected by the de-Gennes scaling [17,18]. Sometimes the T_C can even become larger than that of the corresponding Gd compound as in the case of compounds like TbPdSn [19],

SmNi₄B [20], etc. The other possible reason especially for the Sm compounds is the strong exchange coupling between the 4*f* electrons and the conduction electrons caused by the hybridiza-

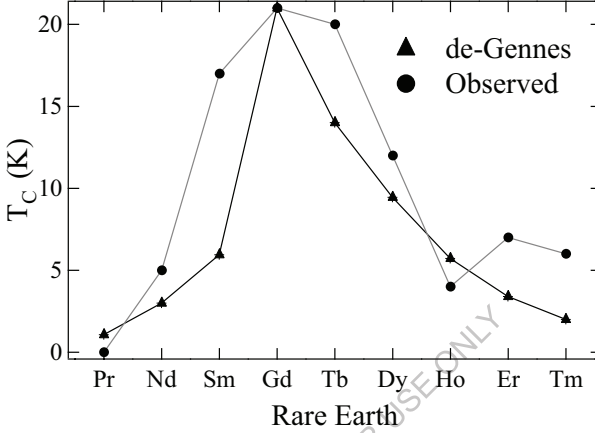


Fig. 4.14: Comparison of the transition temperatures of $R\text{Ni}_4\text{Ga}$ compounds with that of expected from de-Gennes scaling.

tion of the 4*f* state with the conduction electron state [21].

4.3.1.2 Heat Capacity Measurements:

The heat capacity of $R\text{Ni}_4\text{Ga}$ compounds is shown in Fig. 4.15, Fig. 4.16 and Fig. 4.17. The nonmagnetic LaNi_4Ga shows a normal phononic behavior as expected for a non magnetic compound (Fig. 4.15a). The total specific heat of the compound was fitted (shown as solid line in Fig. 4.15a) to the equation,

$$C_{\text{tot}} = C_{\text{elec}} + C_{\text{phonon}} = \gamma T + C_{\text{phonon}} \quad (4.2)$$

The phonon term was calculated using the Debye integral

$$C_{\text{phonon}} = 9NR \left(\frac{T}{\theta_D} \right)^3 \int_0^x \frac{x^4 e^x dx}{(e^x - 1)^2} \quad \text{where } x = \frac{\theta_D}{T} \quad (4.3)$$

The parameters from the fit are $\gamma = 12 \text{ mJ/mole-K}$ and $\theta_D = 292 \text{ K}$. The significance of these parameters will be discussed in detail in the next section. PrNi_4Ga shows a smooth varying specific

Table 4.3: Transition temperature of $R\text{Ni}_5$ [4] and $R\text{Ni}_4\text{Ga}$ series of compounds. Paramagnetic Curie temperature (θ_p), effective magnetic moment (μ_{eff}) and saturation moment (μ_{sat}) for $R\text{Ni}_4\text{Ga}$ compounds are also listed.

| R | $R\text{Ni}_5$ | | $R\text{Ni}_4\text{Ga}$ | | | |
|-----|----------------|-----------|-------------------------|--------------------------------|--------------------------------|---|
| | T_C (K) | T_C (K) | θ_p (K) | μ_{eff} (μ_B) | μ_{sat} (μ_B) | μ_{sat} (μ_B) (theory) |
| La | P-P | P-P | - | - | 0 | 0 |
| Ce | P | P | -35 | 0.8 | 0.8 | 2.14 |
| Pr | P | P | -9 | 3.57 | 1.0 | 3.2 |
| Nd | 13 | 5 | 0 | 3.6 | 1.76 | 3.28 |
| Sm | 27.5 | 17 | 15 | 0.81 | 0.27 | 0.72 |
| Gd | 29.3 | 20 | 20.5 | 7.9 | 7.24 | 7 |
| Tb | 27 | 19 | 19 | 9.7 | 6.9 | 9 |
| Dy | 20 | 12 | 11 | 10.6 | 6.2 | 10 |
| Ho | 20.5 | 3.5 | 2.3 | 10.6 | 6.7 | 10 |
| Er | 12 | 8 | 9.5 | 9.6 | 6.5 | 9 |
| Tm | 11 | 6.5 | 5 | 7 | 2.6 | 7 |
| Lu | P-P | P-P | - | - | 0 | 0 |

P-P: Pauli-paramagnet,

P: Paramagnet

heat curve typical for a paramagnetic compound (Fig. 4.15b). This supports our magnetic measurement results. Compounds with magnetic rare earths like $R = \text{Sm}, \text{Gd}, \text{Tb}, \text{Dy}, \text{Er}$ and Tm show a sharp anomaly at their respective ferromagnetic ordering temperatures. In case of GdNi_4Ga and TbNi_4Ga , there are small hump-like characteristics below the magnetic ordering temperatures, as indicated by arrows (Fig. 4.16). At low temperatures, the transition among the various crystal field states can give rise to such humps. In case of TbNi_4Ga (Fig. 4.16b) and DyNi_4Ga (Fig. 4.17a), the peak at the transition temperature is broadened (compared to lambda type peaks for other compounds). The broadening may also be due to the dominant crystal field effects. The details along with the AC susceptibility and magnetization measurements are discussed in the next sections.

4.3.2 Detailed Discussion for GdNi_4Ga and LaNi_4Ga :

The magnetic properties of GdNi_4Ga compound is of special interest due to the absence of anisotropy for Gd^{3+} atom. This helps us to retrieve the information regarding the magnetic properties of other constituent elements. We will discuss the magnetic properties of GdNi_4Ga using the data obtained from magnetization, specific heat and AC susceptibility measurements. Results

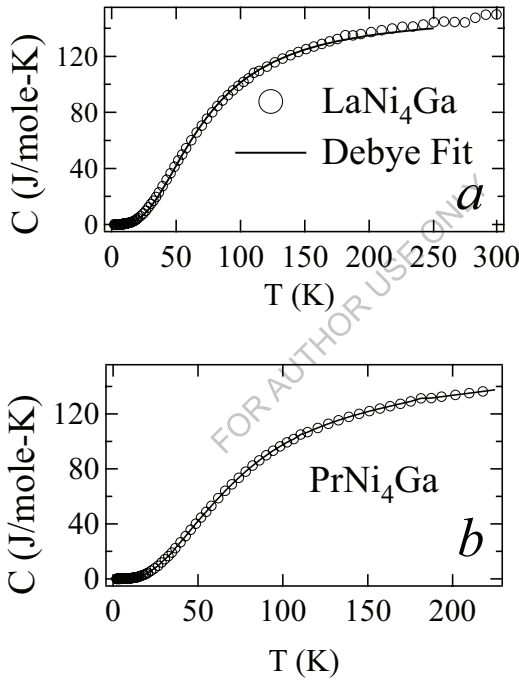


Fig. 4.15 : Heat capacity curves for LaNi_4Ga and PrNi_4Ga . LaNi_4Ga curve is fitted to the sum of electronic and phonon contributions.

of LaNi_4Ga are given to support some of the analysis/discussions.

Figure 4.18 shows the real part of the AC susceptibility for GdNi_4Ga in zero and 5 kOe applied DC magnetic fields. In zero DC field, the real part shows a peak at T_c followed by a mini

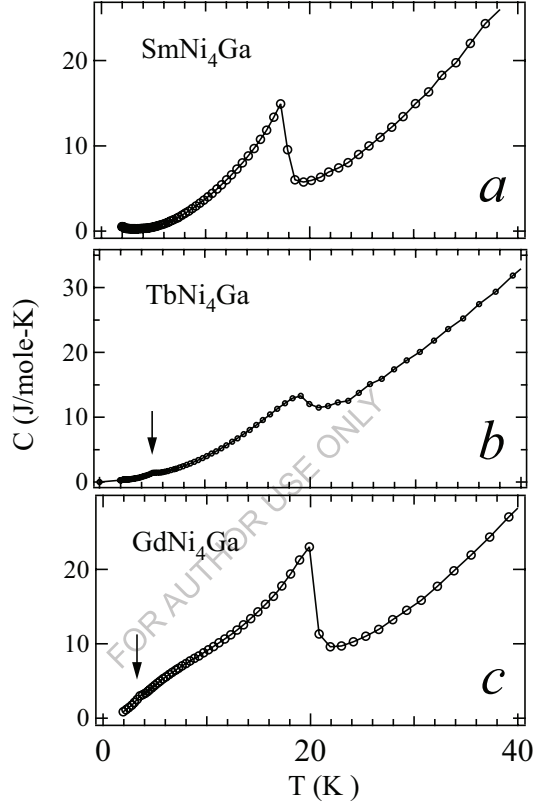


Fig. 4.16 : Heat capacity curves for $R\text{Ni}_4\text{Ga}$ (Sm, Tb and Gd) compounds. Sm and Tb compounds show low temperature anomalies in addition to the one at transition temperature.

mum at ≈ 18 K and then rises and remains almost constant, uncharacteristic of typical FM ordering. The imaginary part (inset of Fig. 4.18) shows only one peak at ≈ 18 K. Schottky type anomalies are also observed at low temperatures (below T_c , at ≈ 6 K and 3 K) in the specific heat of the compound. These anomalies are seen more prominent in C/T vs T curve, as shown in Fig. 4.19.

Usually such anomalies in heat capacity at low temperatures are attributed to the crystal field effects, which split the ground state. In GdNi_4Ga , Ni is non magnetic (as discussed below) and hence the magnetism arises only due to Gd^{3+} . Since the orbital angular momentum for Gd^{3+} is

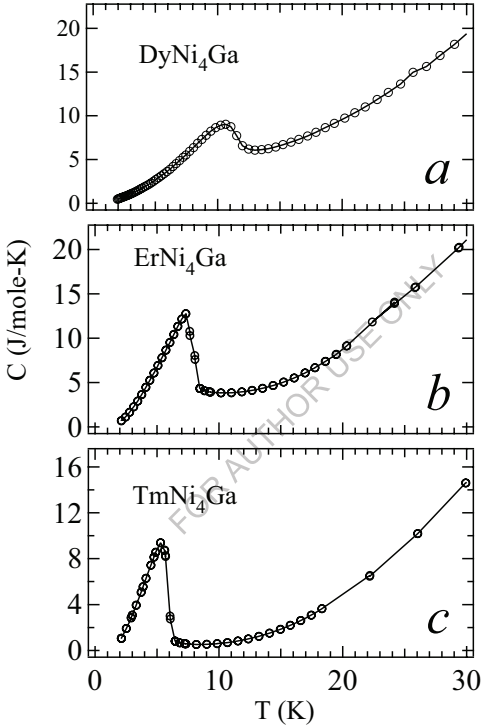


Fig. 4.17 : Heat capacity curves for $R\text{Ni}_4\text{Ga}$ (Dy, Er and Tm) compounds. Anomalies are seen only at transition temperature.

zero, we rule out the possibility of crystal field effects in GdNi_4Ga . Similar anomalies in AC susceptibilities are also reported in Gd metal [22]. In the absence of the usual crystal field effects,

the reason for such anomalies was attributed to the formation of a helical structure of the spins in

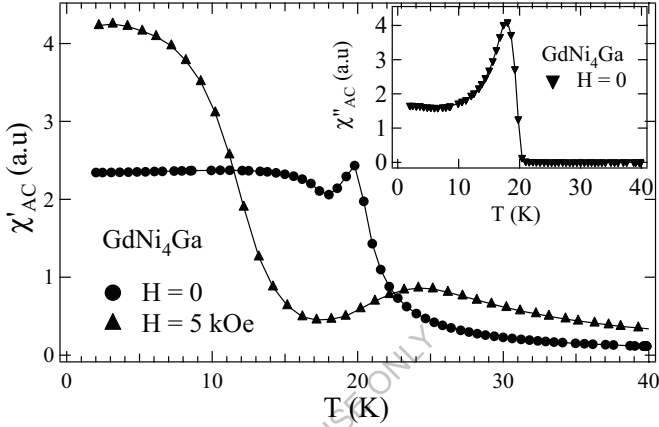


Fig. 4.18: Real part of the AC susceptibility of GdNi₄Ga with a DC field of 0 and 5 kOe. Imaginary part of the susceptibility is shown as the inset.

the ordered state. According to Sandratskii *et al* [23], an exchange type helix forms if the magnetic anisotropy is much weaker compared to the exchange interaction. In case of GdNi₄Ga, the magnetic anisotropy is much weaker (only the second order anisotropy arises from the interaction of magnetic dipoles associated with the spins) than the inter-atomic exchange interaction. Considering this, GdNi₄Ga can be presumed to have a helical structure in the ordered state. There is no indication of any magnetic transition at low temperature, since the imaginary part of the ac susceptibility decreases smoothly below the transition temperature (inset of Fig. 4.18). The humps in the specific heat behavior may be a consequence of the helical structure due to which the rearrangement of spins within the ordered state can occur as a function of temperature. Real part of the AC susceptibility with a DC field of 5 kOe is also shown in Fig. 4.18. The peak at T_c gets broadened and shifts towards higher temperatures. At low temperatures the susceptibility rises indicating a magnetic transition. The shifting of the peak towards high temperatures indicates a dominating ferromagnetic component in the ordered state. The increase of susceptibility at

low temperatures may be due the transition from a helimagnetic to a pure ferromagnetic state. A ferromagnetic state at high fields and low temperatures is confirmed as discussed below.

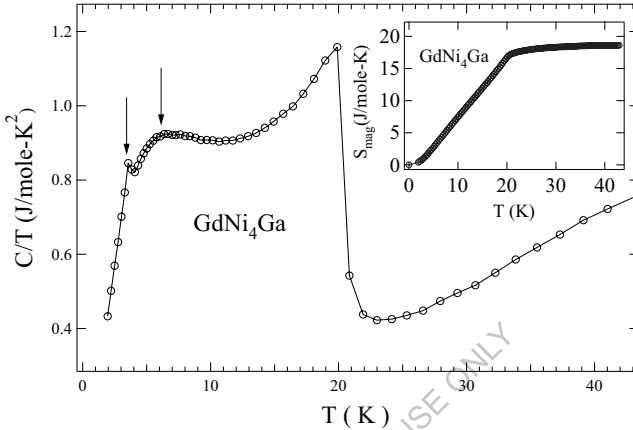


Fig. 4.19: C/T vs T curve for GdNi_4Ga indicating two additional anomalies below the transition temperature. Magnetic entropy is shown as the inset.

For GdNi_4Ga , the saturation magnetization obtained at 2 K and 9 T is $7.25 \mu_B/\text{f.u.}$ (Fig. 4.8c) which is higher than that expected for the free Gd^{3+} ion ($7.0 \mu_B/\text{f.u.}$). This supports our explanation of minimum anisotropy in GdNi_4Ga (full saturation moment) and an anisotropic behavior in other rare earth compounds (smaller values of saturation moments). The saturation moment reported for GdNi_5 is $6.8 \mu_B/\text{f.u.}$ and for a structurally related GdNi_4B is $7.4 \mu_B/\text{f.u.}$. The saturation moment of isotropic GdNi_5 is explained using three different contributions [6]. The main contribution comes from the saturation moment of Gd^{3+} ion ($+7 \mu_B/\text{f.u.}$). The second contribution is from the polarization of the partially filled $3d$ band which couples antiparallel to the $4f$ moments ($-0.76 \mu_B/\text{f.u.}$). The third contribution is from the positive coupling of the $4f$ moments with the polarization of the itinerant electrons ($+0.56 \mu_B/\text{f.u.}$). The smaller value of the saturation moment is due to the net effect of the above three contributions. In the case of GdNi_4B , the negative contribution from the polarization of the $3d$ band is absent because of the possible filling up of the $3d$ bands, giving rise to a higher value of the saturation moment. In the same way, the higher value of the saturation moment in GdNi_4Ga also can be attributed to the absence of the $3d$

contribution. Also the itinerant-electron polarization contribution in GdNi₄Ga (0.25 μ_B /f.u) can be considered to be less than that in GdNi₅ (0.56 μ_B /f.u). This decrease may be due to the increase in the unit cell volume of GdNi₄Ga which in turn decreases the T_C , as discussed above.

From the measured heat capacity of GdNi₄Ga, the magnetic contribution to the heat capac-

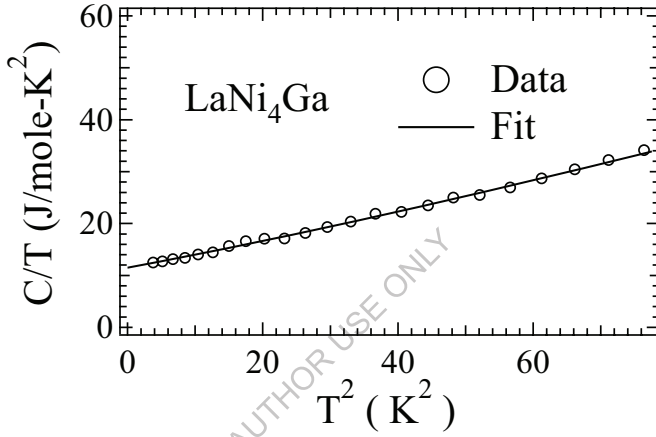


Fig. 4.20: C/T vs T^2 curve for LaNi₄Ga with a straight line fit to obtain the electronic contribution γ from the intercept.

ity (HC) was isolated by subtracting the HC of nonmagnetic LaNi₄Ga. The magnetic contribution to the entropy was then calculated and was found to be 18.3 J/mole-K (inset of Fig. 4.19). This value is higher than the expected value, $R \ln(2J+1) = 17.3$ J/mole-K, for the ground state of Gd³⁺ with $J = 7/2$. Now if we consider the contribution to the entropy arising from the polarization of the conduction electrons as discussed above, we get the total entropy as $R(\ln 8 + 0.25 \ln 2) = 18.7$ J/mole-K in agreement with the experimentally obtained value. This supports our assumption of polarization of the conduction electrons as mentioned above. The low temperature HC, plotted as C/T vs T^2 , of LaNi₄Ga is shown in Fig. 4.20. The y -axis intercept which provides the electronic specific heat coefficient (γ) obtained by extrapolating the linear fit to $T^2 = 0$ axis is $\gamma = 12$ mJ/mole-K. The value of the susceptibility obtained at 4 K is $\approx 4 \times 10^{-4}$ emu/mole (Fig. 4.4). The values of γ and susceptibility are less than half compared to that of the parent compound LaNi₅.

($\gamma = 34.35$ mJ/mole-K [24] and $\chi \approx 20 \times 10^{-4}$ emu/mole [25]). Bloch *et al* [26] have theoretically shown that in case of rare earth-transition metal binary or pseudo binary compounds, weak paramagnetism and low electronic specific heat are characteristic of filled $3d$ bands. In other words, higher density of $3d$ states at the Fermi level gives rise to larger values of γ and χ , as in the case of LaNi_5 [25]. Therefore we presume that the $3d$ band is full in LaNi_4Ga , while it is nearly filled in the case of LaNi_5 . This suggests that in LaNi_4Ga the electronic states near the Fermi level are mainly of $5d$ character which explains the non magnetic behavior of Ni.

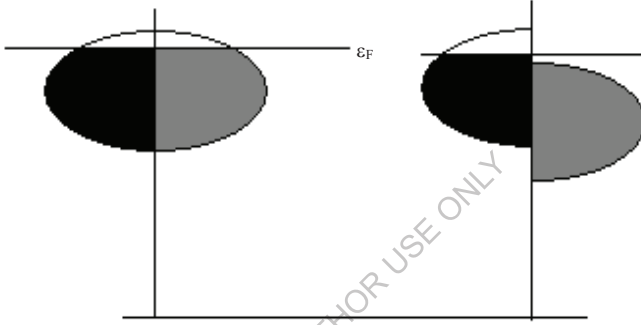


Fig. 4.21: Density of states for $3d$ electrons with spin up (dark) and spin down (light) states. The horizontal straight line within the band denotes the Fermi surface

The question of completely filled or nearly filled $3d$ orbital for LaNi_5 and LaNi_4Ga , that are Pauli paramagnets, can be explained in the following manner. In case of LaNi_5 , there is an unfilled $3d$ band, but the Fermi level is such that both the spin up and spin down bands have the same density of states. (Fig. 4.21). So Pauli paramagnetism arises in this compound. When La is replaced by other magnetic rare earths, the internal field of the rare earth ion splits the band (Fig. 4.21) and Ni bears a polarization moment. Whereas in the case of $R\text{Ni}_4\text{Ga}$, we assume that an extra electron coming from Ga atom fills up the $3d$ band completely and hence the question of splitting does not arise in the presence of internal fields. As a result, the saturation moment increases above the theoretically expected value.

4.3.3 Detailed Discussion for SmNi_4Ga and TbNi_4Ga :

The real and the imaginary part of the AC susceptibility for TbNi_4Ga are shown in Fig. 4.22. Both the curves show anomaly only at the transition temperature. The HC of TbNi_4Ga

showed two extra peaks, one at 5 K and another 2.5 K below the magnetic ordering temperature (Fig. 4.16b). These anomalies are seen more clearly if C/T is plotted as a function of T , as

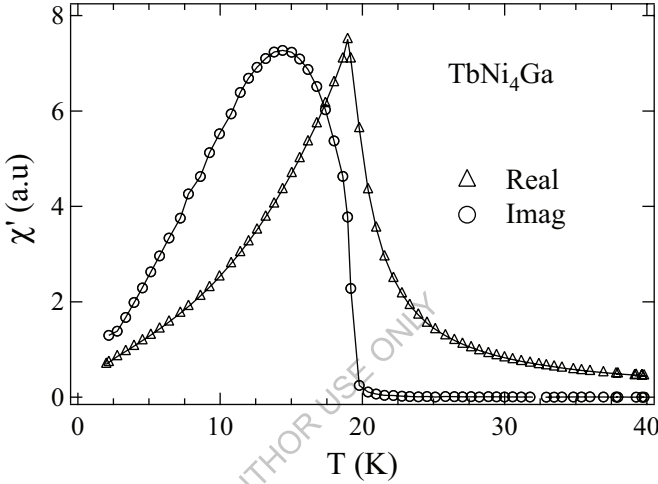


Fig. 4.22: AC susceptibility for TbNi₄Ga with both Real and Imaginary part.

shown in Fig. 4.23. Since these anomalies are absent in the magnetization as well as in the AC susceptibility measurements, it can be assumed that they arise due to the crystal field effects. The magnetic entropy (~ 12.3 J/mole-K, see inset of Fig. 4.23) obtained is also much less than that expected for a $J = 6$ ground state of Tb³⁺ ion (21.3 J/mole-K), again confirming the presence of strong crystal field effects in this compound. The nature of AC susceptibility and heat capacity in TbNi₄Ga is different compared to that observed in TbNi₅, which shows helimagnetic structure below the magnetic ordering [5]. A possible explanation for this difference in TbNi₄Ga is that the substitution of Ga changes the crystal field and hence the anisotropy of the compound. This causes the deviation of the T_c from the de-Gennes scaling, suppression of helimagnetic structure [5] and the Schottky type anomaly in heat capacity at low temperatures. The change in anisotropy is further confirmed by the magnetization isotherm at 2 K (Fig. 4.24). The coercive field for TbNi₄Ga obtained at 2 K is 2 kOe, which is higher (negligible in TbNi₅) than that of the parent

compound [11] indicating an increase in the anisotropy of the compound. Similar increase in the anisotropy was also observed for $\text{TbNi}_{5-x}\text{M}_x$ ($M = \text{Cu} \text{ \& \; Al}$) compounds [11] which was explained on the basis of the appearance of a local uniaxial anisotropy of Tb^{3+} ions in the basal plane of the compounds.

Figure 4.25 shows the real and the imaginary part of the AC susceptibility for SmNi_4Ga with a peak at the magnetic ordering temperature. However, the HC of SmNi_4Ga shows an upturn at low temperatures in addition to the regular peak at the transition temperature (Fig. 4.26), which is again a signature of a Schottky type anomaly. The magnetic isotherm for SmNi_4Ga at 2 K is

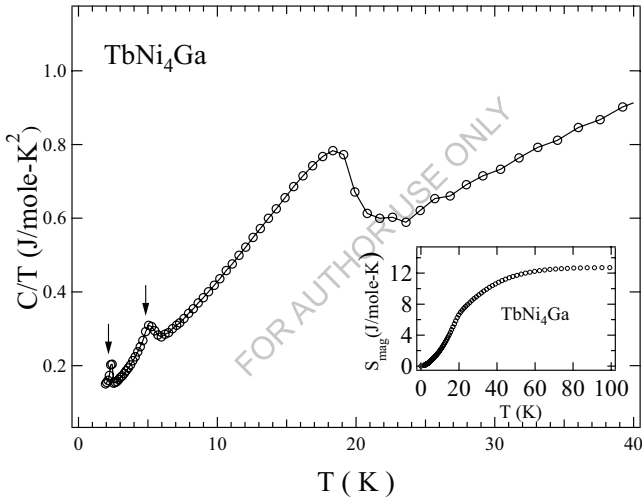


Fig. 4.23: C/T vs T curve for TbNi_4Ga indicating additional anomalies below the transition temperature. Inset shows the magnetic entropy for TbNi_4Ga .

shown in Fig. 4.27. The coercive field obtained is ~ 40 kOe. Such a high coercivity is attributed to the dominant anisotropic energy and narrow domain walls [27]. Initially when the field

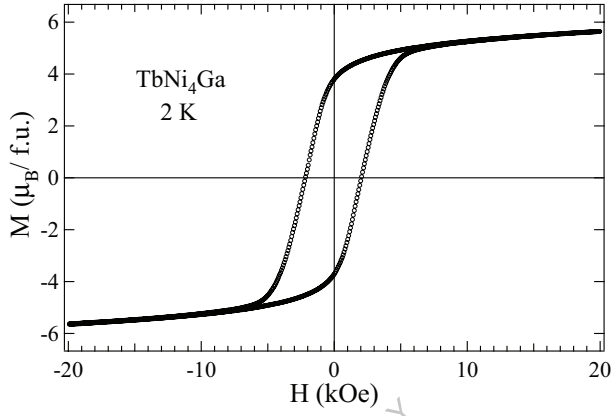


Fig. 4.24: Magnetic isotherm for TbNi_4Ga at 2 K with a coercive field of 2 kOe.

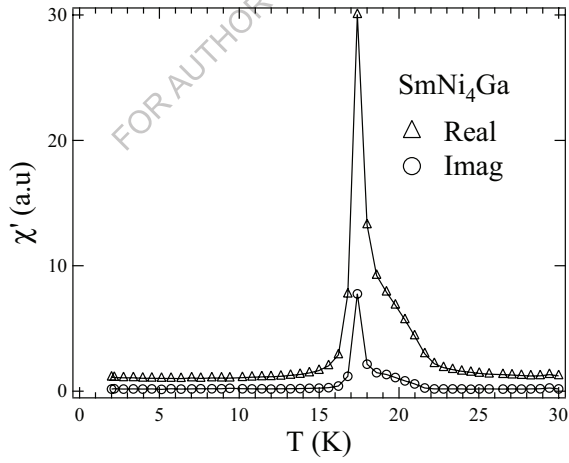


Fig. 4.25: Real part of the AC susceptibility of SmNi_4Ga at zero field

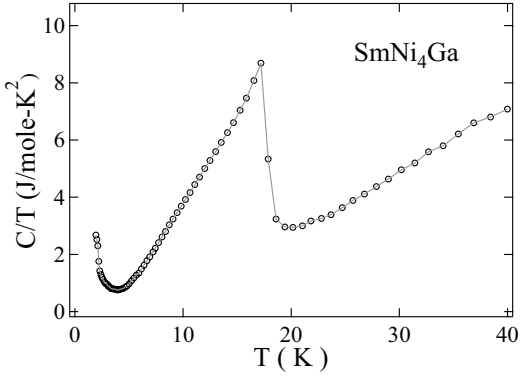


Fig. 4.26: C/T vs T curve for SmNi_4Ga indicating additional anomaly below the transition temperature.

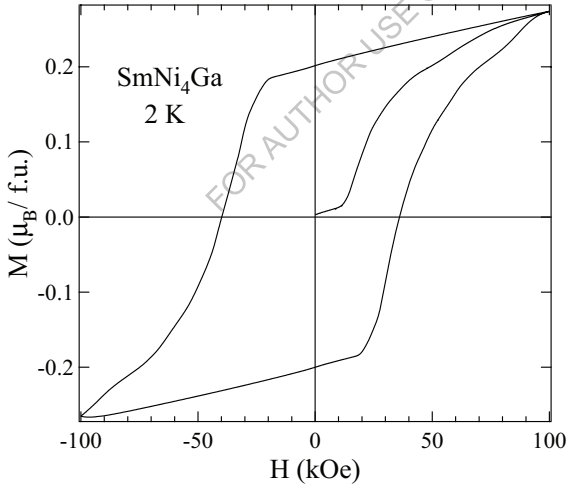


Fig. 4.27: Magnetic isotherm for SmNi_4Ga at 2 K.

is increased from zero, the magnetization increases slowly with field until a critical field is reached where there is a sharp increase in the magnetization. The initial slow increase in mag-

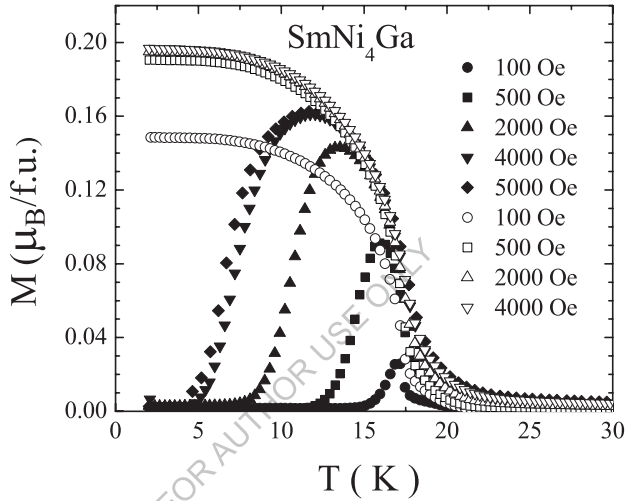


Fig 4.28: Magnetization vs temperature plot for SmNi_4Ga at various fields under ZFC (unfilled symbols) and FC (filled symbols) conditions.

netization occurs when the narrow domain walls find it difficult to move within the grains. Within a grain when the domain wall comes across a nonmagnetic or impurity atom, the domain wall gets pinned since such a position corresponds to a minimum energy region [28]. A critical field is required to move such a domain wall across the grain. The magnetization vs temperature curves for SmNi_4Ga are shown in Fig.4.28 for fields up to 5 kOe under zero field cooled (ZFC) and field cooled (FC) conditions. The difference in magnetization under ZFC and FC condition appears for most of the ferromagnets at low fields because of their anisotropic magnetic property. However, the difference between the ZFC and FC for SmNi_4Ga exists even at a field as high as 5 kOe. Such a behavior is attributed to highly anisotropic property of the compound. It is clear that while increasing the temperature in the ZFC mode, the temperature at which there is an apprecia-

ble increase in the magnetization increases as the field is reduced. This is because the field compensates for the temperature or vice versa for the energy required to overcome the energy barrier within the grain. Similar behavior is also found for YCo_2Ni_3 [29], SmNi_4B [27] and $\text{SmCo}_{5-x}\text{Al}_x$ [30] compounds. The dominant mechanism of coercivity present in such compounds is the domain wall pinning type and hence we presume that, the same is effective in SmNi_4Ga .

A rough estimate for the thickness of the domain walls in the case of SmNi_4Ga can be ob-

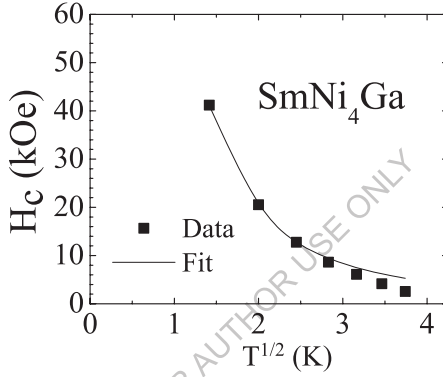


Fig 4.29: Variation of the coercive field with temperature, along with a fit to an equation in text.

tained from the temperature dependence of the coercive field (H_c) (Fig. 4.29), using the indirect equation,

$$H_c/H_{c0} = -V_T T + [1 + (V_T T)^2]^{1/2} \quad (4.4)$$

where $V_T = 15.4k_B/a_0^2\gamma$, the domain wall thickness $\delta = \pi\gamma/4K$, $H_{c0} = H_c$ at 0 K, γ = domain wall energy/unit area, a_0 is the lattice constant and K is the anisotropy constant [31]. The solid line in Fig. 4.29 represents a least square fit for equation (4.4) to the H_c data plotted against $T^{1/2}$. The deviation of the fit at high temperatures may be due to the variation in anisotropy with temperature. The estimated wall energy is $\gamma = 2.1$ erg/cm² for an average lattice constant of $a_0 = 4.5$ Å (under the cubic assumption [3] since the lattice constants, a and c of the hexagonal

SmNi₄Ga are nearly equal). The estimated thickness of the domain wall comes out to be $\approx 8 \text{ \AA}$. This corresponds to two unit cells of SmNi₄Ga. Substitution of a non-magnetic material in a fully magnetic compound (contribution to magnetization from all constituents) increases the coercivity of the compound in most of the cases [27,30,32] (provided the comparison being done on samples made under similar conditions). The main reason behind the increase in coercivity is the change in the mechanism responsible for coercivity. A domain wall nucleation type mechanism changes to pinning type mechanism. The pinning mechanism depends highly on the anisotropy of the material and hence dominates at low temperatures.

4.4 Summary

We have synthesized and studied the magnetic properties of the ternary gallides $R\text{Ni}_4\text{Ga}$ (R = rare earths). These compounds form a substitutional variant of the parent $R\text{Ni}_5$ compounds. All the magnetic rare earth compounds show ferromagnetic ordering at low temperatures except PrNi₄Ga which follows the Curie-Weiss behavior down to 2 K. LaNi₄Ga and LuNi₄Ga show a Pauli paramagnetic behavior down to 2 K, indicating the nonmagnetic behaviour of Ni in these compounds. The transition temperatures are smaller compared to their respective parent compounds $R\text{Ni}_5$. The T_c values of $R\text{Ni}_4\text{Ga}$ compounds do not follow the *de-Gennes* scaling. In particular, the T_c of SmNi₄Ga & TbNi₄Ga vary appreciably from the expected values and the possible reason is attributed to the crystal field effects. All the compounds, except GdNi₄Ga, show magnetic anisotropy. The magnetic ordering of GdNi₄Ga has the possibility of a helical magnetic structure and a filled up 3d band. SmNi₄Ga is a hard magnet with narrow domain walls at low temperatures. The thickness of the domain wall calculated comes out to be $\approx 8 \text{ \AA}$.

4.5 References:

- 1 H.H. Vanmal, K.H.J. Buschow and A.R. Miedena, *J. Less. Comm. Metals* **35** (1975) 65.
- 2 H. Ishimoto, N. Nishida, T. Furubayashi, M. Shinohara, Y. Takano, Y. Miura and K. Ono, *J. Low. Temp. Phys.* **55** (1984) 17.
- 3 H. Oesterreicher, F.T. Parker and M. Misroch, *Phys. Rev. B*, **18** (1978) 480.
- 4 K.H.J. Buschow, *Rep. Prog. Phys.* **40** (1977) 1179.
- 5 V.M.T.S. Barthem and E.A.M. da Gama, *J. Phys. Condens. Matter* **9** (1997) 7609.
- 6 S. K. Malik, F. J. Arlinghaus and W. E. Wallace, *Phys. Rev. B*, **25** (1982) 6488.

- 7 H. Oesterreicher, F.T. Parker and M. Misroch, *Applied Physics* (Berlin) **16** (1978) 185.
- 8 A. Kowalczyk, T. Toliński, B. Andrzejewski and A. Szlaferek, *J. Alloys. Compd.* **413** (2006) 1.
- 9 N.M. Hong, T. Holobar, G. Hilsher, M. Vybemou and P. Rogl, *IEEE Trans, Magn.* **30** (1994) 4966.
- 10 I.S. Dubenko, I.Yu. Gaidukova, S.A. Granovasky, V. Rodimin, A.S. Markosyan, S. Roy and N. Ali, *IEEE Trans, Magn.* **36** (2000) 3336.
- 11 A.G. Kuchin, A.S. Ermolenko, V.I. Khrabrov, N.I. Kourov, G.M. Makarova, Ye.V. Belozarov, T.P. Lapina and Yu.A. Kulikov, *J. Magn. Magn. Mater.*, **238** (2002) 29.
- 12 T. Toliński, A. Kowalczyk, A. Szlaferek and B. Andrzejewski, *J. Alloys. Compd.* **374** (2002) 31.
- 13 H. Flandorfer, P. Rogl, K. Hiebl, E. Bauer, A. Lindbaum, E. Gratz and C. Godart, *Phys. Rev. B*, **50** (1994) 15527.
- 14 A. Kowalczyk, M. Pugaczowa-Michalska and T. Toliński, *Phys. Stat. Sol. B* **242** (2005) 433.
- 15 H.C. Hamaker, L.D. Wolf, H.B. Mackey, Z. Fisk and M.B. Maple, *Solid State Comm.*, **32** (1979) 289.
- 16 R. Ballou, V.M.T.S. Barthem and D. Gignoux, *Physica B*, **149** 340 (1998).
- 17 D. R. Noakes and G. K. Shenoy, *Phys. Lett.*, **91A** (1982) 35.
- 18 B. D. Dunlap, L. N. Hall, F. Behrooz, G. W. Crabtree and D. G. Niarchos, *Phys. Rev. B*, **29** (1983) 6244.
- 19 D. T. Adroja and S. K. Malik, *Phys. Rev. B*, **45** (1992) 779.
- 20 R. Nagarajan, L. C. Gupta, C. Mazumdar, Z. Hossain, S. K. Dhar, C. Godart, B. D. Padalia and R. Vijayaraghavan, *J. Alloys Compd.*, **225** 571 (1995).
- 21 M. B. Maple, *App. Phys.*, **9** 179 (1976) and references therein.
- 22 J.M.D. Coey, V. Skumryev and K. Gallagher, *Nature* **401** (1999) 35.
- 23 L. M. Sandratskii and G.H. Lander, *Phys. Rev. B*, **63** (2001) 134436.
- 24 S. Nasu, *J. Phys. Chem. Of Solids* **32** (1971) 2779.
- 25 D. Gignoux, D. Givord and A. Del Moral, *Solid State Comm.* **19** (1976) 891.
- 26 D. Bloch and F.C.R. Chaissfi, *Acad. Sci., Paris* **274** (1972) 221.
- 27 C. Mazumdar, R. Nagarajan and B.D. Padalia, *Appl. Phys. Lett.* **77** (2000) 895.
- 28 H. Zijlstra, *Ferromagnetic Materials*, 3 (1988) 37 E.P. Wohlfarth (Eds.).

- 29 H. Oesterreicher, F.T. Parker and M. Misroch, *Solid State Comm.* **19** (1976) 539.
- 30 H. Oesterreicher, *J. Phys. F. Metal Physics*, **5** (1975) 1607.
- 31 F. T. Parker and H. Oesterreicher, *J. Magn. Magn. Mater.*, **36** (2002) 195.
- 32 H. Oesterreicher, F.T. Parker and M. Misroch, *J. Appl. Phys.* **49** (1978) 2058.

FOR AUTHOR USE ONLY

Chapter 5

Magnetic Properties of RNi_3TGa (R = rare earths, T = Fe and Mn) compounds

5.1 Introduction

RNi_4Ga series of compounds have exhibited some interesting properties such as ferromagnetic ordering, crystal field effects, high coercivity, etc. Compounds with almost all the magnetic rare earths undergo ferromagnetic transition at low temperatures. In the ordered state, $GdNi_4Ga$ has the possibility of a helical structure and a filled $3d$ band. $SmNi_4Ga$ shows high coercivity at low temperatures. $LaNi_4Ga$ and $LuNi_4Ga$ show Pauli-paramagnetic behavior. Since Ni is nonmagnetic in this series of compounds [1, 2], the interaction is only among the rare earth moments. It is also of interest to see whether a substitution can make the transition element magnetic within the lattice. This will provide us an opportunity to study the interaction between the $3d$ and $4f$ orbitals. If the transition element is magnetic in the lattice then it couples ferromagnetically with light rare earths and antiferromagnetically with heavy rare earths [1]. All these can provide us an opportunity to study a variety of interesting fundamental properties. Considering this, we have studied the RNi_4Ga series of compounds by substituting Fe and Mn at the Ni site. Ni is nonmagnetic, Co is known to form magnetic compounds in RM_5 ($M = 3d$ element) lattice [1] and hence we selected Fe and Mn to see whether they will become magnetic or nonmagnetic in the RNi_4Ga lattice.

5.2 Sample Preparation and Crystal Structure

Polycrystalline samples of RNi_3FeGa and RNi_3MnGa series of compounds were prepared by the standard arc melting procedure as discussed in Chapter 4. In case of the RNi_3MnGa compounds, special care was taken during the melting because of the volatile nature of both Mn and Ga. The total weight loss during the arc melting in case of RNi_3FeGa series of compound was less than 0.5%. In case of RNi_3MnGa series, the weight loss was more, $\approx 2-3\%$ per melting. The extra loss was compensated by adding more Mn to the sample. The as melted buttons were wrapped in Tantalum foil, sealed in evacuated quartz tube and annealed. The RNi_3FeGa series of compounds were annealed for 7 days and RNi_3MnGa were annealed for 15 days. All The compounds were brittle in nature. The compounds with lighter rare earths in both the series were not stable in air, specially the La compounds. Room temperature powder X-ray diffraction pattern of

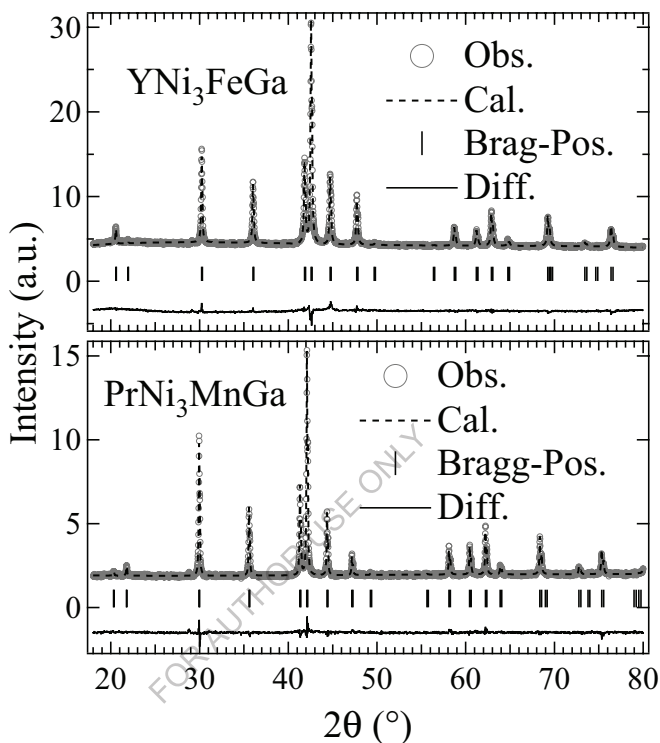


Fig. 5.1: Rietveld analysis of the X-ray pattern of YNi_3FeGa and $PrNi_3MnGa$

the samples were obtained using Panalytical X-ray diffractometer equipped with $Cu-K_\alpha$ radiation. The X-ray patterns of the samples before and after annealing were compared. It was found that the RNi_3FeGa series of compounds form readily after melting. The X-ray pattern obtained under similar X-ray exposure times, before and after annealing of the compounds, were same except that the intensity increased after annealing. However, in case of the RNi_3MnGa series of compounds, the X-ray pattern before annealing consisted of broad peaks with some small impurity phases. The X-ray pattern obtained after the annealing was sharp and intense with no impurity phases. Two trials to make $ErNi_3MnGa$ and $SmNi_3MnGa$ in single phase failed. In case of $SmNi_3MnGa$ the volatile nature of Sm, Mn and Ga might be responsible for the non formation of

the compound in single phase. In case of $ErNi_3MnGa$ the exact reason is not known. The compound forms but a little unknown impurity phase is always present. The formation of the Mn doped compounds after annealing indicates less solubility of Mn compared to Fe in the parent compound.

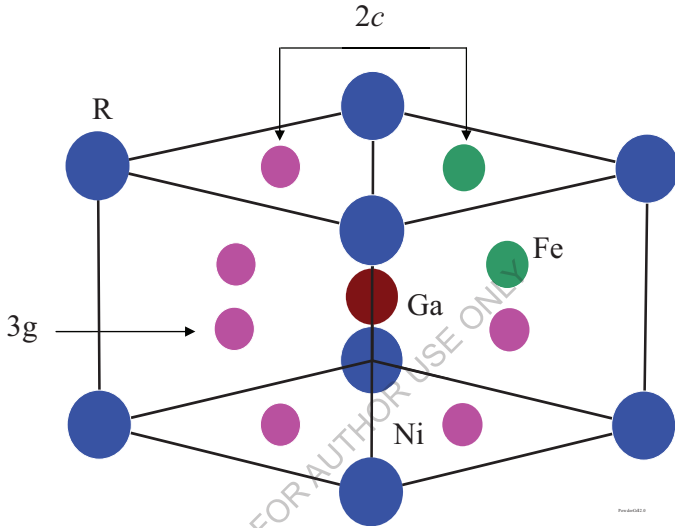


Fig. 5.2: Crystal structure of RNi_3TGa ($T = Mn$ and Fe) compounds with a $1/3$ hexagonal unit cell. $2c$ and $3g$ represent the crystallographic sites. The corners represent the crystallographic site $1a$.

In order to obtain the structure type and the lattice parameters of the compound, a Rietveld refinement (FullProf program) of the XRD pattern was carried out. The Rietveld refinement of the X-ray pattern of YNi_3MnGa and $PrNi_3FeGa$ is shown in Fig. 5.1. To start with, the lattice parameters and the space group of the parent compounds were given as the input to the program. The best fit to the X-ray pattern was obtained by considering the crystallographic parameters as given in Table 5.1. For compounds with other rare earths, only the temperature factor changes. It was found that all the compounds of both the series form in the $CaCu_5$ type hexagonal structure with a space group $P6/mmm$, maintaining the structure of the parent compound.

Table 5.1: Crystallographic parameters for RNi_3TGa ($T = Mn$ and Fe) compounds. The occupancy of Ni atoms has changed compared to the parent compound.

| Atom | Site Symmetry | x | y | z | $U_{eq}(\text{\AA}^2)$ | Occupancy |
|-------|---------------|-------|-------|------|------------------------|-----------|
| Y | $1a$ | 0.00 | 0.00 | 0.00 | 0.068 | 1 |
| Ni | $2c$ | 0.333 | 0.666 | 0.00 | 0.045 | 1.5 |
| Fe/Mn | $2c$ | 0.333 | 0.666 | 0.00 | 0.045 | 0.5 |
| Ni | $3g$ | 0.50 | 0.00 | 0.50 | 0.052 | 1.5 |
| Fe/Mn | $3g$ | 0.50 | 0.00 | 0.50 | 0.052 | 0.5 |
| Ga | $3g$ | 0.50 | 0.50 | 0.50 | 0.023 | 1 |

Table 5.2: Lattice parameters of RNi_3FeGa and RNi_3MnGa series of compounds.

| R | RNi_3FeGa | | RNi_3MnGa | |
|-----|-------------|---------|-------------|---------|
| | a (Å) | c (Å) | a (Å) | c (Å) |
| Y | 5.002 | 4.01 | 5.030 | 4.045 |
| La | 5.128 | 4.076 | 5.164 | 4.12 |
| Ce | 4.964 | 4.084 | 5.064 | 4.115 |
| Pr | 5.0733 | 4.0665 | 5.1263 | 4.1028 |
| Nd | 5.0632 | 4.061 | 5.092 | 4.101 |
| Sm | 5.0462 | 4.052 | - | - |
| Gd | 5.0273 | 4.0467 | 5.054 | 4.0972 |
| Tb | 5.0147 | 4.031 | 5.0421 | 4.0797 |
| Dy | 5.011 | 4.0198 | 5.0289 | 4.053 |
| Ho | 4.988 | 3.998 | 5.0189 | 4.042 |
| Er | 4.972 | 3.961 | - | - |

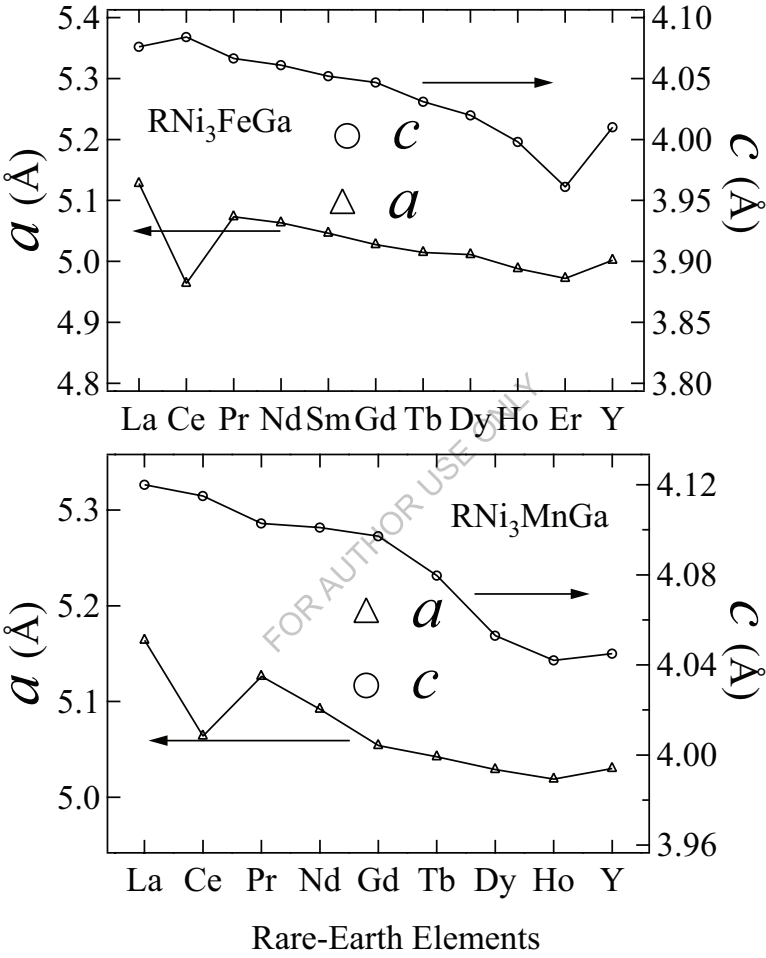


Fig. 5.3: Lattice parameters of RNi_3FeGa and RNi_3MnGa series of compounds plotted against the corresponding rare earths.

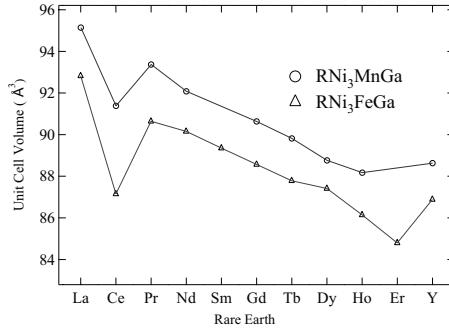


Fig. 5.4: Comparison of the unit cell volume of the RNi_3FeGa and RNi_3MnGa series of compounds

Figure 5.2 shows the hexagonal crystal structure (one third) of the $RNi_3T Ga$ series of compounds. Rare earth atoms occupy the corners, crystallographically referred to as the $2a$ site for a hexagonal structure. In the parent compound RNi_5 , Ni occupies the $2c$ and $3g$ sites (shown in Fig. 5.2) with occupancy 2 and 3, respectively [3]. Ga goes only to the $3g$ site because of the larger size compared to Ni atom. While substituting Fe and Mn in RNi_4Ga compounds, a better fit was obtained by considering Fe and Mn equally occupied at both the sites. The site preference can be known from the occupancy of the atom used for the Rietveld fit. Equal preference to both the sites by the substituting atom may be due to the comparable size of Fe, Mn and Ni atoms.

The lattice parameters of RNi_3FeGa and RNi_3MnGa compounds are given in Table 5.2 and plotted against their corresponding rare earth in Fig. 5.3. The lattice parameters of RNi_3FeGa and RNi_3MnGa compounds are larger than that of their corresponding parent compound RNi_4Ga . The metallic radii of Mn and Fe are slightly higher than that of Ni and hence there is a marginal increase in the lattice parameters. The unit cell volumes of RNi_3FeGa and RNi_3MnGa compounds are shown in Fig. 5.4, which clearly show the same trend of lanthanide contraction as expected for the trivalent rare earth ions, except for Ce. This indicates that Ce is in a mixed valent state in both the series as in the parent compound [4]. The unit cell volumes of the Mn compounds are larger than that of the corresponding Fe compounds because of the slightly larger atomic radius of Mn (1.28 Å) ion compared to that of the Fe (1.26 Å) ions. The lattice pa-

parameter a of $CeNi_3FeGa$ shows a discontinuity type behavior where as c follows the same trend as the other rare earths.

5.3 Results and Discussions

5.3.1 RNi_3FeGa and RNi_3MnGa ($R = \text{Nonmagnetic rare earths, La and Y}$):

Rare earth elements La and Y make up the nonmagnetic counterparts of the RNi_4Ga series of compounds, since Ni is nonmagnetic in these compounds. If the substitution of other $3d$ elements makes these compounds magnetic, then the magnetism should arise from the substituted $3d$ elements. In order to verify this, we first studied the Fe and Mn doped ternary gallides YNi_4Ga and $LaNi_4Ga$.

The variation of susceptibility with temperature for YNi_3FeGa under field cooled (FC) and zero field cooled (ZFC) conditions is shown in Fig. 5.5a. The ZFC susceptibility shows a sharp increase below ~ 100 K and shows a broad peak ~ 30 K and then decreases below 10 K. The susceptibility under FC conditions follows the ZFC curve down to ≈ 12 K (below the peak) and then separates from it showing a temperature independent behavior down to 2 K. The temperature independent susceptibility at low temperatures is expected for a ferromagnetic compound. However, the FC-ZFC bifurcation after the peak in susceptibility is usually expected for a spin glass or superparamagnetic type systems. The magnetic isotherm at 2 K (Fig. 5.5b) shows a curvature, which indicates the presence of a ferromagnetic component. The moment obtained at 90 kOe is $\approx 1.4 \mu_B/\text{f.u.}$, which is less than that expected for pure Fe ($\approx 2 \mu_B/\text{f.u.}$). Even though the susceptibility shows a sharp deviation below 100 K, the inverse susceptibility shows a clear deviation from the straight line behavior below 200 K (Fig. 5.5c). Even in the paramagnetic state above 200 K, the inverse susceptibility could not be fitted to the Curie-Weiss law with admissible values of the parameters.

In order to further investigate the magnetic behavior of this compound, the AC susceptibility was measured at various frequencies. The real part of the AC susceptibility (Fig. 5.6a) clearly shows a shift of the peak towards high temperatures with frequency. The peak height decreases with the frequency. In the imaginary part of the AC susceptibility (Fig. 5.6b), the peak height increases with frequency with the same temperature shift. Such a behaviour is generally expected for a super-paramagnet or a spin glass. To differentiate between the spin glass and super para

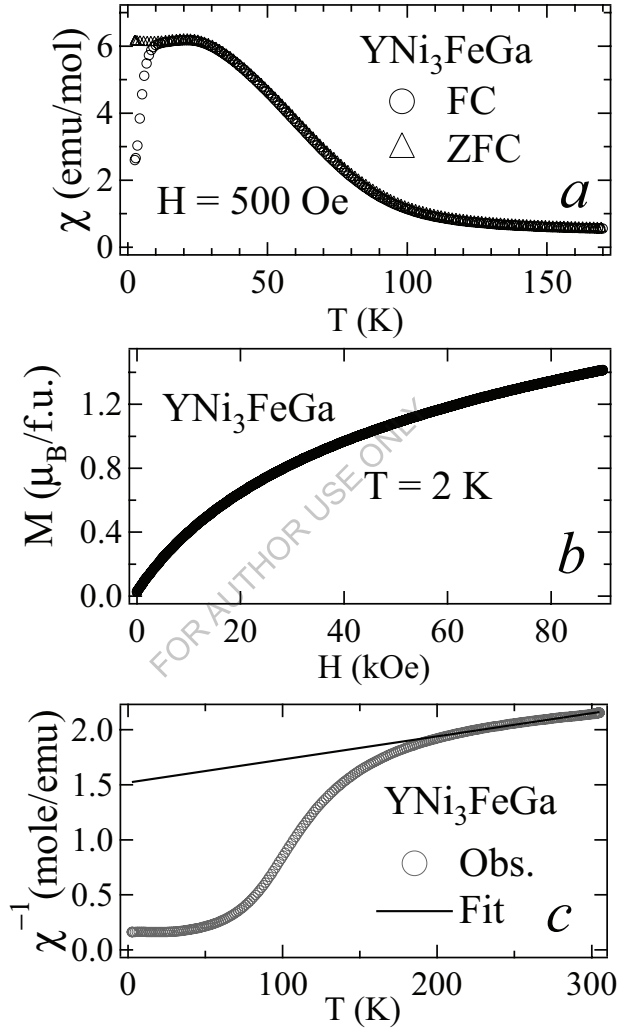


Fig. 5.5: (a): Temperature variation of susceptibility at 500 Oe for YNi_3FeGa . (b): Magnetic isotherm for the same at 2 K. (c): χ^{-1} vs T plot for the same.

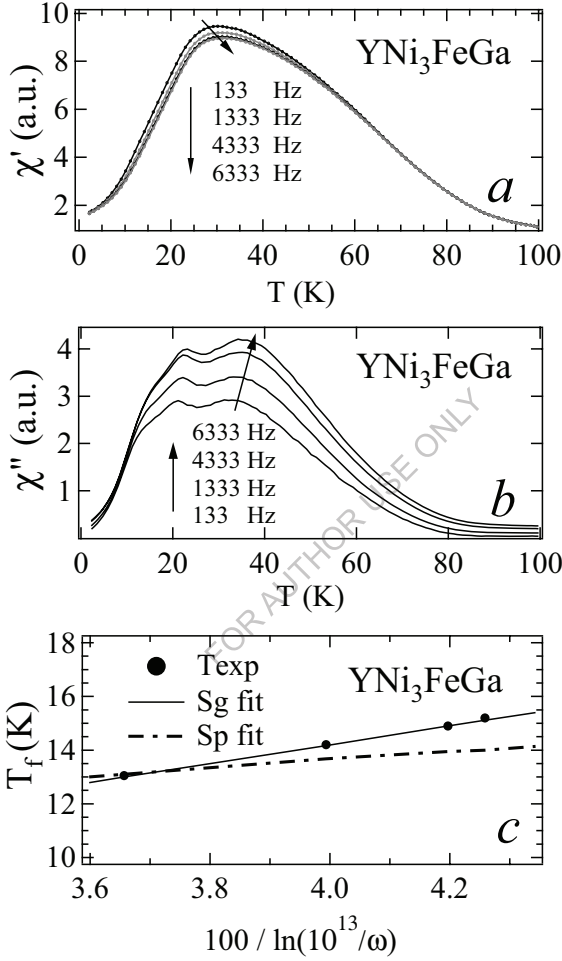


Fig. 5.7: Real part (a) and Imaginary part (b) of the AC susceptibility for YNi_3FeGa . Variation of T_g with frequency is fitted to Vogel-Fulcher law for spin glass and super paramagnetic cases as shown in (c).

magnetic behavior, the shift in the freezing temperature (T_f) with frequency was fitted to the Vogel-Fulcher law [5],

$$\omega = \omega_0 \exp\left(-E_a / k_B (T_f - T_a)\right) \quad (5.1)$$

where ω_0 is the characteristic frequency, E_a is the activation energy and T_a is the Vogel-Fulcher temperature. The freezing temperature T_f of a spin glass material should be proportional to $\ln(\omega / \omega_0)$. Substituting the typical values used within the range for the spin glass type behavior ($\omega_0 = 10^{13}$ Hz, $E_a = 325$ K and $T_a = 24.4$ K) [5], the fit obtained is shown as solid line in Fig. 5.6c. The data was also fitted with parameter values admissible for the superparamagnetic behavior ($\omega_0 = 10^{30}$ Hz and $E_a = 845$ K), shown as broken line in Fig. 5.6c. It is very clear that the Vogel-Fulcher law fits much better with the parameter values admissible for the spin glass type behavior and hence the magnetic behaviour of YNi_3FeGa can be considered as spin glass type behavior. Another characteristic of the spin-glass compounds is that the magnetization of the material below the freezing temperature reacts to the applied field over a period of time. One of the parameters describing such a behavior is the thermoremanent magnetization (TRM). To obtain the TRM, the remnant magnetization is measured as a function of time after removing the field in which the sample is cooled from a temperature well above the freezing temperature T_f to a temperature well below. YNi_3FeGa was cooled down to 2 K in an applied field of 100 Oe. The observed decay of the magnetization after the removal of the field at 2 K is shown in Fig. 5.7. There are various models to fit this time dependent magnetization. One of the models [6], based on the assumption that the energy barriers which cause the slow response to the field are uniformly distributed from zero to some maximum energy, considers that the remnant magnetization decay logarithmically as

$$M(t) = M_0 - S \log(t) \quad (5.2)$$

where M_0 and S are the fit parameters which depend upon the temperature and the relaxation rate. M_0 is the magnetization at $t = 1$ unit. The TRM plot (Fig. 5.7) was fitted to the above equation (solid line in Fig. 5.7) with $M_0 = 2.129$ emu/g and $S = 0.0019$ emu/g. The value of S is related to the magnetic viscosity of the system and no definite conclusion can be drawn from it. But a reasonably good fit to equation (5.2) indicates the spin glass type behavior of the compound. The remanent magnetization (TRM) value obtained is ≈ 2.12 emu/g at 2 K and 100 Oe.

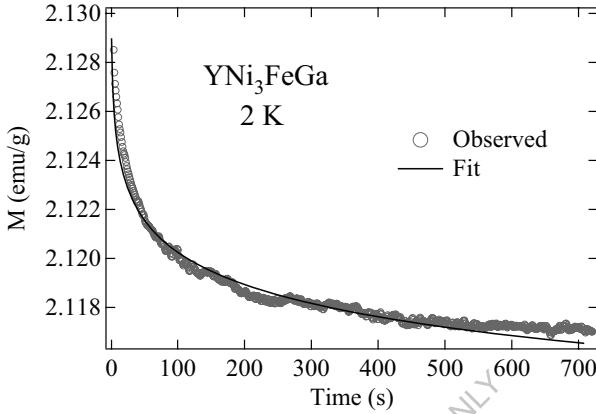


Fig. 5.7: Thermoremanent magnetization as a function of time at 2 K after field cooling the sample at 100 Oe. Solid line is the fit to equation (5.2) given in the text.

The temperature variation of the susceptibility of LaNi_3FeGa is shown in Fig. 5.8a. The behavior is similar to that of the YNi_3FeGa compound except that the peak (~ 20 K) is narrower and prominent for LaNi_3FeGa . The ZFC and FC susceptibility curves separate only below ≈ 10 K. The magnetic isotherm at 2 K (Fig. 5.8b) shows saturation type behavior with a moment of $\approx 1.4 \mu_B/\text{f.u.}$ at 90 kOe. The inverse susceptibility above 100 K (Fig. 5.8c) could be fitted to the modified Curie-Weiss law which gave $\mu_{\text{eff}} = 2.7 \mu_B$, $\chi_0 = 0.45 \text{ emu/mole}$ and $\theta_p = -65 \text{ K}$. The value of μ_{eff} is in agreement with the paramagnetic behavior of Fe. To check for the spin glass type behavior, AC susceptibility of the compound was measured at different frequencies, which is shown in Fig. 5.9a. Even though there is a small shift of the peak at higher frequencies that can be seen clearly in the imaginary part of the AC susceptibility (Fig. 5.9b), this shift could not be fitted to the Vogel-Fulcher law. Hence the possibility exists that the compound is on the ferromagnetic side of the spin glass-ferromagnetic border.

The temperature variation of the susceptibility taken under FC and ZFC conditions for YNi_3MnGa is shown in Fig. 5.10a. Both the susceptibilities show a sharp peak at ≈ 35 K and then separate from each other at ≈ 28 K. The behavior is almost similar to that of YNi_3FeGa except

that the peak becomes sharper. In the paramagnetic state of the compound, the susceptibility de

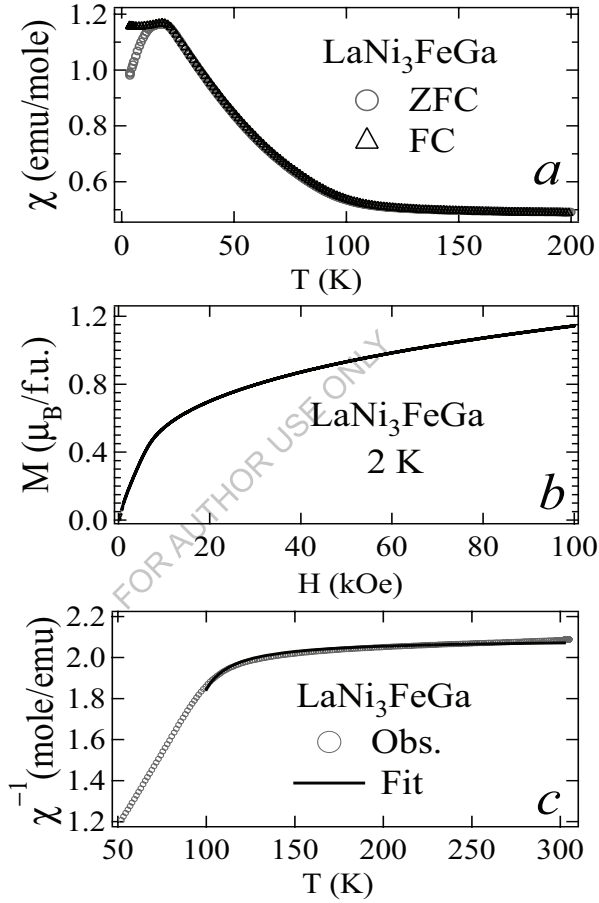


Fig. 5.8: Temperature variation of susceptibility (a) and magnetic isotherm at 2 K (b) for $LaNi_3FeGa$. (c) χ^{-1} vs T plot with Curie-Weiss Fit.

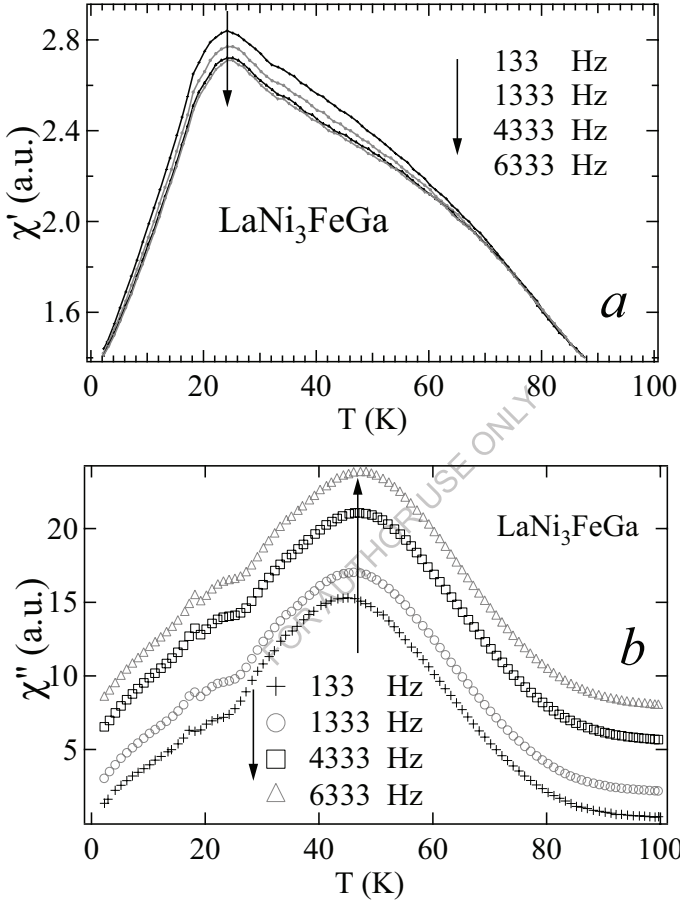


Fig. 5.9: Real part (a) and expanded version of the imaginary part (b) of the AC susceptibility for LaNi_3FeGa .

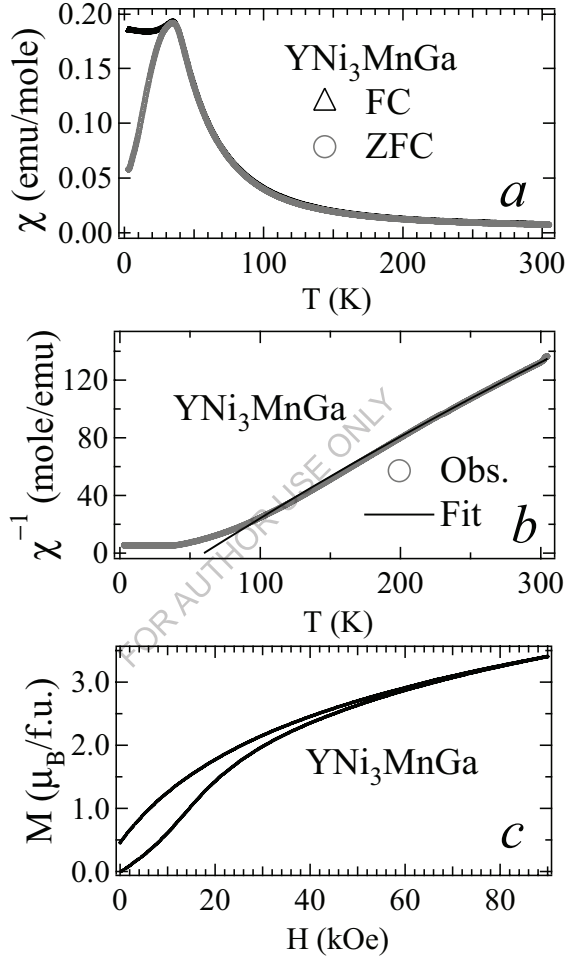


Fig. 5.10: Temperature variation of susceptibility (a), inverse susceptibility with a Curie Weiss fit (b) and the magnetic isotherm at 2 K (c) for YNi_3MnGa .

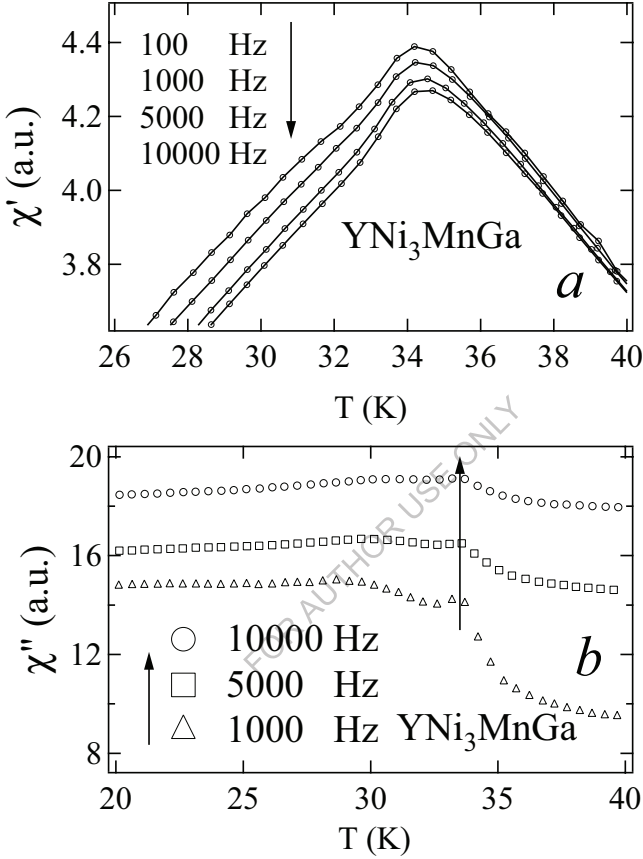


Fig. 5.11: Real part (a) and imaginary part (b) of the AC Susceptibility for YNi_3MnGa

viates from the straight line behaviour below ≈ 100 K. The inverse susceptibility (see Fig. 5.10b) above 100 K could be fitted to the Curie-Weiss law with an effective moment of $3.6 \mu_B$ which is in good agreement within the range expected for the Mn ions. The separation of the FC and ZFC susceptibility below the transition temperature is attributed to the inherent spin glass type behav-

ior. The magnetization behavior of the compound with applied field is shown in Fig. 5.10c. The

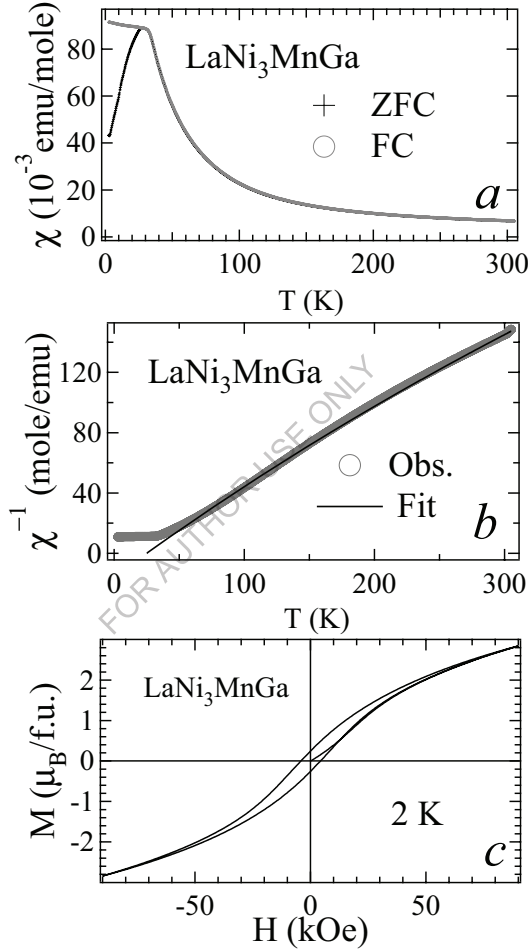


Fig. 5.12: Temperature variation of susceptibility (a), Inverse susceptibility curve with a Curie Weiss fit (b) and Magnetic isotherm at 2 K for $LaNi_3MnGa$

magnetization increases with the field and tend to saturate at high fields as expected for a ferromagnet. The incomplete saturation of the curve at high fields may be due to the anisotropic behavior of the Mn ion. The moment obtained at 2 K and 90 kOe is $3.4 \mu_B/\text{f.u.}$ To investigate

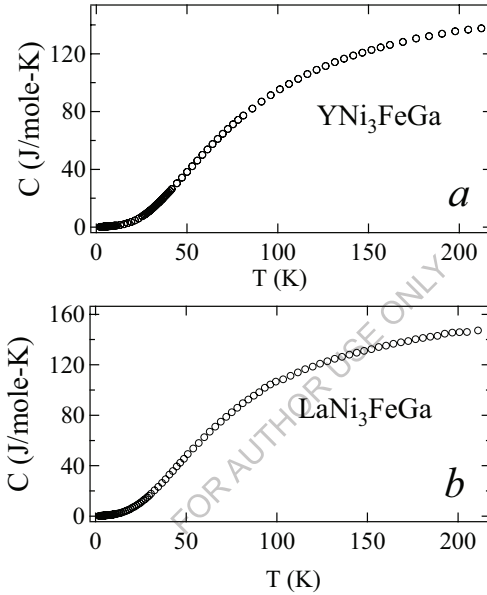


Fig. 5.13: Heat capacity plot for YNi_3FeGa (a) and $LaNi_3FeGa$ (b).

whether the compound shows a spin glass behaviour, AC susceptibility of the compound was measured at different frequencies. Figure 5.11a and Figure 5.11b show the real and imaginary part of the ac susceptibility. The peak in the AC susceptibility (freezing temperature T_f) shifts with frequency towards high temperatures. The shift in the freezing temperature with frequency was fitted to the Vogel-Fulcher law (Eq. (5.1)) which gives the characteristic frequency $\omega_0 = 10^{13}$ Hz, activation energy $E_a = 55.6$ K and $T_0 = 32$ K. The value of the characteristic frequency is typical for the spin-glass systems and the closeness of T_0 to the freezing temperature T_f (34.2 K for $f = 100$ Hz) supports the spin glass behavior of the compound.

The FC and ZFC susceptibility curves of $LaNi_3MnGa$ separate from each other just at the peak temperature ≈ 30 K (Fig. 5.12a). Such a behavior is generally attributed to the anisotropic ferromagnetic behavior of the compound. The peak temperature is lower compared to that of YNi_3MnGa (≈ 34 K). One of the possible reasons is that, for YNi_3MnGa the Mn-Mn distance might be less compared to that of the $LaNi_3MnGa$ because of the lower unit cell volume of the former. The inverse susceptibility (Fig. 5.12b) could be fitted to the modified Curie-Weiss law with $\mu_{eff} = 3.6 \mu_B$, $\theta_p = 60$ K and $\chi_0 = 0.001$ emu/mole. The magnetic isotherm at 2 K shows a behavior similar to that of a ferromagnet with a coercivity of 4 kOe (Fig. 5.12c). The moment obtained at 90 kOe and 2 K is $\approx 2.8 \mu_B/f.u.$, which is comparable to that obtained for YNi_3MnGa .

The heat capacity curves for RNi_3FeGa and RNi_3MnGa ($R = Y$ and La) are shown in Fig. 5.13 and Fig. 5.14, respectively. None of them shows any anomaly at the transition or freezing temperature. One of the possible reasons is that the onset of the Fe or Mn ordering takes place at higher temperatures (≈ 100 K) and completes at low temperatures (where we see a peak in the susceptibility) resulting in a slow change in the entropy. This slow change in entropy may be not distinguishable in the background of a large phonon contribution.

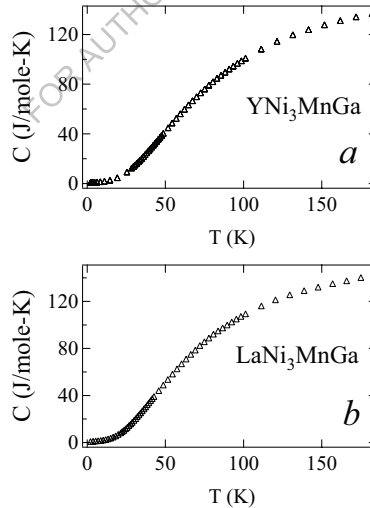


Fig. 5.14: Heat capacity plot for YNi_3MnGa (a) and $LaNi_3MnGa$ (b)

5.3.2 RNi_3FeGa ($R = Ce, Pr, Nd, Sm, Gd, Tb, Dy, Ho$ and Er):

RNi_4Ga series of compounds with magnetic rare earths were found to order ferromagnetically at low temperatures (except Ce and Pr). The ordering was due to the rare earth moments, which interacts via *RKKY* interaction. There was no magnetic contribution from Ni, since the corresponding Y and La compounds showed only a Pauli paramagnetic behavior and $GdNi_4Ga$ showed the property of a filled $3d$ band. However, when Ni is substituted by Fe/Mn, even the non-magnetic rare earth (Y and La) compounds showed magnetic ordering. Again assuming that magnetic moments are not induced on the Ni atoms, the magnetic ordering should arise from the substituted Fe/Mn atoms. This clearly indicates that when Fe/Mn is substituted at the Ni site it retains its magnetic property within the lattice. The effect of the moment on Fe in compounds with magnetic rare earths was studied and is reported as follows.

$CeNi_3FeGa$ shows only a paramagnetic type behavior down to 2 K (Fig. 5.15a). The absence of magnetic ordering is surprising because Fe is found to order ferromagnetically in all the other compounds, including the nonmagnetic rare earth compounds. However, this paramagnetic behaviour is not exactly the Curie Weiss type. The inverse susceptibility (inset of Fig. 5.15a) deviates from the straight line behavior well above 100 K. The magnetic isotherm at 2 K (Fig. 5.15b) is also showing a ferromagnetic type behaviour rather than a paramagnetic type. It is quite possible that the sample is already in the ferromagnetic region at low temperatures, but ordering is not complete to have a peak in the susceptibility. One of the ways to see whether the ferromagnetic ordering has started is to look at the derivative of the DC susceptibility. The derivative of the susceptibility for $CeNi_3FeGa$ is shown in the inset of Fig. 5.15b. The peak in the derivative plot clearly indicates the ferromagnetic ordering. The saturation moment obtained is $\sim 0.8 \mu_B/f.u.$, which is much less than the theoretical value ($\approx 4 \mu_B/f.u.$). The lower value of the moment can be attributed to the incomplete ferromagnetic ordering as well the mixed valent behavior of Ce [4].

The magnetic susceptibility of $PrNi_3FeGa$ (Fig. 5.16a) indicates a magnetic ordering at ~ 60 K. Since both Fe and Pr can order, it is not possible (in the absence of neutron diffraction measurements) to ascertain which one is ordering at 60 K. However, considering the fact that $PrNi_4Ga$ do not show any magnetic ordering, and the magnetic ordering of $3d$ elements are usually high compared to the rare earth moments, we will assume that the ordering is due to the Fe moments. This brings in the possibility whether Pr can also order due to the interaction with the ordered Fe moments. Since the ordering of Fe is ferromagnetic (see the magnetic isotherm at 2 K in Fig.

5.16*b*), any change in the magnetic ordering due to Pr will be masked in the susceptibility curve. The derivative curve (inset of Fig. 5.16*a*) clearly shows a peak at 40 K in addition to the one at the ordering temperature. The other peak at 40 K can be assumed to be arising from the ordering of the Pr moments. This implies that the strong interaction between the ordered Fe moments and Pr moments forces the Pr moments to order, at rather high temperatures (no magnetic ordering in $PrNi_4Ga$). This is further confirmed by the saturation moment obtained from the magnetic isotherm at 2 K, which gives a value of $3.1 \mu_B/f.u.$, more than that expected for the saturation moment of pure Fe ($\approx 2 \mu_B$). This can be possible only if the Pr moments also order ferromagnetically, and align parallel to the Fe moments. This result is as per the general trend because the transition elements couple ferromagnetically with the lighter rare earths and antiferromagnetically with the heavier rare earths in the $R-T$ (R = rare earth, T = $3d$ transition metal) compounds [1]. We have made the same assumption in other compounds also that the first ordering is due to Fe moments which forces the rare earth moments order at temperatures lower than the Fe ordering.

Magnetic susceptibility of $GdNi_3FeGa$ is even more interesting, as shown in Fig. 5.17*a*. The susceptibility curves under ZFC and FC conditions at 500 Oe are separated below the magnetic ordering. One expects negligible anisotropy for Gd moments and hence no difference between the ZFC and FC curves since the orbital angular momentum is zero. The thermomagnetic hysteresis in the present case implies that the anisotropy comes from the ordered Fe moments. This also corroborates our assumption that the Fe atoms order first since the anisotropy starts at the first ordering itself, which is only due to Fe in the present case. The magnetic isotherm at 2 K (Fig. 5.17*b*) shows a saturation consistent with its ferromagnetic ordering. However, the saturation moment obtained is $5 \mu_B/f.u.$ which is more than the saturation moment of Fe ($2 \mu_B/f.u.$), but smaller than the saturation moment of Gd ($7 \mu_B/f.u.$). This clearly indicates that both Gd and Fe have ordered at 2 K. The only way to obtain this intermediate value is that the ferromagnetically ordered moments of Fe and Gd are aligned antiparallel to each other, resulting in a ferrimagnetic arrangement. The derivative plot of the susceptibility shows only one peak (inset of Fig. 5.17*a*). The most probable reason for the absence of the second peak is that the ordering of the Gd moments occurs at the same temperature as that of Fe.

The magnetic susceptibilities of other compounds are shown in Figs. 5.18*a* (Nd), 5.19*a* (Sm), 5.20*a* (Tb), 5.21*a* (Dy), 5.22*a* (Ho) and 5.23*a* (Er). All of them show peak in susceptibility corresponding to the magnetic ordering of Fe and a second peak in the derivative plot (except Er)

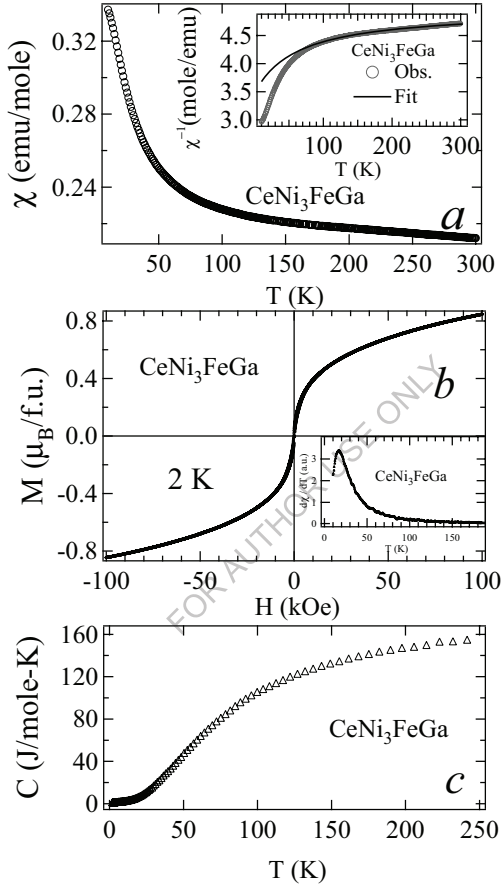


Fig. 5.15: Zero field cooled susceptibility (a), magnetic isotherm at 2 K (b) and the heat capacity curve (c) for $CeNi_3FeGa$. Inset of (a) shows the inverse susceptibility curve with a Curie Weiss fit. Inset of (b) depicts the derivative of susceptibility.

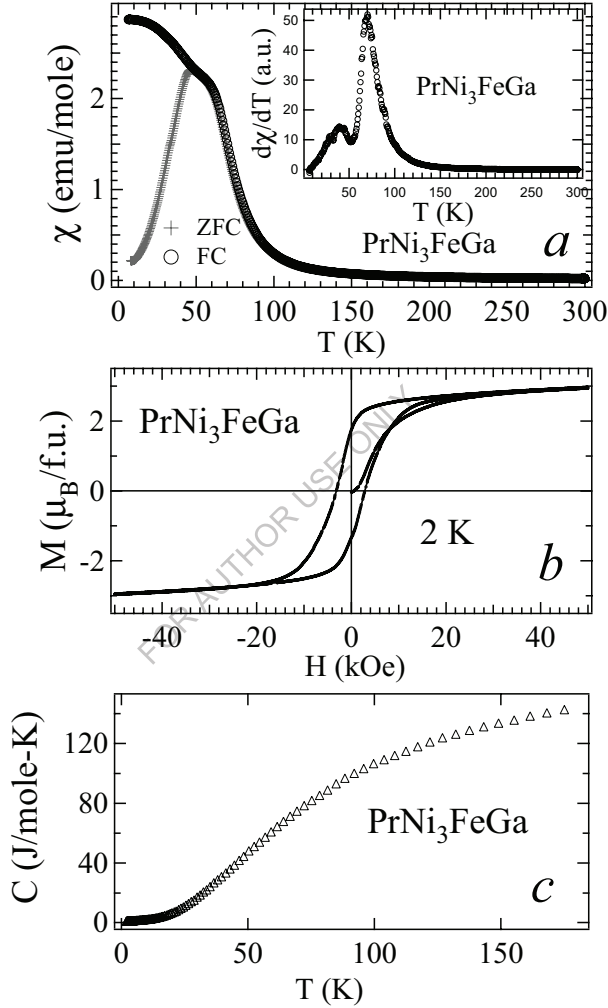


Fig. 5.16: Zero field cooled and field cooled susceptibility (a), magnetic isotherm at 2 K (b) and the heat capacity curve (c) for $PrNi_3FeGa$. Inset of (a) shows the derivative of susceptibility

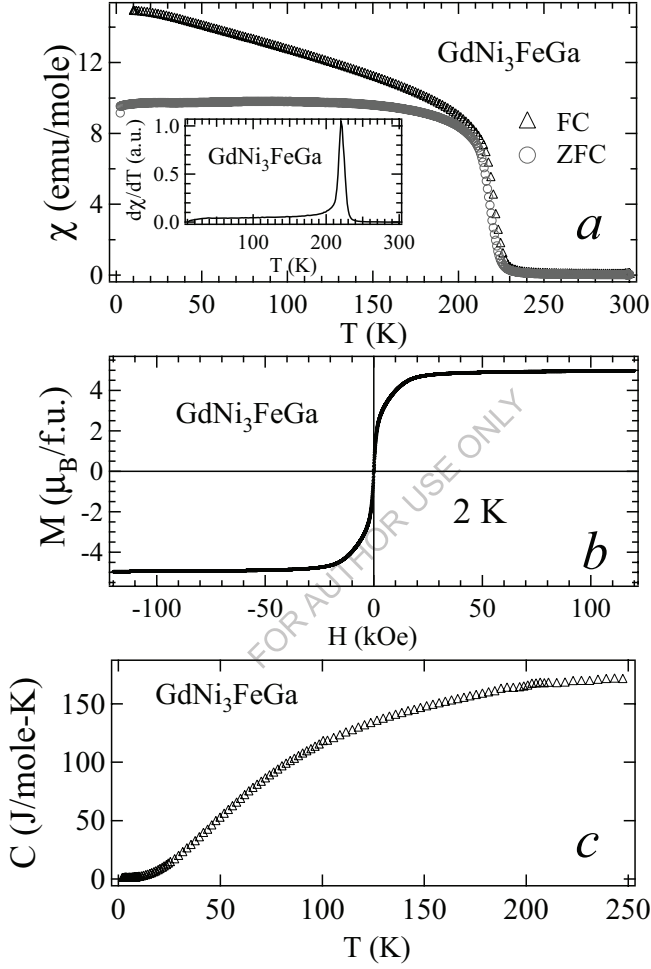


Fig. 5.17: Zero field cooled and field cooled susceptibility (a), magnetic isotherm at 2 K (b) and the heat capacity curve (c) for GdNi_3FeGa . Inset of (a) shows the derivative of susceptibility

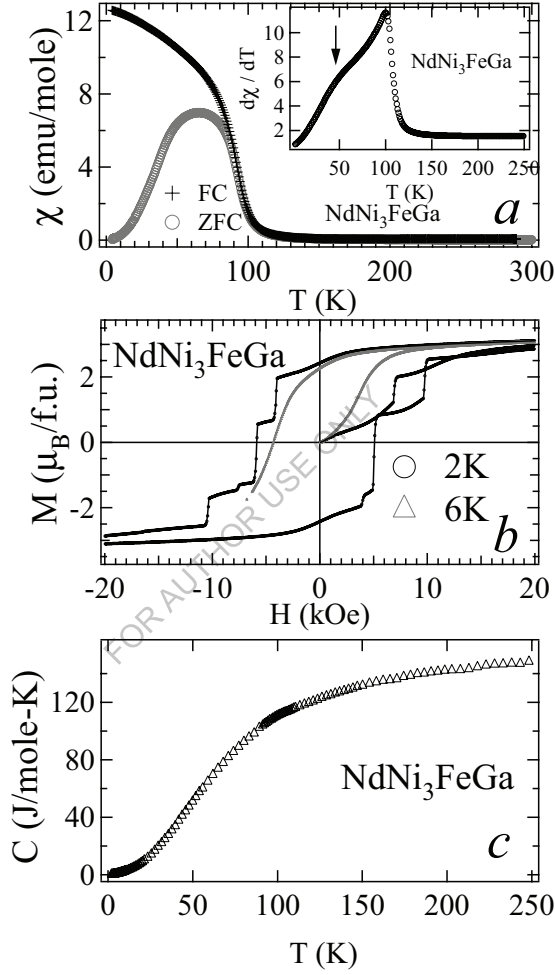


Fig. 5.18: Zero field cooled and field cooled susceptibility (a), magnetic isotherm at 2 K & 6 K (b) and the heat capacity curve (c) for $NdNi_3FeGa$. Inset of (a) shows the derivative of susceptibility

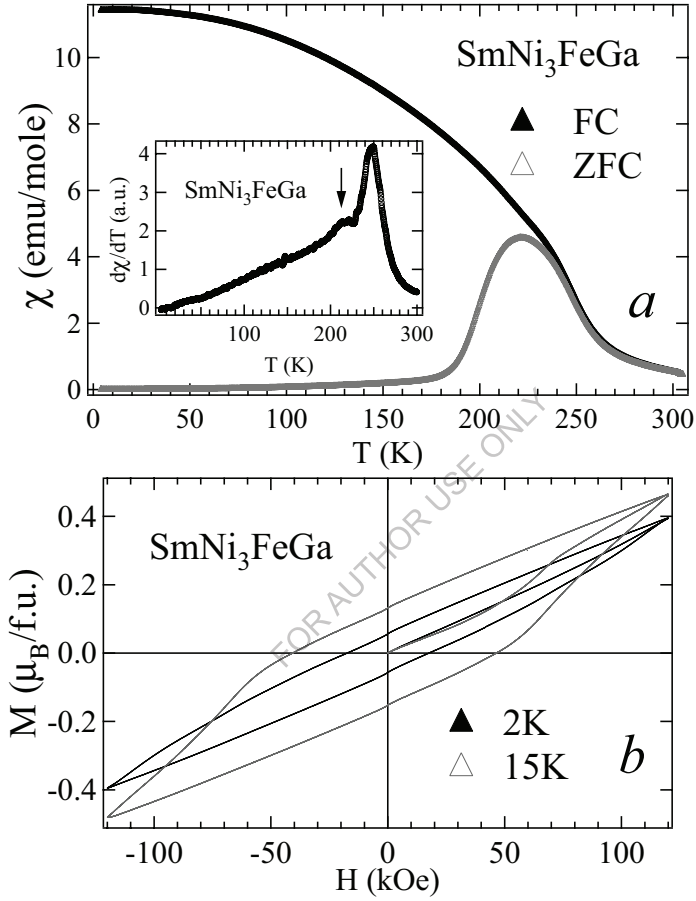


Fig. 5.19: Zero field cooled and field cooled susceptibility (a) and magnetic isotherm at 2 K & 15 K (b) for $SmNi_3FeGa$ Inset of (a) shows the derivative of susceptibility

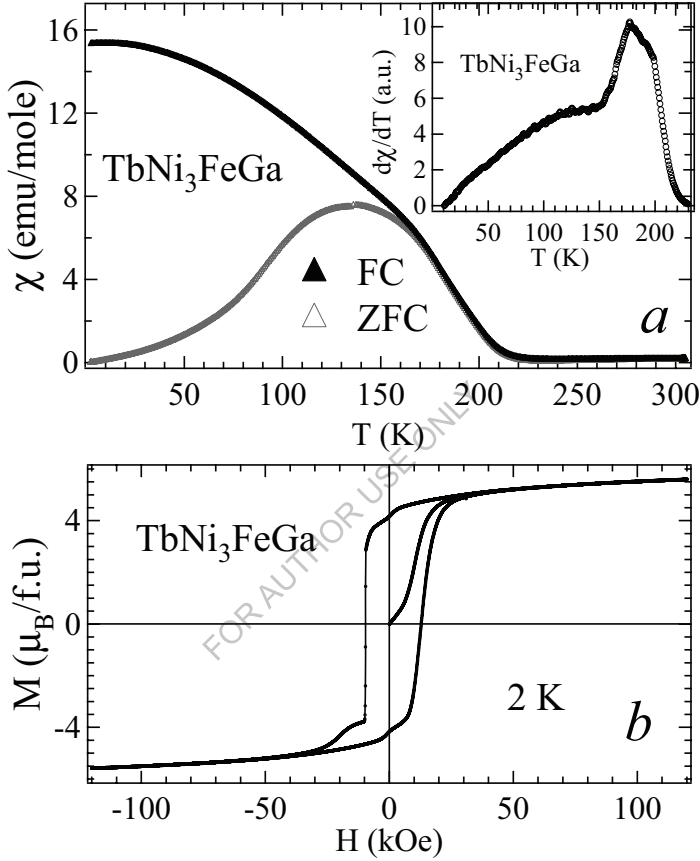


Fig. 5.20: Zero field cooled and field cooled susceptibility (a) and magnetic isotherm at 2 K (b) for $TbNi_3FeGa$. Inset of (a) shows the derivative of susceptibility

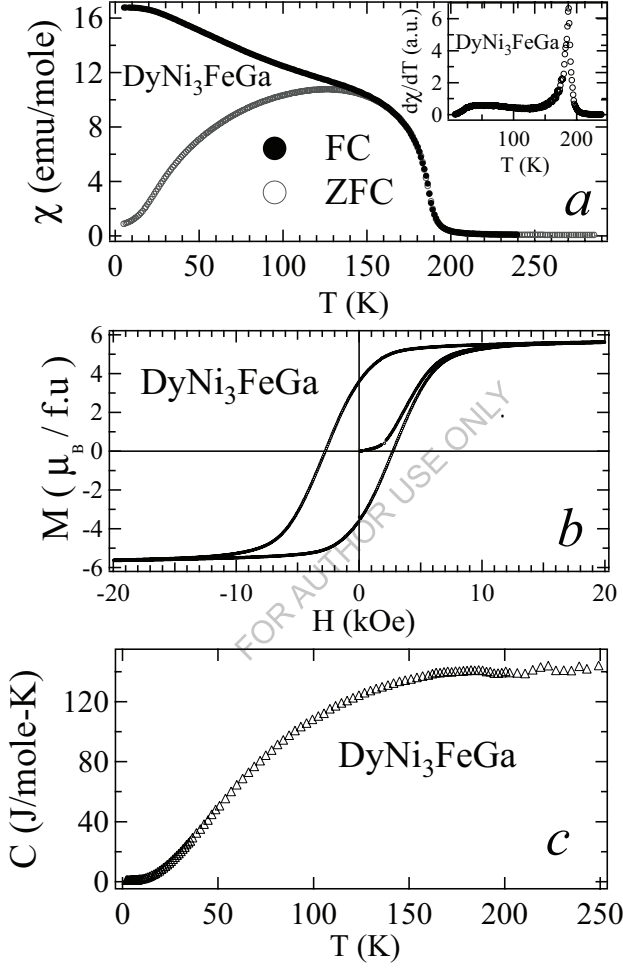


Fig. 5.21: Zero field cooled and field cooled susceptibility (a), magnetic isotherm at 2 K (b) and the heat capacity curve (c) for $DyNi_3FeGa$. Inset of (a) shows the derivative of susceptibility

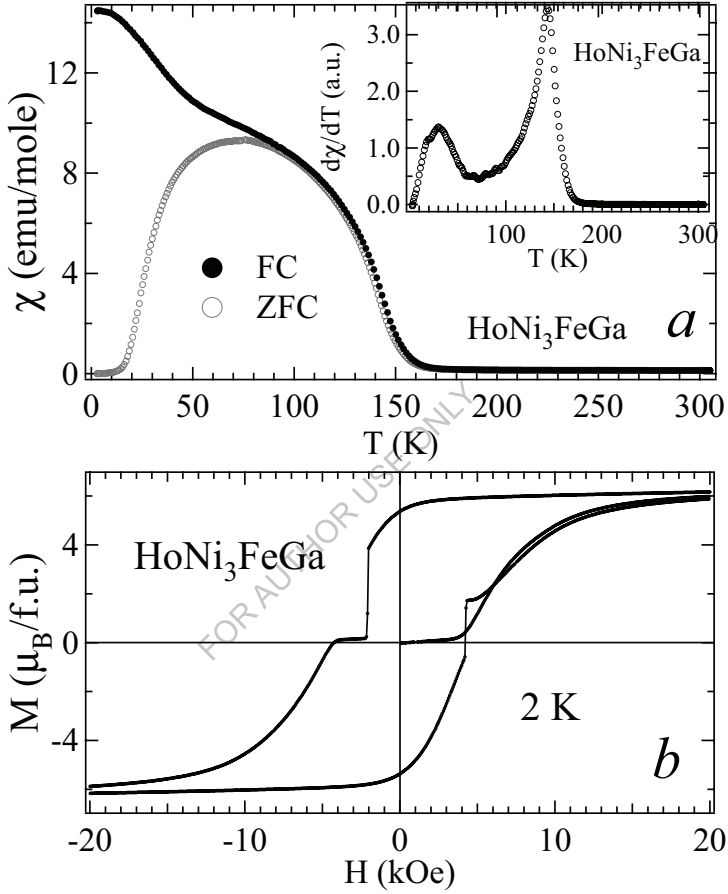


Fig. 5.22: Zero field cooled and field cooled susceptibility (a) and magnetic isotherm at 2 K (b) for $HoNi_3FeGa$. Inset of (a) shows the derivative of susceptibility

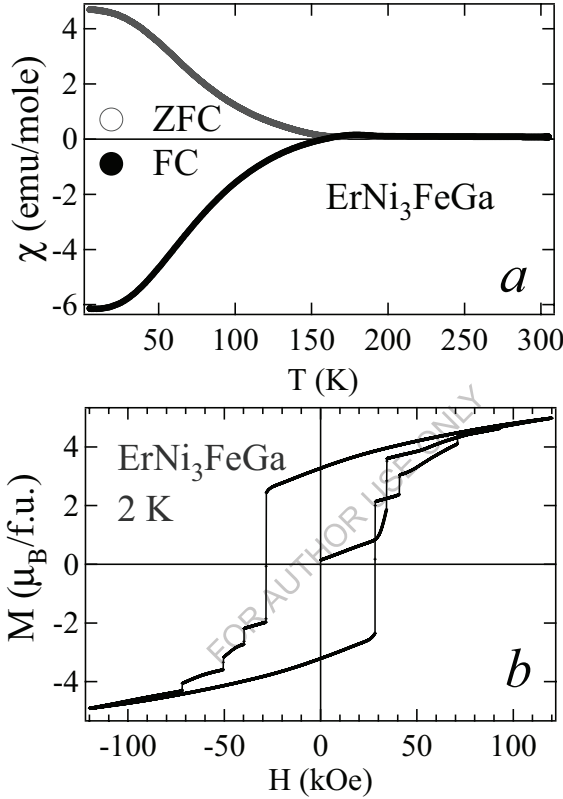


Fig. 5.23: Zero field cooled and field cooled susceptibility (a) and magnetic isotherm at 2 K for $ErNi_3FeGa$

where the rare earth moment ordering is assumed to take place. In the case of $SmNi_3FeGa$, the transition temperature (≈ 250 K) is even higher than the corresponding Gd compound. The reason is not clear because of the three different type of interaction present (between $R-R$, $T-T$ and $R-T$) [1]. The susceptibility behavior of $SmNi_3FeGa$ is a clear indication of the highly anisotropic behavior of the material. Sm^{3+} is highly anisotropic and it seems Fe ion has enhanced it. The susceptibility behaviour of $ErNi_3FeGa$ is very peculiar in the sense that the FC susceptibility

becomes negative below the magnetic ordering. This may be due to the spin compensation between the Fe and Er moments due to the high anisotropy involved and the details are given in the next section.

The magnetic isotherms of all the compounds show saturation, consistent with a ferromagnetic ordering. Multiple metamagnetic transitions are observed in the magnetic isotherms at 2 K for some of the compounds (Nd, Ho, Er, and Tb). The saturation moment obtained for $PrNi_3FeGa$ (Fig. 5.16*b*) and $NdNi_3FeGa$ (Fig. 5.18*b*) is more than that expected for the corresponding rare earth ions. This is because the Fe moments couple ferromagnetically with the rare-earth ion as expected for lighter rare earths [1]. In case of $NdNi_3FeGa$, the magnetization increases initially with field and undergoes a metamagnetic transition at ≈ 7 kOe and then moves towards saturation at high fields. During demagnetization (reverse cycle) the compound undergoes step like metamagnetic transitions. In all, there are four metamagnetic transitions at approximately -4 , -6 , -7.5 and -10.5 kOe, respectively. In the second forward magnetization cycle (5th quadrant), all the four metamagnetic transitions are present, but the three at ≈ 4 , 5 and 9.5 kOe are more prominent and the fourth one involves a small step ≈ 40 kOe (not shown). Magnetic isotherm at 6 K (≈ 2 quadrant curve) involves no metamagnetic transitions. This is also true for all the other compounds. Now since there are two magnetic ions present in the system, it is difficult to say which ion is involved in it. In case of $SmNi_3FeGa$, the shape of the $M-H$ curve (Fig. 5.19*b*) at 2 K looks like an elongated oval. The first quadrant (0 to 12 T) magnetization is nearly linear in field. This suggests that, a field of 120 kOe is not sufficient to push the domain walls out of the anisotropic energy barrier [7]. In such a case, a coercivity of 16 kOe occurs because of the highly anisotropic behavior of the compound, evident from the ZFC curve of magnetization vs temperature. The magnetic isotherm at 15 K shows an increase in the magnetization as well as an increase in the coercive field (≈ 40 kOe). This supports our explanation of insufficient energy to push the domain walls out of the anisotropic energy barrier at 2 K. Even at 15 K, the saturation is incomplete at 120 kOe. The complete saturation may occur still at a high temperature and then will decrease due to the temperature effects. This shows an increase in the anisotropy of the compound with Fe substitution. In case of $TbNi_3FeGa$ and $DyNi_3FeGa$ (Fig. 5.20*b* and 5.21*b*), the magnetization curves are as usual expected for a ferromagnet. The saturation magnetization obtained at 120 kOe is $6 \mu_B/f.u.$ and $5.6 \mu_B/f.u.$, respectively. The coercivity obtained is 10 kOe and 3 kOe, respectively. The curve of $TbNi_3FeGa$ is not symmetric about the axis due to a metamagnetic transition in the reverse leg of the magnetization. In case of $HoNi_3FeGa$, the initial magnetization

does not show a metamagnetic behavior but the magnetization in the 3rd and 5th quadrants shows a metamagnetic transition at ≈ 2 and 4 kOe, respectively. In case of $ErNi_3FeGa$ there are step like metamagnetic transitions at high fields. In the 3rd quadrant, it shows four metamagnetic transitions at 30, 40, 50 and 73 kOe and in the 5th quadrant, it shows at $\approx 30, 40, 70$ and 92 kOe. Here also the reason may be attributed to anisotropic behavior of the compound.

The heat capacity curves for the RNi_3FeGa series of compounds are shown along with their magnetic susceptibility figures. It is surprising to observe that the curves are smooth and do not involve any significant anomalies at the magnetic ordering temperatures. This is in contrast to the parent compounds where a lambda type anomaly appeared at the transition temperatures. The absence of the anomaly in the title compounds may be the slow variation of the entropy with temperature. Hence the peak is absent at the ordering temperature. Ordering of the Fe in the compound causes a high internal field which act on the rare earth ion and it also starts ordering slowly with decrease in temperature. Neutron diffraction studies are needed to ascertain the nature of magnetic ordering in these compounds and hence the absence of anomalies in the heat capacity.

5.3.3 Spin Compensation Behaviour of $ErNi_3FeGa$

In order to investigate the exact magnetic behaviour of the $ErNi_3FeGa$ compound, detailed magnetization measurements were carried out. The magnified view of the magnetization near the ordering temperature is shown in Fig. 5.24a. The FC magnetization in the ordered state (for fields ≤ 500 Oe) shows a broad hump followed by a null point where the magnetization is zero (called the compensation temperature T_{com}) and a negative magnetization below T_{com} down to the lowest temperature. At 600 Oe the magnetization at low temperatures increases to the positive value giving another null point at ≈ 121 K. Further increase in the field shifts the entire curve towards the positive magnetization side but the initial hump is now followed by a minima. It was found that the T_{com} shifted towards low temperatures with field. So to find out the exact null point, the magnetization data was taken in zero field after field cooling the sample down to 10 K (any temperature well below T_{com}) in the presence of a high field of 50 kOe and -50 kOe (Fig. 5.24b). The null point was found out to be 163 K. Similar behavior was also found in the case of $Sm_{1-x}Gd_xAl_2$ [8] and $Ho(Mn_{1-x}Fe_x)_{12}$ [9,10] systems. In case of the $Sm_{1-x}Gd_xAl_2$ system the reason for zero magnetization is the cancellation of orbital (Sm) and spin (Gd) moments and in the later case it is due to the moment cancellation arising from the negative coupling of Ho and (Fe,Mn) moments.

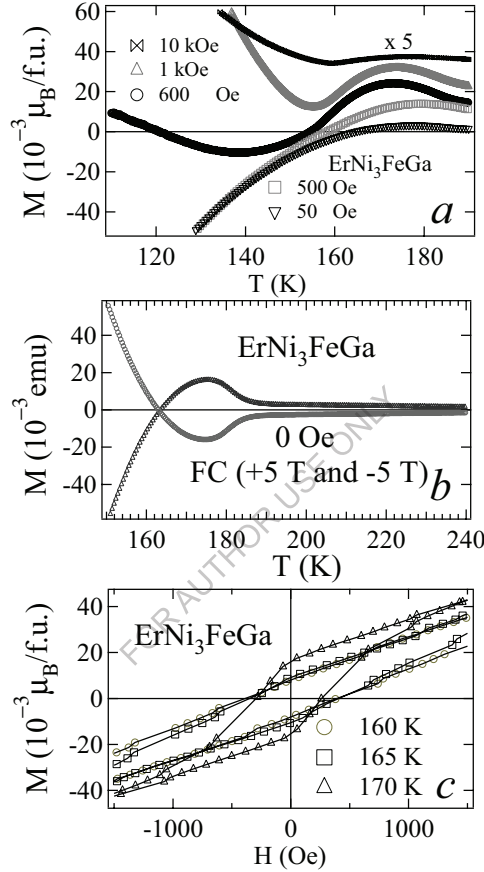


Fig. 5.24: Field cooled susceptibility near the transition at various applied fields (a), magnetization in zero field after cooling the sample in ± 50 kOe (b) and magnetic isotherm at various temperatures near the compensation temperature for (c) for $ErNi_3FeGa$. The 10 kOe curve in (a) is divided by 5 to show in the view.

Table 5.3: Comparison between the T_C s of RNi_4Ga and RNi_3FeGa series of compounds. Experimental saturation magnetization at 90 kOe and 2 K is compared with the expected value. Coercive Field for RNi_3FeGa at 2 K is given.

| R | RNi_4Ga | RNi_3FeGa | | | |
|-----------|-----------|-------------|-------------|------------------------------|------------------------------|
| | T_C (K) | T_C (K) | H_c (kOe) | $Exp. \mu_{sat}$ (μ_B) | $The. \mu_{sat}$ (μ_B) |
| La | P-P | 24 | N | 1.14 | 2 |
| Ce | P | P | N | 0.85 | 4.14 |
| Pr | P | 70 | 3.1 | 3.2 | 5.2 |
| Nd | 5 | 100 | 6 | 3.6 | 5.28 |
| Sm | 17 | 240 | 16 | 0.27 | 0.72 |
| Gd | 20 | 209 | N | 5 | 5 |
| Tb | 19 | 200 | 10 | 6.9 | 9 |
| Dy | 12 | 180 | 3 | 6.2 | 8 |
| Ho | 3.5 | 130 | 4.5 | 6.7 | 8 |
| Er | 8 | 190 | 28 | 6.5 | 7 |

P: Paramagnet

P-P: Pauli paramagnet

N: Negligible coercivity

Table 5.4: Comparison of the T_C of RNi_4Ga , RNi_3FeGa and RNi_3MnGa series of compounds. Experimental saturation magnetization at 90 kOe and 2 K compared with the expected value. Coercive Field for RNi_3MnGa and RNi_3FeGa at 2 K is given.

| R | RNi_4Ga | RNi_3MnGa | | | | RNi_3FeGa | | | |
|-----------|--------------|--------------|----------------|----------------------------|----------------------------------|--------------|----------------|----------------------------|----------------------------------|
| | T_C (K) | T_C (K) | H_c (kOe) | μ_{sat} (μ_B) | μ_{sat} (th.) (μ_B) | T_C (K) | H_c (kOe) | μ_{sat} (μ_B) | μ_{sat} (th.) (μ_B) |
| La | P-P | 28 | N | 1.14 | 2 | 24 | N | 1.14 | 2 |
| Ce | P | 21 | N | - | 4.14 | P | N | 0.85 | 4.14 |
| Pr | P | 56 | 21 | 3.2 | 6.2 | 70 | 3.1 | 3.2 | 5.2 |
| Nd | 5 | 85 | 8 | 3.0 | 6 | 100 | 6 | 3.6 | 5.28 |
| Sm | 17 | - | - | - | - | 240 | 16 | 0.27 | 0.72 |
| Gd | 20 | 130 | N | 5 | 4 | 209 | N | 5 | 5 |
| Tb | 19 | 137 | 22 | 3.6 | 6 | 200 | 10 | 6.9 | 9 |
| Dy | 12 | 95 | 2.5 | 5.8 | 7 | 180 | 3 | 6.2 | 8 |
| Ho | 3.5 | - | - | - | - | 130 | 4.5 | 6.7 | 8 |
| Er | 8 | - | - | - | - | 190 | 28 | 6.5 | 7 |

We attribute the behavior of the $ErNi_3FeGa$ arising due to the latter effect. The feature observed in the magnetization curve can be explained on the basis of the ferrimagnetic coupling between the Er and Fe moments. When the sample is field cooled (low field ≤ 500 Oe) from its paramagnetic state, at ≈ 190 K the Fe ions order ferromagnetically in the direction of the field. Now due to the rare earth transition metal exchange coupling, the Er ion will also start ordering negatively to the Fe moments. The competing nature of both the moments results in a peak, there after the larger Er moments take over and the magnetization decreases. So as the temperature is further decreased, at T_{com} , both the moments become equal in magnitude and hence the resultant magnetization is zero. Below T_{com} , the magnetization is negative because of the ordered Er moments against the field. The Er moments are not able to go with the field because the field energy (it also depends upon the net moment on the Er ion) is unable to overcome the anisotropic energy barrier on the Er ion. It is to be noted that the effect of both the energies increases with decrease in the temperature. Now when the field is increased (600 Oe) the competitive effects between the anisotropic and field energies give rise to a minima in the negative magnetization after which it moves towards a positive value, resulting in another compensation temperature T'_{com} at ≈ 121 K (for $H = 600$ Oe in Fig. 5.24a). For higher fields (1 kOe and 10 kOe), the entire magnetization curve shifts to the positive magnetization region but because of the high anisotropic energy in the neighborhood of the ordering temperature, the magnetization does not go to zero, but increases after going through a minimum. The magnetic isotherms taken around the null point (163 K) are shown in Fig. 5.24c. It is clear that the magnetization increases at 170 K compared to that at 160 K or 165 K in contrast to a normal ferromagnetic behaviour. This increase is due to the dominant ordered Fe moments, where as at 160 K and 165 K there is contribution from both Er and Fe ions which are negatively aligned to each other. A similar behavior could not be found in case of other RNi_3FeGa compounds ($R = Dy, Tb$ and Ho) even though all of them have ferrimagnetic type ordering between the Fe and the rare earth moments. This may be because the anisotropic energy at the rare earth is much less compared to the magnetic energy at or in the neighborhood of the ordering temperature. So the external field shifts the rare earth moment in its direction.

5.3.4 RNi_3MnGa ($R = Ce, Pr, Nd, Gd, Tb, Dy$ and Ho):

The magnetic behaviour of the Mn substituted magnetic rare earth compounds is almost similar to the Fe substituted compounds. All of them show a magnetic ordering much higher compared to that of the unsubstituted RNi_4Ga series of compounds. Here also we assume that

the Mn atoms order first at high temperatures due to the direct exchange interaction between the Mn atoms and forces the rare earth moments to order later. The susceptibilities at 500 Oe as a function of temperature for RNi_3MnGa are shown in Figs. 5.25-5.30. All the compounds show thermomagnetic irreversibility in the ordered state. The transition temperatures are given in Table 5.4. Comparing the transition temperatures with the corresponding Fe counterparts, it is found that the T_C of the Fe compounds is larger compared to the Mn compounds (except La and Ce). This shows that the interactions are stronger in the RNi_3FeGa compounds.

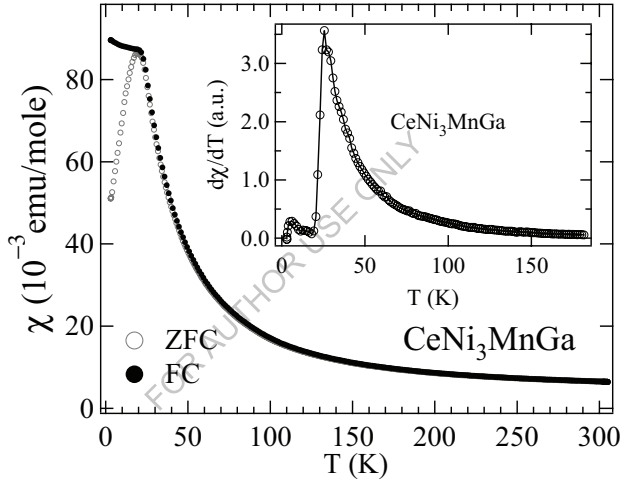


Fig. 5.25: Zero field cooled and field cooled susceptibility for $CeNi_3MnGa$ Inset shows the derivative of susceptibility

$CeNi_3MnGa$ orders magnetically at 21 K (Fig. 5.25a). Since the Ce atoms are found in the valance fluctuating state (evident from the Lanthanide contraction of the unit cell volume), the magnetic ordering is presumed to be due to the Mn atoms. This observation is in contrast to that observed in the Fe substituted compound $CeNi_3FeGa$, which has only an onset of ferromagnetic ordering down to 2 K. The exact reason for such a behavior is not known but it is possible that the effective valency of Ce in the Mn substituted compound is more close to $3+$, where as it is close to $4+$ in the Fe substituted compound. In that case, the extra electron can kill the magnetic state of Fe completely. In case of $PrNi_3MnGa$ the ferromagnetic ordering temperature is 56 K.

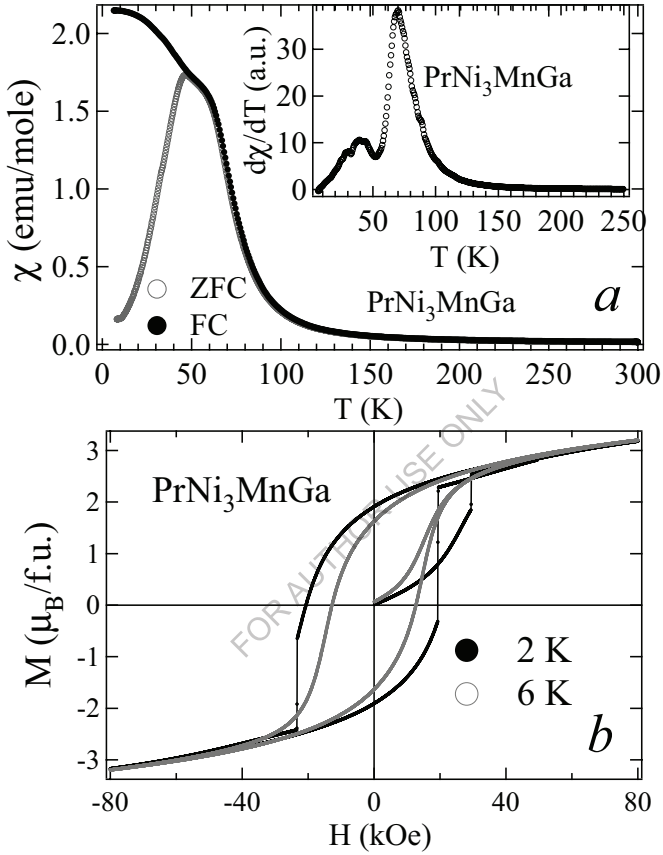


Fig. 5.26: Zero field cooled and field cooled susceptibility (a) and magnetic isotherm at 2 K & 6 K (b) for $PrNi_3MnGa$. Inset of (a) shows the derivative of susceptibility

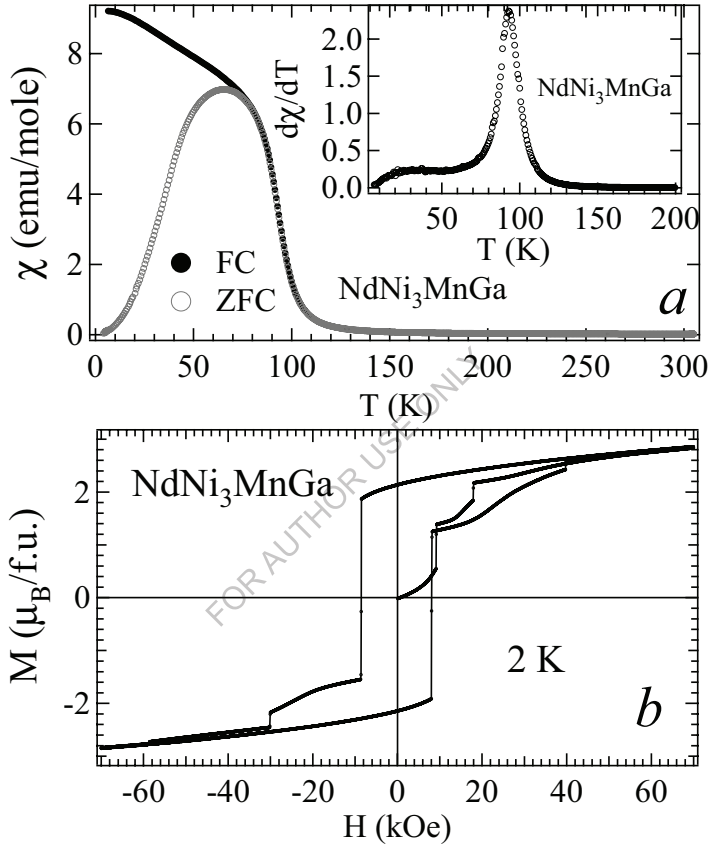


Fig. 5.27: Zero field cooled and field cooled susceptibility (a) and magnetic isotherm at 2 K (b) for $NdNi_3MnGa$. Inset of (a) shows the derivative of susceptibility

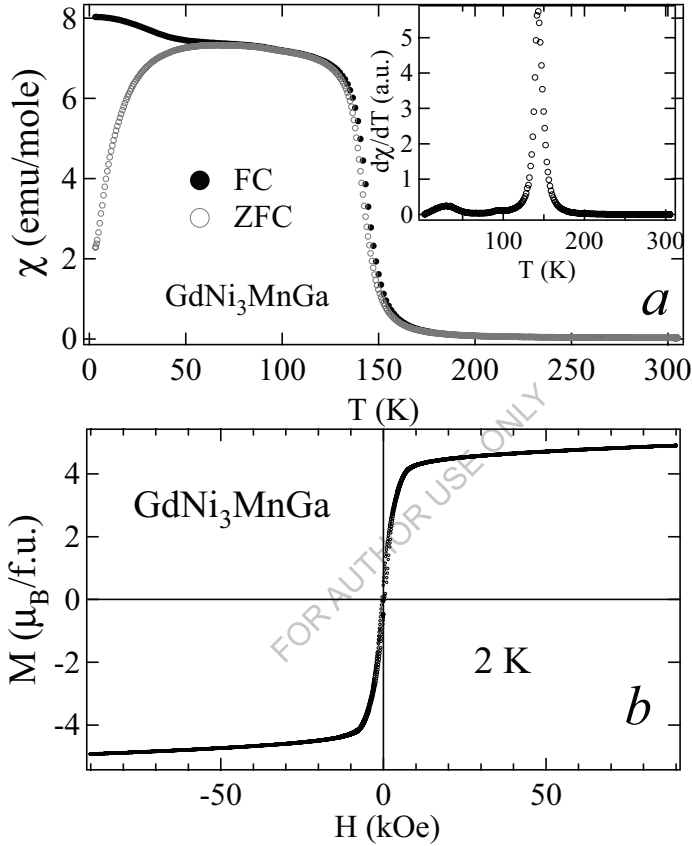


Fig. 5.28: Zero field cooled and field cooled susceptibility (a) and magnetic isotherm at 2 K (b) for $GdNi_3MnGa$. Inset of (a) shows the derivative of susceptibility

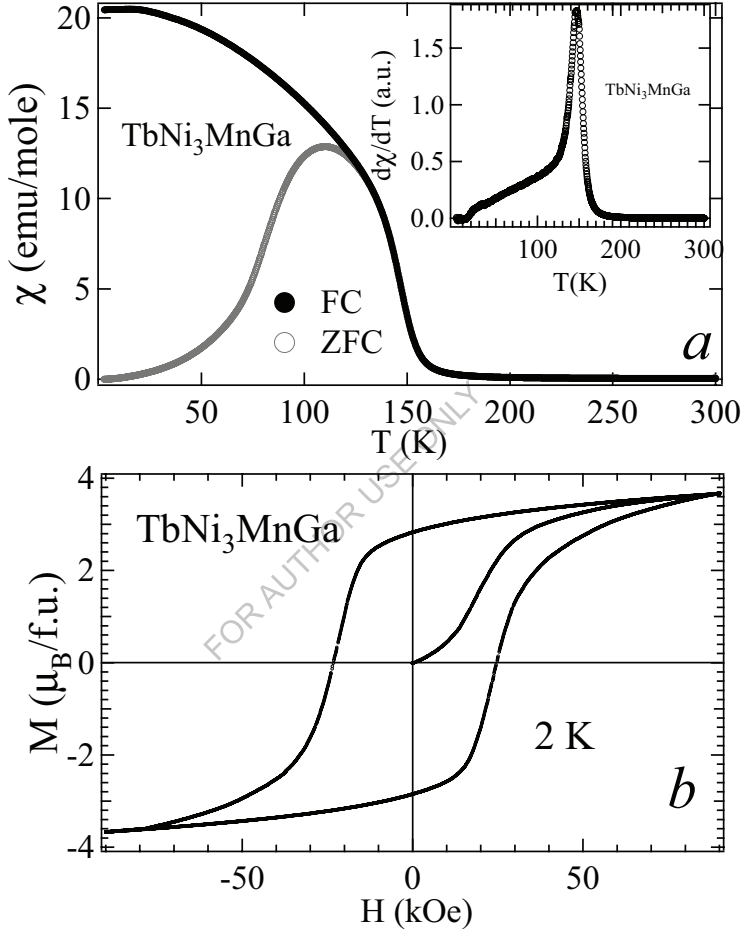


Fig. 5.29: Zero field cooled and field cooled susceptibility (a) and magnetic isotherm at 2 K (b) for $TbNi_3MnGa$. Inset of (a) shows the derivative of susceptibility

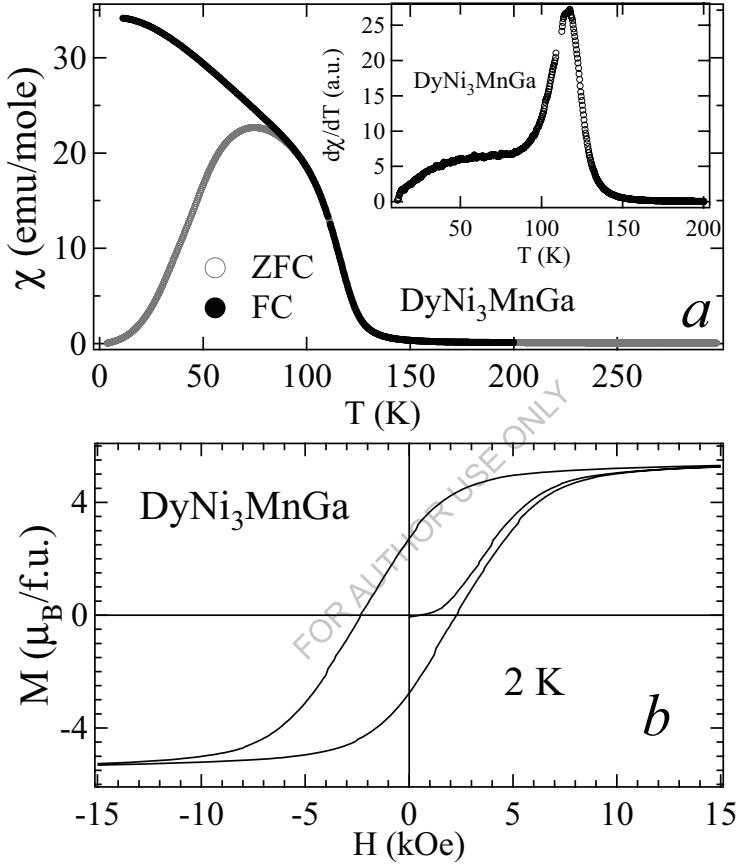


Fig. 5.30: Zero field cooled and field cooled susceptibility (a) and magnetic isotherm at 2 K (b) for $DyNi_3MnGa$. Inset of (a) shows the derivative of susceptibility

The derivative of the DC susceptibility (inset of Fig. 5.26a) shows an extra peak at ≈ 40 K, which can be assumed to be due to the ordering of the Pr moments. In rest of the compounds, a broad hump appears below T_c in the derivative plots, and it can be considered to be due to the ordering of the rare earth moments over a range of temperature. The susceptibility behavior of all the compounds is as expected, except for $GdNi_3FeGa$. There is a large separation in the susceptibility measured under the ZFC and FC conditions. In case of $GdNi_4Ga$ both of them coincided with each other and in case of $GdNi_3FeGa$ there was a small separation between them. The increase in the separation between the FC and ZFC curves indicates an increase in the anisotropy of the compound compared to the other two. Another interesting observation in case of $GdNi_3MnGa$ is that the susceptibility between the transition temperature (≈ 150 K) and the temperature where FC and ZFC separates is nearly temperature independent.

For the further analysis of the obtained susceptibility results, the magnetization of the compounds at 2 K was measured. The saturation magnetization and coercive field obtained are given in Table 5.4. The coercive field increases and the saturation magnetization decreases in almost all the compounds compared to the Fe doped compounds. Such a behavior arises when the anisotropy of the compound increases [11]. $PrNi_3MnGa$ shows metamagnetic transitions at 25 kOe, -23 kOe and 20 kOe (Figs. 5.26b). Such a behavior was absent in case of $PrNi_3FeGa$. The increase in temperature suppresses the metamagnetic behavior in the compound, as seen from the magnetic isotherm at 6 K. In case of $NdNi_3MnGa$ there are step like metamagnetic transitions similar to that observed in case of $NdNi_3FeGa$. In case of $GdNi_3FeGa$ the magnetization isotherm at 2 K (Figs. 5.28b) increases with field even at 9 T with a moment of $5 \mu_B/f.u.$ $DyNi_3MnGa$ and $TbNi_3MnGa$ also show a reduced moment compared to the corresponding Fe compounds. The possible reason is attributed to the anisotropic behavior of the Mn in the compound, which does not possess the full moment in the ordered state.

5.4 Summary:

We have synthesized and studied the magnetic properties of the pseudo ternary gallides RNi_3FeGa and RNi_3MnGa (R = rare earths). These compounds form as substitutional variants of parent RNi_4Ga compounds. Here Fe and Mn show equal priority to the two different Ni sites in RNi_4Ga structure. The lattice parameters show a marginal increase compared to the parent compounds RNi_4Ga . The lattice parameters of Mn compounds are larger than compared to the Fe compounds. YNi_3FeGa and YNi_3MnGa show a spin glass type behavior. $LaNi_3FeGa$ and

$LaNi_3MnGa$ show anisotropic ferromagnetic behavior at low temperatures. RNi_3FeGa compounds with other magnetic rare earths undergo ferromagnetic transitions below room temperature. The transition temperatures are much higher compared to their parent compounds RNi_4Ga . This is due to the magnetic nature of Fe in the compound lattice. $SmNi_3FeGa$ has the highest transition temperature among the series. It also shows a highly anisotropic behavior. All the compounds show thermomagnetic irreversibility in the ordered state. $ErNi_3FeGa$ shows zero magnetization followed by negative magnetization in low field in the ordered state under field cooled condition. The magnetic isotherm at 2 K for RNi_3FeGa compounds shows that the lighter rare earths couple ferromagnetically with the transition elements and the heavier rare earths couple antiferromagnetically. $NdNi_3FeGa$ and $ErNi_3FeGa$ show step like metamagnetic transitions in their magnetic isotherm at 2 K. In case of RNi_3MnGa compounds the saturation moments are less compared to that of the corresponding Fe doped compounds. The coercivity of these compounds increases compared to the RNi_3FeGa series of compounds. All these behavior can be attributed to the increased anisotropy of the compound with Mn doping.

5.5 References:

1. K.H.J. Buschow, *Rep. Prog. Phys.*, **40** (1977) 1179.
2. Devang A. Joshi, C.V. Tomy, R. Nagarajan, and S.K. Malik, *Solid State Comm.*, **13** (1999) 225.
3. J.-L. Bobet, S. Pechev, B. Chevalier and B. Darriet, *J. Alloys Compd.*, **267** (1998) 136.
4. H. Flandorfer, P. Rogl, K. Hiebl, E. Bauer, A. Lindbaum, E. Gratz and C. Godart, *Phys. Rev. B*, **50** (1994) 15527.
5. J. A. Mydosh, *Spin Glass* (Taylor and Francis).
6. C.N. Guy, *J. Phys. F: Metal Phys.* **8** (1978) 1309.
7. B.D. Cullity, *Introduction to Magnetic Materials*, (Addison-Wisley Pub. Co. 1972.).
8. H. Adachi, H. Kawata, H. Hashimoto, Y. Sato, I. Matsumoto and Y. Tanaka, *Phys. Rev. Lett.*, **87** (2001) 1.
9. W. Mao, J. Yang, B. Chang, Y. yang, *Solid State Comm.* **109** (1999) 655.
10. J. B. Yang, W. B. Yalon, W.J. James, S. Cai, D. Eckert, A. Eckert, K.H. Muller and Y.C. Yang, *Phys. Rev. B*, **65** (2002) 064444.

Chapter 6

Conclusion

We have studied the magnetic behavior of ternary rare earth indides $R_2\text{CoIn}_8$ and rare earth gallides $R\text{Ni}_4\text{Ga}$, $R\text{Ni}_3\text{FeGa}$ and $R\text{Ni}_3\text{MnGa}$. A brief summary of the important results is as follows.

6.1 Ternary Indide $R_2\text{CoIn}_8$

- $R_2\text{CoIn}_8$ compounds form with $R = \text{Ce, Pr, Nd, Sm, Gd, Tb, Dy, Ho}$ and Y . The compounds form in Ho_2CoGa_8 type tetragonal structure with a space group $P4/mmm$. The lattice parameters are such that the $c/a \sim 3$. Rare earth and Cobalt atoms occupy crystallographic sites $2g$ and $1a$, respectively with occupancy 2 and 1. Indium atoms occupy sites $2e$, $2h$ and $4i$ with occupancy 2, 2 and 4, respectively.
- The nonmagnetic Y compound (Y_2CoIn_8) shows a Pauli-paramagnetic behavior. The heat capacity and resistivity behavior of the compound also shows a behavior similar to that expected for a nonmagnetic compound. These results confirm a nonmagnetic behavior of Co in these compounds.
- Ce_2CoIn_8 is a heavy fermion superconductor with a transition temperature of 0.4 K. The electronic contribution to the heat capacity (γ) comes out to be 480 mJ/mole-K. The effective mass of the conduction electron was calculated to be $55 m_e$, where m_e is the mass of the electron. The resistivity behavior of the compound reflects a dominant Kondo behavior at high temperatures (above ≈ 40 K) and a non Fermi liquid behavior at low temperatures (down to 2 K).
- Pr_2CoIn_8 does not show any magnetic ordering down to 2 K, but shows dominant crystal field effects at low temperatures. The crystal field fit to the inverse susceptibility yields the following energy levels with their corresponding degeneracy.

| Energy (K) | 0 | 33 | 35 | 53 | 64 | 68 | 94 |
|------------|---|----|----|----|----|----|----|
| Degeneracy | 2 | 1 | 1 | 1 | 2 | 2 | 2 |

The ground state was found to be a nonmagnetic doublet which occurs very rarely.

- Compounds with the rest of the magnetic rare earths order antiferromagnetically at low temperatures. The effective moment of Gd in the compound which is least affected by crystal field compares well with the theoretical value ($7.9 \mu_B$), and hence we can assume that the Co atoms do not contribute to the magnetic properties of the compounds.

- ▶ Magnetization results of Sm_2CoIn_8 show an effect of a ferromagnetic component below the ordering temperature. The behavior is attributed to the incomplete cancellation of antiferromagnetically ordered spins. Magnetic isotherm at 2 K shows that the compound remains in the field induced metamagnetic state even if the field is reduced to zero. This behavior is attributed to the highly anisotropic behavior of the Sm^{3+} ions. The effect of the ferromagnetic component is dominant only in the magnetization measurements. Heat capacity and resistivity behavior of the compounds are consistent with a dominant antiferromagnetic phase.
- ▶ In case of Gd_2CoIn_8 , the magnetic ordering temperature hardly shows any shift with magnetic field. In addition to this, a large negative Curie temperature suggests a strong antiferromagnetic interaction present in the compound. The resistivity behavior of the compound shows a T^2 variation in the ordered state, in contrast to a T^3 variation expected for an isotropic antiferromagnet.
- ▶ Magnetization measurements on Tb_2CoIn_8 show the possibility of a complex magnetic structure with dominating antiferromagnetic interactions. The heat capacity and resistivity measurements also support the result. The compound also shows an unexpectedly high magnetoresistance at 2 K ($\approx 2500\%$).
- ▶ Dy_2CoIn_8 shows an additional magnetic transition (≈ 5 K) below the ordering temperature in magnetization, specific heat and resistivity measurements. This effect is due to the spin reorientation of the Dy moments below the ordering temperature. This effect was also proved by fitting the resistivity curve of the compound in the ordered state. The transition temperature shifts appreciably with field (≈ 0.05 K/kOe) indicating a weak coupling between the ordered moments. At 2 K the compound undergoes two metamagnetic transitions at 28 kOe and 83 kOe. It was also found that the magnetoresistance of the compound at 2 K decreases with field above 83 kOe. This implies that the second metamagnetic transition at 83 kOe and 2 K drives the compound to a field induced ferromagnetic state.
- ▶ Ho_2CoIn_8 shows an antiferromagnetic transition at 7.5 K. The transition shifts appreciably with field (≈ 0.05 K/kOe) indicating a weak interaction between the ordered moments. Similar effect is also reflected in the heat capacity behavior of the compound. The compound shows two field induced magnetic transitions (at 25 kOe and 55 kOe) at 2 K. The magnetoresistance behavior of the compound shows that at ≈ 55 kOe the compound undergoes a field induced ferromagnetic transition.

6.2 Ternary Gallides (RNi₄Ga)

This series forms as a substitutional variant of the well known RNi₅ series of compounds.

- ▶ RNi₄Ga compounds form in a CaCu₅ type hexagonal structure with a space group $P6/mmm$. Within a unit cell, the rare earth atoms occupy crystallographic $1a$ site with occupancy 1, Ni atoms occupy $2c$ and $3g$ sites, both with occupancy 2. However, when Ga is substituted for Ni, it occupies only the $3g$ site. Since the large rare earth atoms also occupy the plane containing the $2c$ site, the large metallic radii of Ga atom (1.41 Å) compared to Ni (1.24 Å) may prevent it from occupying the $2c$ site.
- ▶ The unit cell volume of the compounds decreases as we go from La to Lu (except for Ce) in agreement to the well known lanthanide contraction of the rare earth elements. The unit cell volume of Ce deviates from the normal behavior because of the mixed valent behavior of the Ce (Ce³⁺ and Ce⁴⁺) in the compound. This also suggests a unique valency (R^{3+}) for the other rare earths in the series.
- ▶ The unit cell volume increases compared to that of the parent compound due to the large size of Ga compared to Ni.
- ▶ The nonmagnetic La and Lu compounds show Pauli-paramagnetic behavior similar to that of their parent compounds. This shows a nonmagnetic behavior of Ni in this series of compounds.
- ▶ The heat capacity of LaNi₄Ga could be fitted to pure electronic (with $\gamma = 12$ mJ/mole-K) and phonon ($\theta_D = 292$ K) contributions as expected for a nonmagnetic compound.
- ▶ CeNi₄Ga and PrNi₄Ga show a paramagnetic behavior down to 2 K.
- ▶ The Curie-Weiss fit to the susceptibility of Ce compound yields $\mu_{eff} = 0.8 \mu_B$ (less than $2.54 \mu_B$, expected for Ce³⁺ ion). The reason is due to the mixed valent behavior (Ce⁴⁺ is nonmagnetic) of Ce in the compound.
- ▶ PrNi₄Ga shows no magnetic ordering, behavior similar to that of the parent compound PrNi₅, due to the crystal field effects.
- ▶ Compounds with rest of the rare earths order ferromagnetically at low temperatures.
- ▶ The transition temperature decreases compared to that of the parent compound. The reason is attributed to the decrease in the absolute value of the conduction electron polarization responsible for the RKKY interaction.

- ▶ The transition temperature of SmNi_4Ga and TbNi_4Ga deviates appreciably from the values that are expected from the de-Gennes scaling. The reason may be attributed to the crystal field effects.
- ▶ All the compounds show anisotropic magnetic behavior except GdNi_4Ga .
- ▶ At 2 K, GdNi_4Ga shows saturation magnetization more than the theoretically expected value. The extra contribution is attributed to the polarization of the conduction electrons and possible filling up of the $3d$ band.
- ▶ GdNi_4Ga shows the possibility of helical magnetic structure in the ordered state at low fields.
- ▶ The coercive field obtained for all the compounds was negligible except for SmNi_4Ga ($H_c = 40$ kOe) and TbNi_4Ga ($H_c = 2$ kOe) due to high anisotropy.
- ▶ High coercivity in SmNi_4Ga is attributed to the presence of narrow domain walls. A rough estimate of the thickness of the domain walls calculated from the temperature dependence of H_c comes out to be 8 \AA .

6.3 Pseudo Ternary Gallides (RNi_3FeGa and RNi_3MnGa)

The nonmagnetic behavior of Ni in RNi_4Ga series of compounds motivated us to see the effect on other magnetic $3d$ elements within the lattice. RT_5 ($T = 3d$ elements) series of compounds are well known to form magnetic compounds with Co, so we selected Fe and Mn for which the series (RT_5) do not form compounds. Our discussion is mainly focused on the magnetic properties these compounds.

- ▶ RNi_3FeGa compounds form as melted, where as RNi_3MnGa compounds require annealing. This indicates a less solubility of Mn in this compounds compared to Fe.
- ▶ RNi_3MnGa and RNi_3FeGa forms in a CaCu_5 type hexagonal structure with a space group $P6/mmm$, maintaining the structure of the parent compound.
- ▶ Both Fe and Mn have equal preference to $2c$ and $3g$ sites. This may be due to the comparable size of Ni (1.24 \AA), Fe (1.26 \AA) and Mn (1.28 \AA). The unit cell volume has increased compared to the parent compounds. The unit cell volume of Mn compounds is larger than that of the Fe compounds. The reason may be due to the larger size of Mn compared to Fe.
- ▶ In both the series of compounds the unit cell volume follows the lanthanide contraction except for Ce compounds. This implies that Ce is mixed valent in both the series.

- ▶ Y and La compounds in both the series (with Fe and Mn) show magnetic ordering at low temperatures. This shows that both Mn and Fe retain the magnetic behavior in the compound (assuming Ni is nonmagnetic).
- ▶ Fe shows a moment of $1.2 \mu_B/\text{f.u.}$ at 90 kOe in both the Y and La compounds.
- ▶ Mn shows a moment of $3.4 \mu_B/\text{f.u.}$ in case of Y compound, where as $2.8 \mu_B/\text{f.u.}$ in case of La compound.
- ▶ Y compounds in both the series show spin glass behavior at low temperatures.
- ▶ La compounds show anisotropic ferromagnetic behavior at low temperatures.
- ▶ CeNi_3FeGa does not show magnetic ordering down to 2 K, where as CeNi_3MnGa orders ferromagnetically at 23 K. However, an indication of onset of magnetic ordering is seen in Fe compound at ≈ 15 K.
- ▶ Compounds of Fe and Mn with rest of the rare earths show a ferromagnetic ordering at very high temperatures compared to their parent compound RNi_4Ga .
- ▶ The ferromagnetic ordering temperature increases due to the ordering of the substituted ions at high temperature in the compound.
- ▶ GdNi_3FeGa and GdNi_3MnGa show anisotropic behavior in contrast to the isotropic behavior of GdNi_4Ga . The anisotropy is induced by the substituted Fe and Mn ions.
- ▶ SmNi_3FeGa shows a highly anisotropic behavior with a large ferromagnetic ordering temperature of 240 K (maximum of all the investigated compounds). The coercivity obtained at 15 K is 40 kOe. The compound could not be formed in single phase with Mn.
- ▶ NdNi_3FeGa , NdNi_3MnGa , PrNi_3MnGa and ErNi_3FeGa show step like metamagnetic transitions at 2 K.
- ▶ The most interesting part of the study in both the series of compounds is the spin compensated ferrimagnetic behavior exhibited by ErNi_3FeGa . The reason is due to the ferrimagnetic ordering of the Er and Fe moments. The anisotropic energy at the ordering temperature is high, preventing the Er moments to proceed in the direction of field (field < 500 Oe) during its onset of ordering and remains negative to the ordered Fe moments (in the direction of field).

6.4 Future Plans

Polycrystalline ternary intermetallics R_2CoIn_8 series of compounds exhibits a variety of interesting properties. Except Ce, and Pr compounds, the rest of the compounds require a detail investi-

gation looking into both the low temperature heat capacity and the transport behavior of the compound. Er compound is a challenge since it is reported to form in single phase but our three trials failed. In this series each compound is interesting in itself, so to know a exact behavior at atomic level, a single crystal study with Neutron diffraction is required for all the compounds. Since Co is found to be nonmagnetic in this series of compound, a substitutional study with Fe and Ni (neighbors of Co) would be a best option for magnetic study.

RNi₄Ga series with its substitutions (Fe and Mn) are required to be explored using the transport characteristic of the compounds. The magnetic behavior itself in case of substituted compounds is not fully explained. A wide literature survey would help to explain the present magnetic properties of all the compounds. A single crystal study is must for all the compounds, since it helps to dig out its original behavior. Spin compensation study in Gd doped ferromagnetic Sm compounds has (SmAl₂) has produced many interesting results. In our compounds Sm_{1-x}Gd_xNi₄Ga is an ideal candidate for this study since both of them have ferromagnetic ordering at low temperatures (17-20 K).

ErNi₃FeGa compound shows spin compensation type behavior. Detailed investigations can be carried out in this compound. SmNi₃FeGa shows even a higher magnetic ordering compared to GdNi₃FeGa compound. This will be another ideal consideration to study the spin orbital compensation by substituting small amounts of Gd in SmNi₃FeGa compound.

Acknowledgements

It is my pleasure to express sincere gratitude to my supervisor Prof. C.V. Tomy for his effective guidance, suggestions, and technical discussions during the course of my research work. His teachings and advice are invaluable. Apart from these he is a good experimentalist, which helped me in understanding the practical ways to tackle the things. I learned a lot from him which would be helpful to me in my life.

I am very happy to have been associated with Prof. S.K. Malik of TIFR during the course of my work. I am thankful to him for his interest in my work and valuable information regarding the subject. Without his help I could not have gripped my subject. My special thanks to Prof. R. Nagarajan for teaching me the methodology and skill needed in the experimental work. His work on SmN₂B motivated me to study ferromagnetism. I would also be thankful to Prof. A.K. Nigam in helping me to finish my final experimental work for the book.

I would like to thank my lab-mates Nishaika, Rakesh, Pradip and Ravi for their cooperation and support during the period of my work. They have been there with all their advices and concerns at the times of fun as well as distress. I would also like to thank my other department friends who helped me when needed.

I would like to thank the non teaching staff of our department especially A.I. Kamble our lab assistant, Mr. Dilip and Mrs. Jose from departmental office, Mr. Ramchandra from Workshop, Mr. Rajan from departmental store, Mr. Pawar and Mr. Prabhu from electronics lab and Mr. Tiwari and Prasad from general physics lab.

Devang A. Joshi

Date: 12/12/2019

Place: Gandhinagar

FOR AUTHOR USE ONLY

**More
Books!**



yes
I want morebooks!

Buy your books fast and straightforward online - at one of world's fastest growing online book stores! Environmentally sound due to Print-on-Demand technologies.

Buy your books online at
www.morebooks.shop

Kaufen Sie Ihre Bücher schnell und unkompliziert online – auf einer der am schnellsten wachsenden Buchhandelsplattformen weltweit! Dank Print-On-Demand umwelt- und ressourcenschonend produziert.

Bücher schneller online kaufen
www.morebooks.shop

KS OmniScriptum Publishing
Brivibas gatve 197
LV-1039 Riga, Latvia
Telefax: +371 686 204 55

info@omniscryptum.com
www.omniscryptum.com

OMNIScriptum



FOR AUTHOR USE ONLY